

## INFORMATION TO USERS

This manuscript has been reproduced from the microfilm master. UMI films the text directly from the original or copy submitted. Thus, some thesis and dissertation copies are in typewriter face, while others may be from any type of computer printer.

**The quality of this reproduction is dependent upon the quality of the copy submitted.** Broken or indistinct print, colored or poor quality illustrations and photographs, print bleedthrough, substandard margins, and improper alignment can adversely affect reproduction.

In the unlikely event that the author did not send UMI a complete manuscript and there are missing pages, these will be noted. Also, if unauthorized copyright material had to be removed, a note will indicate the deletion.

Oversize materials (e.g., maps, drawings, charts) are reproduced by sectioning the original, beginning at the upper left-hand corner and continuing from left to right in equal sections with small overlaps. Each original is also photographed in one exposure and is included in reduced form at the back of the book.

Photographs included in the original manuscript have been reproduced xerographically in this copy. Higher quality 6" x 9" black and white photographic prints are available for any photographs or illustrations appearing in this copy for an additional charge. Contact UMI directly to order.

# UMI

A Bell & Howell Information Company  
300 North Zeeb Road, Ann Arbor MI 48106-1346 USA  
313/761-4700 800/521-0600



MUONIUM FORMATION AND DIFFUSION IN CRYOCRYSTALS

By

Gerald D. Morris

B. Sc. Simon Fraser University, 1986

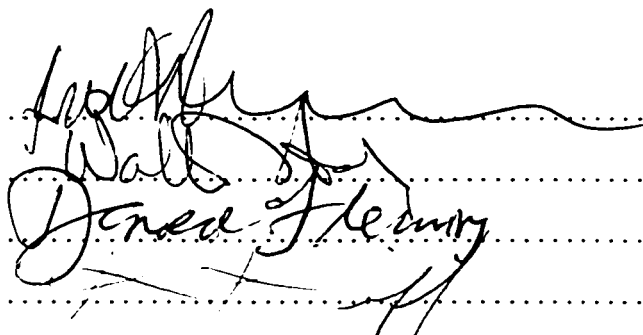
M. Sc. Univ. British Columbia, 1990

A THESIS SUBMITTED IN PARTIAL FULFILLMENT OF  
THE REQUIREMENTS FOR THE DEGREE OF  
DOCTOR OF PHILOSOPHY

in

THE FACULTY OF GRADUATE STUDIES  
DEPARTMENT OF PHYSICS AND ASTRONOMY

We accept this thesis as conforming  
to the required standard



Handwritten signature of Donald Henry, written over a series of horizontal dotted lines. The signature is in cursive and includes the name "Donald Henry".

THE UNIVERSITY OF BRITISH COLUMBIA

December 1997

© Gerald D. Morris, 1997



National Library  
of Canada

Acquisitions and  
Bibliographic Services

395 Wellington Street  
Ottawa ON K1A 0N4  
Canada

Bibliothèque nationale  
du Canada

Acquisitions et  
services bibliographiques

395, rue Wellington  
Ottawa ON K1A 0N4  
Canada

*Your file* *Votre référence*

*Our file* *Notre référence*

The author has granted a non-exclusive licence allowing the National Library of Canada to reproduce, loan, distribute or sell copies of this thesis in microform, paper or electronic formats.

The author retains ownership of the copyright in this thesis. Neither the thesis nor substantial extracts from it may be printed or otherwise reproduced without the author's permission.

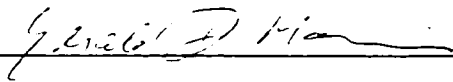
L'auteur a accordé une licence non exclusive permettant à la Bibliothèque nationale du Canada de reproduire, prêter, distribuer ou vendre des copies de cette thèse sous la forme de microfiche/film, de reproduction sur papier ou sur format électronique.

L'auteur conserve la propriété du droit d'auteur qui protège cette thèse. Ni la thèse ni des extraits substantiels de celle-ci ne doivent être imprimés ou autrement reproduits sans son autorisation.

0-612-27205-2

**Canada**

In presenting this thesis in partial fulfilment of the requirements for an advanced degree at the University of British Columbia, I agree that the Library shall make it freely available for reference and study. I further agree that permission for extensive copying of this thesis for scholarly purposes may be granted by the head of my department or by his or her representatives. It is understood that copying or publication of this thesis for financial gain shall not be allowed without my written permission.

  
\_\_\_\_\_

Department of Physics and Astronomy  
The University of British Columbia  
6224 Agricultural Road  
Vancouver, Canada  
V6T 1W5

Date:

  
\_\_\_\_\_

## Abstract

Energetic positive muons stopping in insulators often form the hydrogen-like neutral atom muonium by capturing an electron from the stopping medium. In this thesis it is shown that some of this muonium is formed by free electrons, produced along the muon's radiolysis track, diffusing to the muon, and subsequently forming muonium. Electron transport properties of the lattice play a role in delayed muonium formation in these solids. Application of an electric field along the initial muon momentum reveals a strong anisotropy of the spatial distribution of electrons in the vicinity of the muon, implying that the muon's direction of motion during thermalization is not completely lost by multiple scattering. Estimates of the initial electron-muon separation and muonium formation time are given.

Diffusion of muonium in cryocrystals has been studied with both transverse and longitudinal field muon spin relaxation techniques. Experimental results are compared to the theory of quantum tunnelling diffusion. In solid nitrogen at temperatures much smaller than the Debye temperature of the lattice, the data and theory are in good agreement, with a temperature dependence approaching the  $T^7$  law predicted by the theory of two-phonon quantum diffusion. At higher temperatures the agreement is qualitative only, but does show a key feature of two-phonon quantum tunnelling diffusion - a rapid *increase* in hop rate as temperature *decreases* due to the reduction of the phonon scattering rate.

Muonium in solid Xe is an extreme case of a light interstitial atom in a heavy lattice. This system was chosen to provide an example of tunnelling diffusion at relatively high temperatures where lattice dynamics could be expected to play a role in determining the muonium hop rate. The hop rate of muonium atoms in solid Xe was measured over a

range temperatures both above and below the Debye temperature and was found to vary by nearly four orders of magnitude. However, the absence of a temperature dependence in the activation energy leads to the conclusion that thermally-induced fluctuations of barrier height are not significant in this system.

## Table of Contents

Abstract	ii
Table of Contents	iv
List of Tables	vii
List of Figures	viii
Acknowledgement	xiii
<b>1 Introduction</b>	<b>1</b>
<b>2 Muon Spin Rotation Spectroscopy</b>	<b>5</b>
2.1 Muons and Muon Beams . . . . .	5
2.2 Hardware for $\mu SR$ Spectroscopy . . . . .	10
2.2.1 Time-Differential $\mu SR$ . . . . .	11
2.3 Data Reduction . . . . .	16
<b>3 Cryocrystals as <math>\mu SR</math> Samples</b>	<b>22</b>
3.1 Cryostats and Techniques . . . . .	22
3.2 Growing Cryocrystals . . . . .	24
3.3 Properties of Solid Nitrogen . . . . .	28
3.3.1 Crystal Structures . . . . .	28
3.3.2 Librational Modes in Solid Nitrogen . . . . .	29



<b>4</b>	<b>Muonium formation in Insulators</b>	<b>30</b>
4.1	Models of Muonium Formation . . . . .	31
4.2	Muonium Formation and Electron Transport in Insulators . . . . .	33
4.2.1	Muonium in Solid Nitrogen . . . . .	33
4.2.2	Muonium in Neon . . . . .	35
4.3	$\mu SR$ in Electric Fields . . . . .	36
4.3.1	Liquid Helium in an Electric Field . . . . .	37
4.3.2	Solid Nitrogen in an Electric Field . . . . .	38
4.4	Delayed Muonium Formation . . . . .	40
4.5	Implications of Delayed Muonium Formation for $\mu SR$ . . . . .	44
<b>5</b>	<b>Quantum Diffusion I: Theory</b>	<b>45</b>
5.1	An Introduction to Quantum Diffusion in Insulators . . . . .	45
5.2	Renormalization of the One-Phonon Interaction . . . . .	48
5.3	Linear Coupling; One-Phonon Diffusion . . . . .	50
5.4	Barrier Fluctuations . . . . .	52
5.5	Quadratic Coupling: Two-Phonon Limited Diffusion . . . . .	56
<b>6</b>	<b>Quantum Diffusion II: Experimental Results</b>	<b>60</b>
6.1	Two-Phonon Quantum Diffusion . . . . .	60
6.2	Muonium Diffusion in KCl . . . . .	63
6.3	Experimental Results in Solid Nitrogen . . . . .	65
6.4	Numerical Calculations: Solid Nitrogen . . . . .	71
6.5	One-Phonon Quantum Diffusion in Solid Xe . . . . .	82
6.6	Experimental Results in Solid Xe . . . . .	85
6.7	Numerical Evaluation of 1-Phonon Diffusion Theory . . . . .	88
6.8	Activated Tunnelling From Excited States . . . . .	90

<b>7</b>	<b>Conclusions</b>	<b>97</b>
7.1	Muonium Formation <i>via</i> Electron Transport . . . . .	97
7.2	Quantum Diffusion in Insulators . . . . .	99
	<b>Bibliography</b>	<b>102</b>
	<b>Appendices</b>	<b>106</b>
<b>A</b>	<b>Muonium Spin Polarization Function</b>	<b>106</b>
A.1	Transverse Field . . . . .	110
A.2	Longitudinal Field Polarization . . . . .	114
<b>B</b>	<b>Numerical Integration of a Highly Oscillatory Function</b>	<b>116</b>

## List of Tables

2.1	Physical properties of muons. [1]	6
A.2	Muon and electron $g$ -factors and magnetic moments.	106

## List of Figures

2.1	Muon decay asymmetry $a(\epsilon)$ , energy spectrum $\Lambda(\epsilon)$ and the product $a(\epsilon)\Lambda(\epsilon)$ plotted against the reduced positron energy $\epsilon$ . . . . .	10
2.2	A polar-coordinate plot of the rate of positron emission from muon decay as a function of angle from the muon spin $\Theta$ , at various energies $\epsilon$ . The distribution has axial symmetry about the muon spin polarization direction, which points toward the right in this plot. . . . .	11
2.3	A view of the M20 secondary channel and experimental area of the TRIUMF laboratory, configured with a conventional $\mu\mathcal{SR}$ spectrometer capable of transverse and longitudinal field measurements. (G.D.Morris) . . . . .	12
2.4	Schematic diagram showing an arrangement of a sample and five scintillation particle detectors. Each muon triggers the thin muon (TM) detector on entering the experiment. Later, the decay positron triggers one of the positron detectors. . . . .	13
2.5	Schematic logic diagram of the basic fast front-end electronics and signal timing for time-differential $\mu\mathcal{SR}$ experiments. Two decay positron detectors are shown; more may be added as required by the detector geometry.	15
2.6	(a) A histogram from the “Back” positron detector of a time-differential experiment on a sample of liquid Ne. (b) The asymmetry $a_B(t)$ extracted from the same histogram according to Eq. (2.8). The oscillations are due to the Larmor precession of the muons’ magnetic moments in an externally applied transverse magnetic field of 51.5 G. . . . .	20

2.7	The corrected asymmetry obtained from the Back-Front histogram pair using Eq. (2.13). Error bars shown and all parameter errors obtained in fitting are derived from counting statistics. . . . .	21
3.8	The interior parts of the coldfinger cryostat used for $\mu\mathcal{SR}$ experiments on solidified gases. The samples were condensed from the gas phase and frozen solid in the cell visible at the tip of the cold finger. Sample gas was allowed into the cell through the thin stainless tube, which was equipped with a heater to prevent blockages. (G.D. Morris) . . . . .	25
3.9	The sample cell used to condense gases to solids (approximately twice actual size), showing the attachment point to the cold finger and heater on the top of the cell. The flow of heat from top to bottom created a temperature difference of about 1 K down the cell walls. This is necessary to grow void-free crystals by ensuring that the sample freezes from the bottom up. The sample could be seen through the transparent mylar windows enclosing the front and back faces of the cell. (G.D. Morris) . . . . .	26
3.10	A sample of Ne being condensed and frozen; (a) The cell partially full of liquid Ne. (b) The cell full of Ne, some of which has solidified around the edges of the cell. (G.D. Morris) . . . . .	27
4.11	Muonium and slowly relaxing diamagnetic asymmetries measured in solid nitrogen. . . . .	34
4.12	Electron mobility in solid nitrogen measured by Loveland <i>et al.</i> [19] using a direct time-of-flight method. Various symbols indicate different samples. . . . .	35

4.13	Slowly relaxing diamagnetic asymmetry $A_S$ and muonium asymmetry $A_{Mu}$ (boxes and circles respectively) measured in a sample of solid nitrogen at $T=20$ K with an external electric field applied either along ( $E > 0$ ) or opposite ( $E < 0$ ) to the incoming muon beam direction. . . . .	39
4.14	Total muonium asymmetry measured in liquid nitrogen ( $T=75$ K) at long times where delayed muonium formation has ceased. The solid line represents a fit to theory, yielding a characteristic muonium formation time of $0.014(4)\mu s$ . . . . .	43
6.15	Phonon density of states $g(\omega)$ of KCl, from MacPherson and Timusk. Can. J. Phys. <b>48</b> , 2917 (1970) . . . . .	66
6.16	Dashed line: $\Omega_2(T)$ calculated in the case where $g(\omega)$ is the real phonon density of states of KCl. Solid line: the same calculation performed assuming a Debye model. . . . .	67
6.17	Temperature dependence of the exponent $\alpha = \frac{T}{\Omega_2} \frac{d\Omega_2}{dT}$ calculated for KCl with the real phonon spectrum (dashed line) and Debye-like phonon density of states (solid line). . . . .	68
6.18	Asymmetries measured in solid $N_2$ at various temperatures in weak longitudinal magnetic fields of (from bottom to top in each plot) 4, 8 and 12 G. . . . .	74
6.19	Muon spin polarization asymmetries measured in a transverse magnetic field of 5.2 G at temperatures of, from top to bottom, $T=3.45$ , 19 and 54 K in a sample of solid, pure $N_2$ . . . . .	75
6.20	Theoretical muonium spin relaxation functions in transverse field, showing the change from Gaussian to exponential form and reduction in the relaxation rate due to motional narrowing. For all curves $\delta = 1\mu s^{-1}$ . . . . .	76

6.21	Muonium spin polarization relaxation rates measured in solid nitrogen. Stars (12G), boxes (8G) and crosses (4G) indicate the LF data and all other points are in TF $\sim 5$ G for different samples. . . . .	77
6.22	Muonium hop rate $1/\tau_c$ in solid $N_2$ obtained from the spin relaxation rates $1/T_1$ and $1/T_2$ measured in LF and TF respectively. Stars indicate the results from LF data; all other points are from TF data. The power-law fit is shown by the solid line; the nearly parallel $T^7$ theoretical dependence is shown by the dashed line, offset for clarity. . . . .	78
6.23	Phonon density of states $g(\omega)$ of solid nitrogen at 22 K, data from Ref.[57].	79
6.24	$\Omega_2(T)$ for solid nitrogen, calculated from both the real (dashed line) and Debye model (solid line) phonon density of states $g(\omega)$ . . . . .	80
6.25	Muonium spin relaxation rates $1/T_2$ in slowly cooled, solid high-purity $N_2$ (circles), $N_2$ with 0.01% CO (boxes) and $N_2$ with 0.1% CO (triangles). . . . .	81
6.26	The phonon density of states of solid Xe used in the numerical evaluation of integrals over the phonon spectrum. . . . .	84
6.27	Muonium spin relaxation rates in solid Xe. Longitudinal relaxation rates $1/T_1$ measured in natural solid Xe in various magnetic fields (triangles:1451 G, circles:725 G, squares:363 G, stars: 72 G and crosses:21 G). The other points (diamonds) are $1/T_2$ measured in solid $^{136}\text{Xe}$ . . . . .	87
6.28	Muonium hop rate in solid Xe extracted from the LF data by simultaneous fits to data in different magnetic fields at each temperature. . . . .	88

6.29	An example of the integrand (top) and integral (bottom) of Eq. 6.20 calculated with the phonon spectrum of solid Xe and parameter values $\lambda_p/\lambda_B = 65$ . The difficulty in evaluating these multiple integrals arises from their oscillatory nature; the integral approaches a small constant value as $t \rightarrow \infty$ . The parameters in this relatively forgiving example were chosen to make the limiting value of the integral visible by eye. . . . .	94
6.30	The Mu hop rate in solid Xe presented in an Arrhenius plot, with the solid line showing the fit to theory calculated by numerical integration. A simple classical model also falls on this line, as does the Flynn-Stoneham model, since all these models are of the same exponential form. . . . .	95
6.31	Potential energy of the Mu atom as a function of displacement from the centre of the octahedral site, along the [111] direction. The configuration of Xe atoms was computed by minimizing the potential of each atom in a $5 \times 5 \times 5$ unit cell cluster, with the interstitial Mu at the centre. . . . .	96
A.32	Breit-Rabi energy level diagram of the four states of muonium in a magnetic field. . . . .	111



## Acknowledgement

This thesis is a result of the work of the many people at the TRIUMF laboratory who contributed in innumerable ways to providing the muons and constructing our experiments.

Thanks go to all the people who worked some very long days and nights to collect the data: Tanya Riseman, Kim Chow, Tim Duty, Masa Senba and Sarah Dunsiger, and the TRIUMF  $\mu\mathcal{SR}$  facility staff Mel Good, Curtis Ballard, Bassam Hitti, Don Arseneau and Syd Kreitzman for their support in both setting up and running these experiments.

I am very grateful to Slava Storchak, whose ideas and hard work took our experiments far, Dr. Nikolai V. Prokof'ev, for discussions and notes from which I learned quantum diffusion, and my committee members Drs. Walter Hardy, Rob Kiefl and Philip Stamp for their suggestions and encouragement. I would especially like to thank my thesis advisor Jess Brewer, whose idea it was to study cryocrystals, for guiding these experiments from their beginning, and for his suggestions, corrections and help in bringing this thesis to completion.

## Chapter 1

### Introduction

This thesis is about two rather diverse topics within the field of muon spin rotation/relaxation/resonance ( $\mu\mathcal{SR}$ ) spectroscopy: muonium formation in insulators and quantum diffusion of muonium in simple insulating solids. They are linked by the nature of the samples studied – they are van der Waals solids made of atoms or small molecules so weakly interacting they are gases at room temperature, solidifying only at very low temperatures and therefore called *cryocrystals*.

When energetic positive muons are injected into most insulating materials a fraction of the muons capture an electron from the sample and form a neutral, light hydrogen-like atom, with the muon as its nucleus (chemical symbol Mu.) The chemistry of positive muons is essentially the same as that of protons; those muons that don't form muonium atoms become bound into molecular ions instead. It has long been known that the fraction of each of these chemical species - muonium and the diamagnetic fraction, referring to the total electron spin density at the muon which is zero for a muon in a molecular bond - vary among different insulating materials. [12] This is a relatively old problem in the field of  $\mu\mathcal{SR}$  and of interest to radiation chemists, but is not widely appreciated by many researchers applying  $\mu\mathcal{SR}$  to a growing number of areas in condensed matter physics such as magnetism and superconductivity.

The first part of this thesis is about the use of electric fields in  $\mu\mathcal{SR}$  experiments to extract new information about end-of-track processes leading to muonium formation. In some of these cryocrystals it is possible to influence the muonium and diamagnetic

fractions with an external electric field applied either parallel to or anti-parallel to the incoming muons' direction of motion. This is the first observation of an electric field having an effect on muonium formation in a solid. The presence of an effect, and its dependence on orientation of the external electric field, imply that, at least sometimes, the electrons that eventually become bound to muons originate far from the muons. Thus, it seems that electron transport properties of the solid play a role in muonium formation. An overview of this technique and the interpretation of results is given in Chapter 4.

The main topic of this thesis is the use of the muonium that is formed in cryocrystals for the study of quantum diffusion under one- and two-phonon coupling to the vibrational modes of the lattice. Tunnelling diffusion of light interstitials is of great interest because it is inherently quantum mechanical in nature. It provides us with a system in which to study a quantum process subject to a dissipative coupling to a bath of excitations. Muons and muonium are particularly good probes of quantum diffusion since the muon has a mass about 1/9 that of hydrogen; its tunnelling amplitude is larger than that of any ordinary atom in the same potential.

Previously, studies of muon diffusion in Cu and Al identified a cross-over from high-temperature, stochastic thermally-activated hopping to a low-temperature regime where the coherent propagation of the muon was disrupted by scattering of electrons and phonons. Minima in the muon hop rates occurred at about 50 K and 5 K in these metals respectively. [42, 47] In metals the interaction of the muon with conduction electrons serves to reduce the tunnelling amplitude and suppress the temperature dependence. [50, 51]

More recently, diffusion rates of muonium in ionic solids KCl and NaCl have been measured. [66, 43] Neutral muonium in insulating materials avoids the interaction with

conduction electrons, so in these systems the dominant interaction between the interstitial particle and its environment is with excitations of the lattice. In NaCl and KCl the muonium hop rate also showed minima at about 50 K and 70 K respectively. In the low temperature regime the scattering of phonons (or electrons) serves to diminish the tunnelling bandwidth, so the key characteristic is a hop rate that increases as the temperature drops.

Chapter 5 reviews the theory of phonon-mediated quantum diffusion (due mostly to Kagan and Prokof'ev), with the emphasis on explaining the origin of the temperature dependences one can measure and the influence of the phonon spectrum.

This thesis presents results from experiments in which diffusion rates of muonium in van der Waals solids were measured. Measurements in both low and high temperature regimes are discussed and results are compared with the current theory of quantum diffusion in chapter 6.

The current theory of phonon-mediated quantum diffusion is successful in predicting the observed temperature dependence of the muonium diffusion rate in solid nitrogen at temperatures well below the Debye temperature. The measured temperature dependence of the diffusion rate was found, for the first time, to be very nearly as strong as predicted by theory. Moreover, these results demonstrate qualitatively the influence of static energy level shifts, which inevitably become important at sufficiently low temperatures. Kadono *et al.* also studied the influence of deliberately induced defects in a sample of KCl doped with varying amounts of Na substitutional impurities. [45] In this inhomogeneous system the lattice has both situations present simultaneously. The muonium ensemble was divided into two parts - one trapped by the static shifts and the other, far from impurities, diffusing as in pure KCl.

At temperatures where the phonon scattering rate is sufficient to destroy the coherent channel, tunnelling diffusion proceeds by stochastic, phonon-assisted hopping. Tunnelling

at temperatures approaching the Debye temperature should be sensitive to the presence of short-wavelength phonons since these excitations will cause the shape and height of the barrier to tunnelling to fluctuate. Optimal configurations of atoms that define the barrier are therefore expected to enhance the average tunnelling rate. Experiments on muonium diffusion in solid Xe were carried out in an attempt to detect this effect. The results do not show any on-set of this effect as the temperature rises. However, it is possible that the diffusion mechanism in this system is dominated by a classical activation to an excited state, obscuring the temperature dependence of the tunnelling rate.

## Chapter 2

### Muon Spin Rotation Spectroscopy

In the most general description Muon Spin Rotation/Relaxation/Resonance (collectively called  $\mu\mathcal{SR}$ ) includes all experimental techniques that exploit the anisotropic decay of spin-polarized muons for studying materials. This covers an enormous range of fields of study, presently including various aspects of chemistry, magnetism, superconductivity, semiconductor properties and quantum diffusion. The essential ingredient common to all these experiments is that the muons interact with the material in which they have been deposited in various ways that have observable effects on their spin polarization, ultimately allowing one to extract information about the muon's environment. In order to understand how this is done we discuss the basics of muons, muon beams and details of  $\mu\mathcal{SR}$  experiments in this chapter.

#### 2.1 Muons and Muon Beams

Muons are elementary particles, second-generation charged leptons about 207 times more massive than electrons. Two properties of muons are key to the  $\mu\mathcal{SR}$  technique: (a) they have an intrinsic spin angular momentum (of  $\hbar/2$ ) and a magnetic moment (several times larger than the proton magnetic moment) which provides a means for the environment to couple with the spin, and (b) they are almost always created or destroyed in weak interactions which maximally violate parity symmetry. Thus the positive muons from  $\pi^+$  decay are 100% spin-polarized and each decays anisotropically via the weak interaction to an energetic positron whose momentum is correlated with the muons angular

Mass, $m_\mu$	105.658389(34) MeV/ $c^2$
Lifetime, $\tau_\mu$	2.19714(7) $\mu\text{s}$
Charge, $q$	$\pm e$
Intrinsic spin	$\hbar/2$
Magnetic moment, $\mu_\mu$	$4.4904514(15) \times 10^{-26}$ J/T
	$8.890577(21) \mu\text{N}$
Spin $g$ -factor, $g_\mu$	2.002331846(17)
Gyromagnetic ratio, $\gamma_\mu = g_\mu \mu_\mu / \hbar$	135.69682(5) MHz/T

Table 2.1: Physical properties of muons. [1]

momentum at the instant of decay. The physical properties of muons that are important to  $\mu\text{SR}$  are listed in Table 2.1.

Muon spin rotation requires an intense beam of spin polarized muons obtained from the decay of charged pions ( $\pi^\pm$ ). The pions are first produced by the collisions of energetic protons with the nuclei of a target, typically made of carbon or beryllium, in the proton beam of a particle accelerator. Charged pions with mass  $m_{\pi^\pm} = 139.5669$  MeV/ $c^2$  then decay to produce one muon neutrino and one muon;

$$\pi^+ \rightarrow \mu^+ + \nu_\mu \quad (2.1)$$

$$\pi^- \rightarrow \mu^- + \bar{\nu}_\mu \quad (2.2)$$

with a lifetime of 26.03 ns. Conservation of energy and momentum dictate the outcome of the two-body final state: muons and neutrinos always have momentum 29.7885 MeV/ $c$ ; the muon always carries away the same kinetic energy of 4.119 MeV in the pion's rest frame. As a result of parity violation in the weak decay of the spinless pion, muon neutrinos are always left-handed (their spin angular momenta pointing in the opposite direction to their linear momenta), so that positive muons (anti-muons, to be precise) produced in this way must also *always* have their spin angular momenta pointed exactly backward along their momenta. Anti-neutrinos have their spins and momenta parallel.

so negatively charged muons similarly produced have spins parallel to their momenta.

It was standard practice early in the development of  $\mu SR$  to collect positive and negative muons from pions that decayed while in flight down the secondary beamline. In order to stop the maximum number of muons in the thinnest samples it was preferable to select those muons with the lowest energy, so “backward decay” muons with momenta (in the pions’ frame) opposite to the pions’ momenta (in the lab frame) were usually chosen for experiments; however these are not entirely spin polarized and still have a relatively high momentum of  $\sim 40\text{-}120\text{ MeV}/c$ .

So far this discussion has been equally applicable to positive and negative particles. but this ends when either pions or muons are stopped in matter due to the different chemical nature of negatively and positively charged particles in matter. Negative pions that stop in the target behave like heavy electrons and rapidly cascade down to tightly bound orbitals where they almost always undergo capture by the nucleus instead of decaying to negative muons. Positive pions that have come to rest in solids take up interstitial positions between atoms so they are too far from nuclei to be captured: as far as  $\mu SR$  is concerned their lifetime is unaffected by any properties of the target material.

Perhaps the most important development in muon beam technology was the realization that by removing the windows that isolated the primary and secondary particle beamlines, and turning down the momentum tuning of the secondary channel. the low momentum positively charged so-called *surface* muons could be brought out to an experiment. [2, 3] Those positive pions that happen to come to rest just within the surface of the pion production target decay to muons that need penetrate only a short distance (a fraction of a millimeter at most) to escape from the target into the beamline vacuum, with momenta up to the maximum of  $p_{\mu}^{\max}=29.8\text{ MeV}/c$ .

These muons have a range of about  $140\text{ mg}/\text{cm}^2$  in water so they conveniently penetrate several thin windows but still stop in small samples, while the spins of the muons



remain almost completely polarized. Surface muon beams are not mono-energetic since muons will come from pions decaying at various depths into the pion production target: those that start out deeper will spend more of their range and lose more energy on their way out. The resulting muon spectrum rises with momentum, then drops sharply at the “surface muon edge” at  $p_\mu^{\max}$ . Secondary beamlines, usually with magnetic steering elements and positron separators ( $\vec{E} \times \vec{B}$  velocity selectors which remove positron contamination from the muon beam) are tuned to transport muons in a narrow momentum range  $\Delta p_\mu/p_\mu$  of a few percent, with  $p_\mu$  usually chosen to be just below the surface muon edge, in order to achieve the greatest beam intensity. Efforts to make still lower-energy polarized muon beams continue to this day, the motivation being the desire to deposit muons into extremely thin samples or with controlled depths into the surface layers of a sample. Compared to backward decay muons, surface muons are easier to collimate and focus into a clean, well-defined spot on a thin sample, minimizing the background due to muons that miss the sample. Most important, they arrive at the sample virtually 100% spin polarized.

The positive muon decays via the parity-violating weak interaction to produce an energetic positron and two neutrinos:



with a lifetime of  $\tau_\mu = 2.19714(7) \mu\text{s}$  that is unaffected by sample properties or experimental conditions. In this decay the three body final state allows for a spectrum of positron energies from 0 to  $E_{e^+}^{\max} = 52.3 \text{ MeV}$ , since all combinations of neutrino and positron momenta that conserve energy and momentum are allowed. The decay rate also depends on the inner product  $\vec{\sigma} \cdot \vec{p}$  of the positron spin  $\vec{\sigma}$  and momentum  $\vec{p}$  in such a way that the positron is emitted preferentially in the direction of the muon spin at the instant of decay. The probability per unit time of being emitted in a direction at an angle  $\Theta$  to the

spin is given by

$$\frac{d^2 W(\Theta)}{d\epsilon d(\cos \Theta)} = \frac{G^2 m_\mu^5}{192\pi^3} \Lambda(\epsilon) [1 + a(\epsilon) \cos(\Theta)] \quad (2.4)$$

where the asymmetry of the decay  $a(\epsilon)$  is a function of the reduced positron energy  $\epsilon = E_{e^+} / E_{e^+}^{\max}$  and is given by

$$a(\epsilon) = \frac{2\epsilon - 1}{3 - 2\epsilon}, \quad (2.5)$$

while the normalized spectrum of positron energies resulting from the available phase space is

$$\Lambda(\epsilon) = 2(3 - 2\epsilon)\epsilon^2. \quad (2.6)$$

These functions of positron energy are shown in Fig. 2.1, along with their product. The resulting angular distribution of decay positrons is shown in Fig. 2.2 for several values of positron energy. Since both the number of positrons and their decay asymmetry rise with energy, the asymmetry of the ensemble angular distribution is largely due to those positrons with energies above about 2/3 of the maximum energy.

We cannot be certain in which direction a single muon spin was pointing from its single decay positron. However, we can determine the ensemble average polarization by measuring the angular distribution of positrons emitted in the decay of a large number of muons. Fast scintillators and phototubes give nanosecond timing resolution but do not yield any information about the positrons' energies. If positrons of all energies are detected with equal efficiency, we must integrate over the positron energy spectrum to obtain a theoretical ensemble average asymmetry  $\langle a \rangle_\epsilon = 1/3$ . In practice, this theoretical asymmetry is never achieved due to the use of positron detectors that cover quite a large solid angle, averaging over a range of  $\theta$  in Eq. (2.4) which reduces the observed asymmetry considerably. With a few cm of absorber one can eliminate the low energy positrons, which have  $a(\epsilon) < 0$  and actually *deduct* from the ensemble asymmetry, to increase the measured asymmetry and improve the signal-to-noise ratio. If the positrons

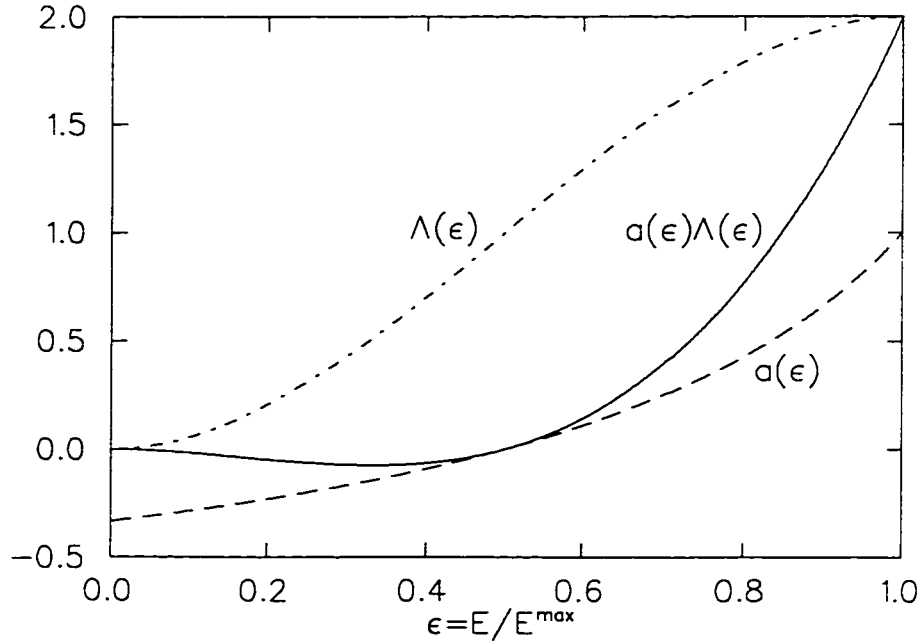


Figure 2.1: Muon decay asymmetry  $a(\epsilon)$ , energy spectrum  $\Lambda(\epsilon)$  and the product  $a(\epsilon)\Lambda(\epsilon)$  plotted against the reduced positron energy  $\epsilon$ .

with energy  $\epsilon \leq 0.5$  are absorbed, for example, the asymmetry of the remaining ensemble rises to 0.435. There is usually some material such as cryostat parts and sample mounts between the sample and positron detectors that will stop some of the low energy positrons. Overall, the maximum initial asymmetry measured by most spectrometers is typically about 0.25.

## 2.2 Hardware for $\mu SR$ Spectroscopy

An experimental area used for  $\mu SR$  is shown in Fig. 2.3, this one being the M20 channel at the TRIUMF laboratory. The  $\mu SR$  experimental apparatus is positioned at the end of the secondary beamline, downstream from the final focusing quadrupole magnets.

The spectrometer consists of a set of Helmholtz magnet coils to produce an externally applied magnetic field, a cryostat (or for some experiments an oven) for controlling sample temperature, and a set of fast scintillation detectors that signal the passage of incoming

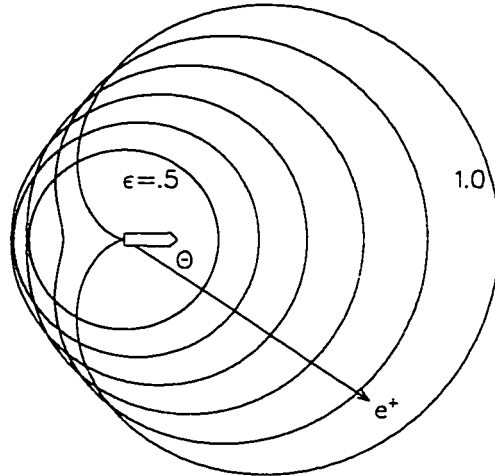


Figure 2.2: A polar-coordinate plot of the rate of positron emission from muon decay as a function of angle from the muon spin  $\Theta$ , at various energies  $\epsilon$ . The distribution has axial symmetry about the muon spin polarization direction, which points toward the right in this plot.

muons and outgoing positrons. Most beamlines used for  $\mu\mathcal{SR}$  incorporate spin rotators into the positron separators that allow one to precess the muons spins in flight by  $\pi/2$  with respect to their momenta before they arrive at the experiment. This spin-rotated mode allows the experimenter more flexibility in orienting the initial spin polarization with respect to the applied field. This is especially useful when the experiment to be performed requires a strong magnetic field transverse to the muon spin, which would otherwise steer the beam off the sample.

### 2.2.1 Time-Differential $\mu\mathcal{SR}$

By far the most common form of  $\mu\mathcal{SR}$  experiment operates in the *time differential* mode. An arrangement of detectors surrounding a sample is shown schematically in Fig. 2.4. The positron detectors are usually mounted in pairs on opposite sides of the sample; Back-Front, Left-Right and Up-Down, a geometry well suited to extracting the signal, which we will come to shortly. Clever variations on this scheme have been used for



Figure 2.3: A view of the M20 secondary channel and experimental area of the TRIUMF laboratory, configured with a conventional  $\mu\mathcal{SR}$  spectrometer capable of transverse and longitudinal field measurements. (G.D.Morris)

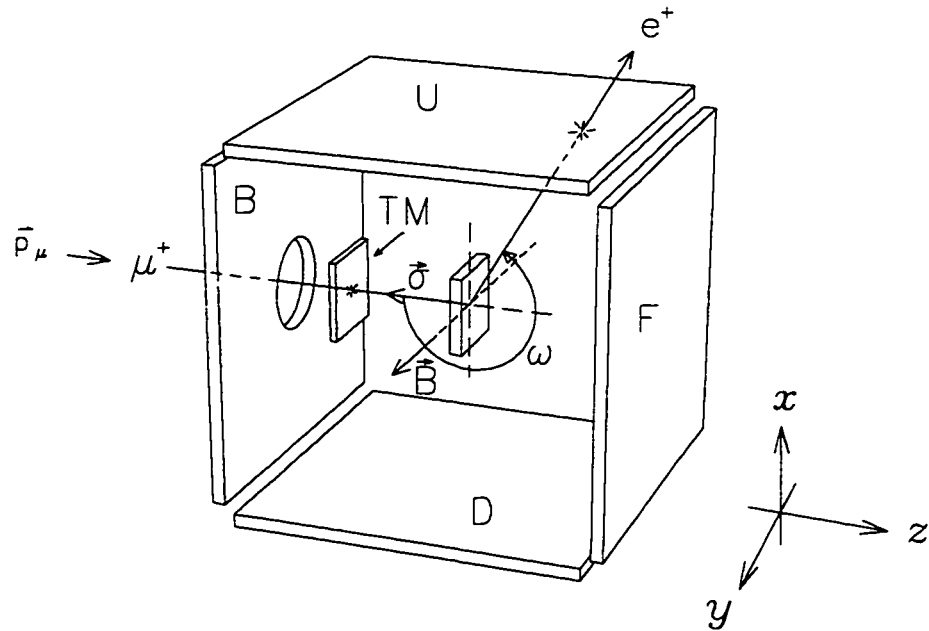


Figure 2.4: Schematic diagram showing an arrangement of a sample and five scintillation particle detectors. Each muon triggers the thin muon (TM) detector on entering the experiment. Later, the decay positron triggers one of the positron detectors.

special applications, to accommodate very small samples or very high magnetic fields for example, but all of these perform essentially the same function of detecting the angular distribution of positrons. We include in our example a magnetic field along the  $\hat{y}$ -axis, transverse to the initial muon polarization so that the spins undergo Larmor precession in the  $\hat{x} - \hat{z}$  plane until the muons decay. Such experiments are termed transverse-field (TF) experiments, giving a signal that demonstrates in an intuitive way the analogy between  $\mu\mathcal{SR}$  and traditional NMR. One can also perform experiments with no (zero) external magnetic field (ZF) or with a longitudinal field (LF) parallel to the initial muon spin, with no other change to the experimental apparatus.

Each muon enters the experiment with a velocity of about  $1/4$  of the speed of light,

passing through a thin (0.125 mm) plastic muon scintillation detector (TM) which provides a “start” pulse to the data acquisition electronics. The muon then enters the sample a few cm further downstream, where it comes to a stop and eventually decays. When one of the positron detectors intercepts the outgoing positron, a “stop” pulse is generated and the elapsed time is determined by a time-to-digital converter (TDC) - essentially a stopwatch able to measure time intervals with a resolution of about 1 ns. The histogram for that positron detector is then incremented in the bin corresponding to the measured time interval. In most experiments the histogram time range extends up to 5 or 6 muon lifetimes.

The high speed front-end logic of the data acquisition system, implemented in standard NIM electronics, is shown schematically in Fig. 2.5. The rest of the data acquisition electronics consists of a histogramming memory, various support systems such as event scalars and detector selection registers and a computer which controls the experiment and reads out the data.

In order to measure the elapsed time we must know from which muon a given decay positron originated. The easiest way to do this is to veto any event for which a positron cannot be unambiguously paired with a muon. Each muon is given a fixed time interval (“pile-up” gate) to decay, during which the arrival of *another* muon would veto the entire sequence and both muons would be discarded. At meson facilities that produce pions continuously (as opposed to those with pulsed primary proton beams), the muons arrive at random time intervals. This and the dead-time of the TDC place a practical limit on the mean rate at which one can take muons to about 50,000/s. Events in which two or more positrons are detected within the data gate are also rejected by the TDC. Delays are introduced into the positron “stop” signals so that the early part of each histogram contains counts from uncorrelated start and stop signals. This allows the background rates to be estimated from the part of each histogram *before*  $t = 0$ , the moment when

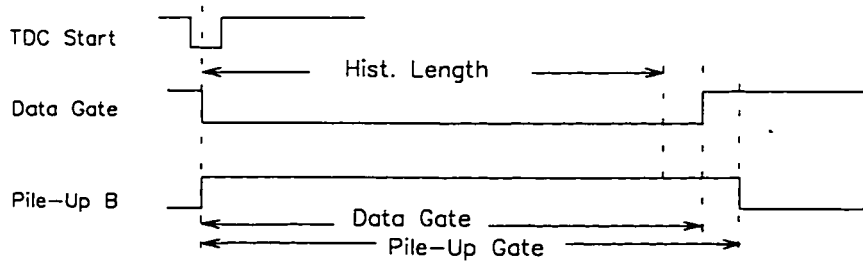
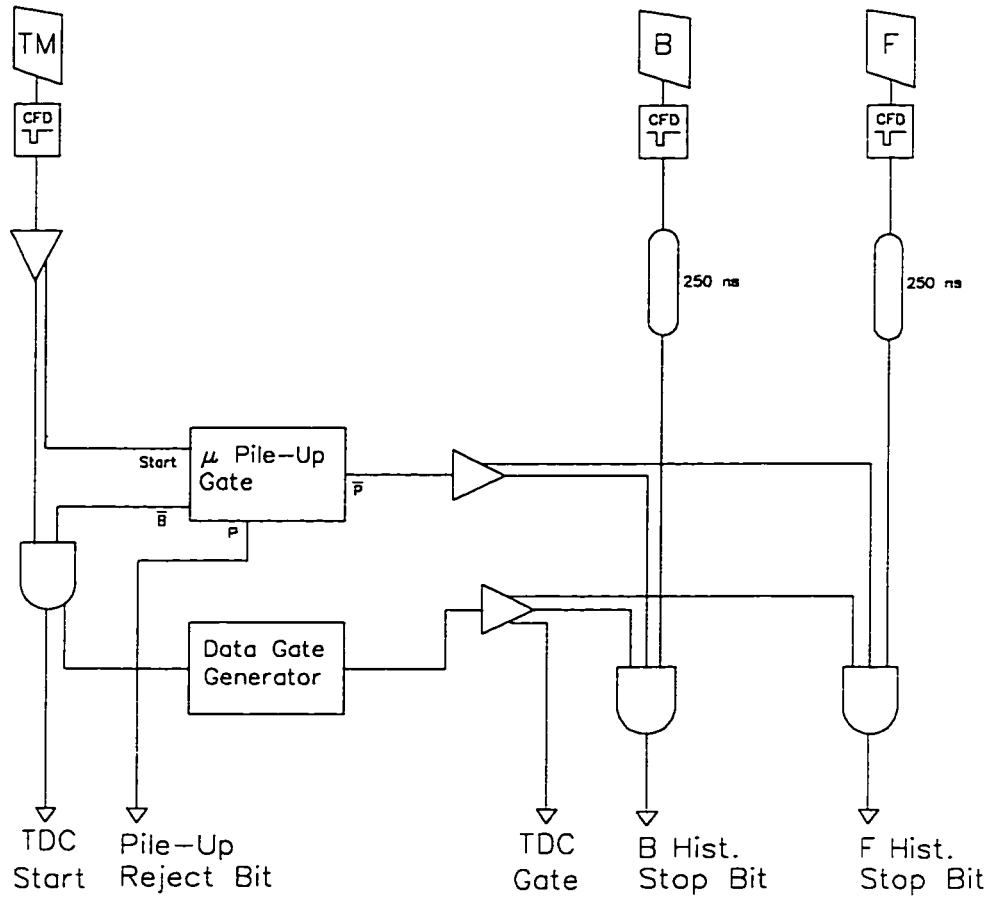


Figure 2.5: Schematic logic diagram of the basic fast front-end electronics and signal timing for time-differential  $\mu SR$  experiments. Two decay positron detectors are shown: more may be added as required by the detector geometry.



start and stop signals happen simultaneously.

Histograms are accumulated for each positron detector  $i=(\text{B.F.L.R.U.D})$ , each having the form

$$N_i(t) = N_0 \left\{ b_i + e^{-t/\tau_\mu} [1 + a_i(t)] \right\}, \quad (2.7)$$

where  $N_0$  is the normalization,  $a_i(t)$  is the experimental asymmetry and  $b_i$  is a time-independent background. The single-histogram asymmetry is easily obtained from the histogram by rearranging this;

$$a_i(t) = \left[ \frac{N_i(t)}{N_0} - b_i \right] e^{t/\tau_\mu} - 1, \quad (2.8)$$

which can be fitted numerically to a model function to obtain estimates of  $N_0$  and  $b_i$ . An example of raw histogram data from the Back counter is shown in Fig. 2.6a. In this experiment a transverse magnetic field of 51.5 G caused the muons' spins to precess at a frequency  $\omega_\mu = \gamma_\mu B = 2\pi \times 0.699$  MHz, which is apparent in the sinusoidal oscillations in the asymmetry. Figure 2.6b is the asymmetry  $a_B(t)$  extracted from the raw data using Eq. (2.8); the solid line is a theoretical asymmetry representing the sum of two signals with different (exponential) relaxation rates.

### 2.3 Data Reduction

We are interested in extracting the asymmetry, the signal manifesting the influence of the muon's environment on its spin. Ultimately we will want to fit the experimental asymmetry to a model function in order to measure some physical property, but ideally the experimental asymmetry should be obtained independently of the model function. One way of extracting the signal from the raw data is to make use of the symmetry of the detectors on opposite sides of the sample. With this geometry the two detectors view the same positron angular distribution, but from diametrically opposed directions, so that

the counts in the two histograms are (for the Back-Front pair)

$$N_{\text{B,F}}(t) = N_0 \{b_{\text{B,F}} + [1 \pm a_{\text{B,F}}(t)]e^{-t/\tau_\mu}\}. \quad (2.9)$$

We can then calculate the asymmetry  $a_z$  for the (B,F) pair

$$a_z(t) = \frac{[N_{\text{B}}(t) - N_0 b_{\text{B}}] - [N_{\text{F}}(t) - N_0 b_{\text{F}}]}{[N_{\text{B}}(t) - N_0 b_{\text{B}}] + [N_{\text{F}}(t) - N_0 b_{\text{F}}]}, \quad (2.10)$$

naively assuming a common asymmetry  $a_z(t) = a_{\text{B,F}}(t)$ . Ideally, the efficiency (probability of a particle being detected) of all positron detectors would be the same, as would be the solid angle they subtend. In general neither of these actually holds, so corrections are needed to avoid distorting the signal. It is easy to see, for example, that if the sample were closer to the B positron detector than to F, then B would intercept (all other things being equal) more positrons by virtue of its larger solid angle, and because it averages over a greater range in  $\Theta$ , the amplitude of the precession signal in our TF experiment would be lower. Photomultiplier tube characteristics, operating voltages and discriminator settings will have a direct bearing on the efficiency of each detector. It would be a difficult task to match a pair of detectors so they had identical characteristics: fortunately, it is not necessary to do so. If we allow for differing efficiencies  $\eta_i$  and asymmetries  $A_i P_z(t)$ , where  $P_z(t)$  is the spin polarization along the  $z$ -axis, which is common to the Back and Front detectors, then each histogram is described by

$$N_{\text{B,F}}(t) = N_0 \{b_{\text{B,F}} + \eta_{\text{B,F}}[1 \pm A_{\text{B,F}}P_z(t)]e^{-t/\tau_\mu}\} \quad (2.11)$$

and the experimental asymmetry is now

$$\begin{aligned} a_z(t) &= \frac{\eta_{\text{B}}[1 + A_{\text{B}}P_z(t)] - \eta_{\text{F}}[1 - A_{\text{F}}P_z(t)]}{\eta_{\text{B}}[1 + A_{\text{B}}P_z(t)] + \eta_{\text{F}}[1 - A_{\text{F}}P_z(t)]} \\ &= \frac{1 - \alpha + (1 + \alpha\beta)A_{\text{B}}P_z(t)}{1 + \alpha + (1 - \alpha\beta)A_{\text{B}}P_z(t)} \end{aligned} \quad (2.12)$$

in which  $\alpha = \eta_F/\eta_B$  and  $\beta = A_F/A_B$ . Rearranging this we obtain a function of the experimental asymmetry  $a(t)$  corrected for differences between detectors.

$$A_B P_z(t) = \frac{1 - \alpha - (1 + \alpha\beta)a_z(t)}{(1 - \alpha\beta)a_z(t) - (1 + \alpha\beta)}. \quad (2.13)$$

This introduces two free parameters  $\alpha$  and  $\beta$  that can be obtained by fitting a model spin polarization function to the experimental asymmetry. The same procedure can be carried out for the other pair of detectors on the  $x$  or  $y$  axes. (Usually there is no need to use detectors on more than two axes since there can never be any asymmetry along an axis that is always perpendicular to the muon spin.)

Returning to our example TF experiment, Fig. 2.7 shows the corrected asymmetry extracted from the (B,F) pair of detectors. The evolution of the muon spin polarization is essentially the same as the familiar free induction decay signal of nuclear magnetic resonance. The most obvious characteristic is the Larmor precession frequency, giving the mean magnetic field at the muon site. We will need to draw on everything we know about the sample from other sources in order to interpret the polarization relaxation function. For example, if we know the sample contains atoms possessing magnetic moments then we expect the muon will be subject to internal fields which may fluctuate in time or in space (or both). In this case, muons will experience different local fields and so precess at different frequencies, which would be reflected in the loss of coherence of the precessing muon ensemble. In other cases, the disappearance of polarization may be entirely due to one or more chemical reactions. The loss of polarization then simply reflects the *amount* of the muon ensemble that has undergone a chemical reaction. This must be the case for the signal seen in our Ne sample, where there are no nuclear magnetic moments present. The amplitude of the muon signal decreases with time because the muons pick up stray electrons and so form neutral muonium atoms (a topic that will occupy much of our attention in chapters to follow) which behave entirely differently

- the “diamagnetic” muon signal gradually vanishes with time. In either case we need to have some idea qualitatively what may be happening to the muon before we can extract quantitative information by fitting a model polarization function. Measuring the polarization function is the easy part; deducing the correct model is usually challenging, but yields all the physics.

We have discussed here only the most common sorts of  $\mu SR$  experiments. Other techniques, falling under the general label of Time-Integral  $\mu SR$ , are described elsewhere [5, 6] including level-crossing resonance experiments and RF- $\mu SR$ .

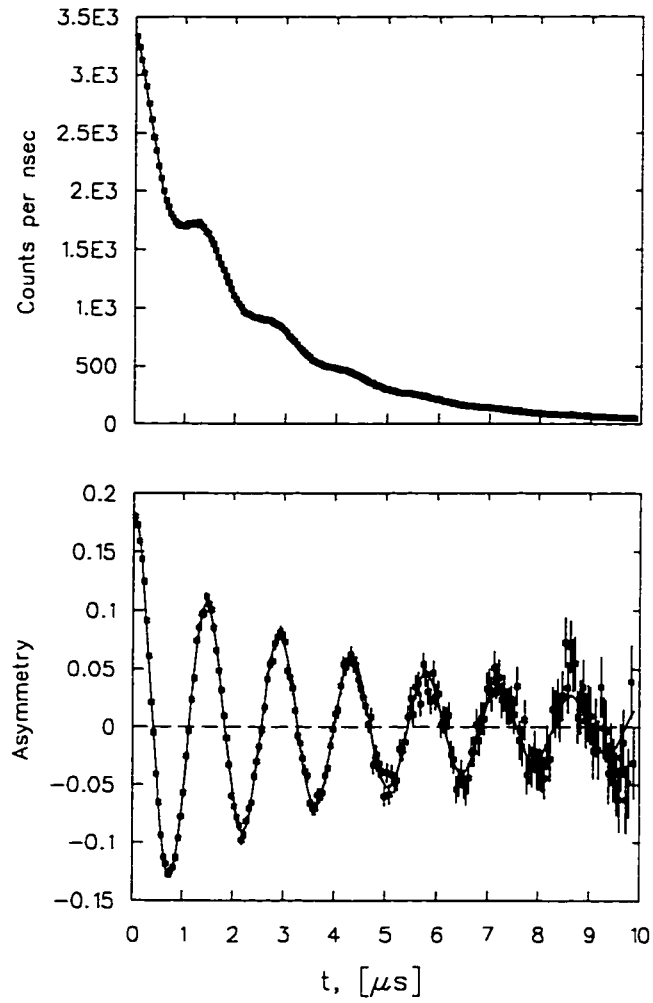


Figure 2.6: (a) A histogram from the “Back” positron detector of a time-differential experiment on a sample of liquid Ne. (b) The asymmetry  $a_B(t)$  extracted from the same histogram according to Eq. (2.8). The oscillations are due to the Larmor precession of the muons’ magnetic moments in an externally applied transverse magnetic field of 51.5 G.

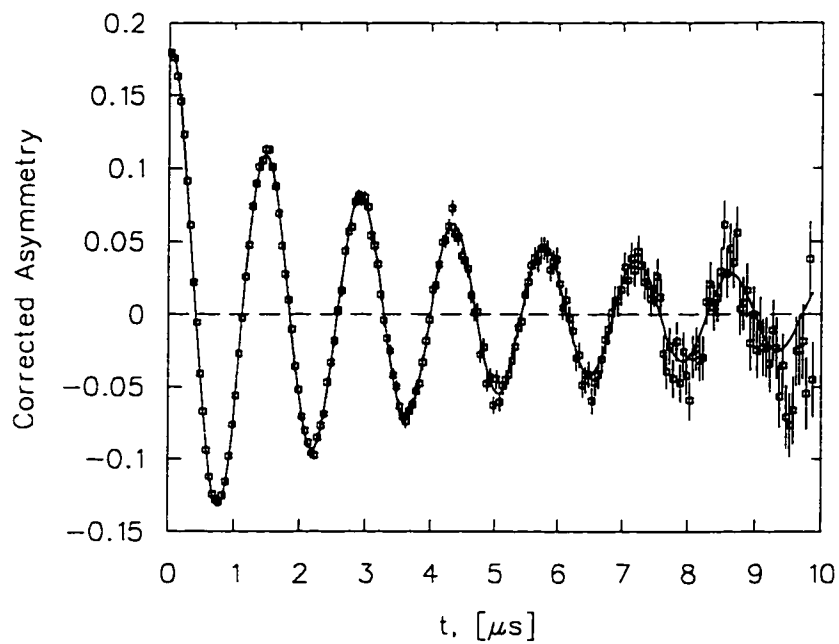


Figure 2.7: The corrected asymmetry obtained from the Back-Front histogram pair using Eq. (2.13). Error bars shown and all parameter errors obtained in fitting are derived from counting statistics.

## Chapter 3

### Cryocrystals as $\mu SR$ Samples

#### 3.1 Cryostats and Techniques

The sample environment suitable for typical muon spin relaxation experiments must allow a beam of muons into the sample, allow the decay positrons to escape and allow one to control the experimental variables, usually temperature and applied magnetic field at the sample. Meeting these requirements imposes several conditions on the experimental apparatus; most important of these (in the sense that it is the easiest requirement to violate unintentionally) is that the total mass of material in the path of the low momentum surface muon beam must be small enough that the muons reach the sample without appreciable attenuation or scattering. The range of these low energy (4.2 MeV) muons is about 140 mg/cm<sup>2</sup> of low-Z material. This places a practical upper limit of about 70 mg/cm<sup>2</sup> on the total mass of material present in beamline windows, air gaps, muon detectors, cryostat windows, coolants and heat shields if we are to avoid stopping a significant number of muons before they reach the bulk of the sample. Normally, this is not a difficult technical problem for the majority of samples that are room-temperature solids. In the case of Van der Waals solids that condensed from room-temperature gases, this is made much more difficult by the need for the sample to be held within a miniature pressure vessel, which is in turn surrounded by vacuum in order to provide thermal isolation. Crystals of these solids are grown from the liquid, under a pressure slightly greater than their equilibrium vapour pressure at the melting point, typically 100 – 700 mbar

depending on the material. Even in the solid phase, the equilibrium vapour pressure can be a considerable fraction of an atmosphere. Therefore, the cryostat must simultaneously provide the contradictory conditions of thin beam windows and considerable mechanical strength. To make matters more difficult it must also be able to withstand changing pressure at cryogenic temperatures due to thermal cycling. In addition to this, the cryostat must provide a way for the sample gas to be piped into the sample space from room temperature outside the cryostat.

The cryostat used for the majority of the results presented here was a commercial Janis Supertran continuous-flow coldfinger cryostat with modifications enabling the condensation of room-temperature gases to liquids that were subsequently frozen to solid samples of a size suitable for  $\mu\text{SR}$ . Samples filled the volume of a cell measuring 22 x 22 x 6 mm machined from a solid block of copper, with the open square faces covered with 0.012 cm thick transparent Mylar windows. (Figures 3.8 and 3.9 show the coldfinger cryostat and the sample cell in detail.) These windows were epoxied to the copper cell, providing a gas-tight seal, and backed up with a copper frame to provide strength against peeling under the strain due to the pressure differential. Sample gases passed from outside the cryostat to the cell via a stainless-steel tube that entered the cell on its top edge. Condensation of sample gases within the tube was prevented by a heater wound about the tube over its entire length inside the cryostat. Cooling of the cell was provided through its attachment to the cold finger on the cell's bottom edge. A heater mounted on the top edge of the cell served to ensure that the top of the sample, near the exit tube, was the warmest part and to allow the establishment of a temperature gradient down the sample during sample preparation. Sample temperature was measured with either carbon glass resistive thermometers or GaAlAs diode thermometers set into the edge of the copper cell. Temperatures down to about 4 K were attainable with this system.



### 3.2 Growing Cryocrystals

Common experience has shown that the best crystals are obtained by slowly freezing the liquid sample by cooling from the bottom, and allowing the solidifying front to pass upward through the sample. Visual inspection of the sample during its growth is essential, so that the temperature gradient and rate of change of temperature can be controlled by seeing exactly what part of the sample is freezing at any given time.

Samples in this work were always prepared by allowing ultra high purity gas from a clean gas handling system into the cell, which was maintained at a temperature approximately midway between the melting and boiling points. The sample cell was filled slowly, keeping the temperature from rising as the heat of vaporization was taken up. A large amount of heating power, typically 6 W, was applied with the cell top heater in order to establish a temperature gradient down the walls of the cell, enabling one to carefully control the solidification of the sample. By adjustment of the heating and cooling power, the boundary between liquid and solid was made to slowly sweep upward through the sample. After the sample was entirely solid, which typically took 4 hours, the thermal gradient was removed and the sample maintained at a temperature a few degrees below the melting temperature for several hours to allow the sample to anneal. Samples so produced were completely transparent, with no *visible* defects; however, it is known [20] that samples prepared in this way are polycrystalline, with grain dimensions on the order of 1 mm. Very slow crystal growth, much slower than used here, is required to prepare truly *single* crystals, even of much smaller size. The nature of the crystal structures was not further investigated.

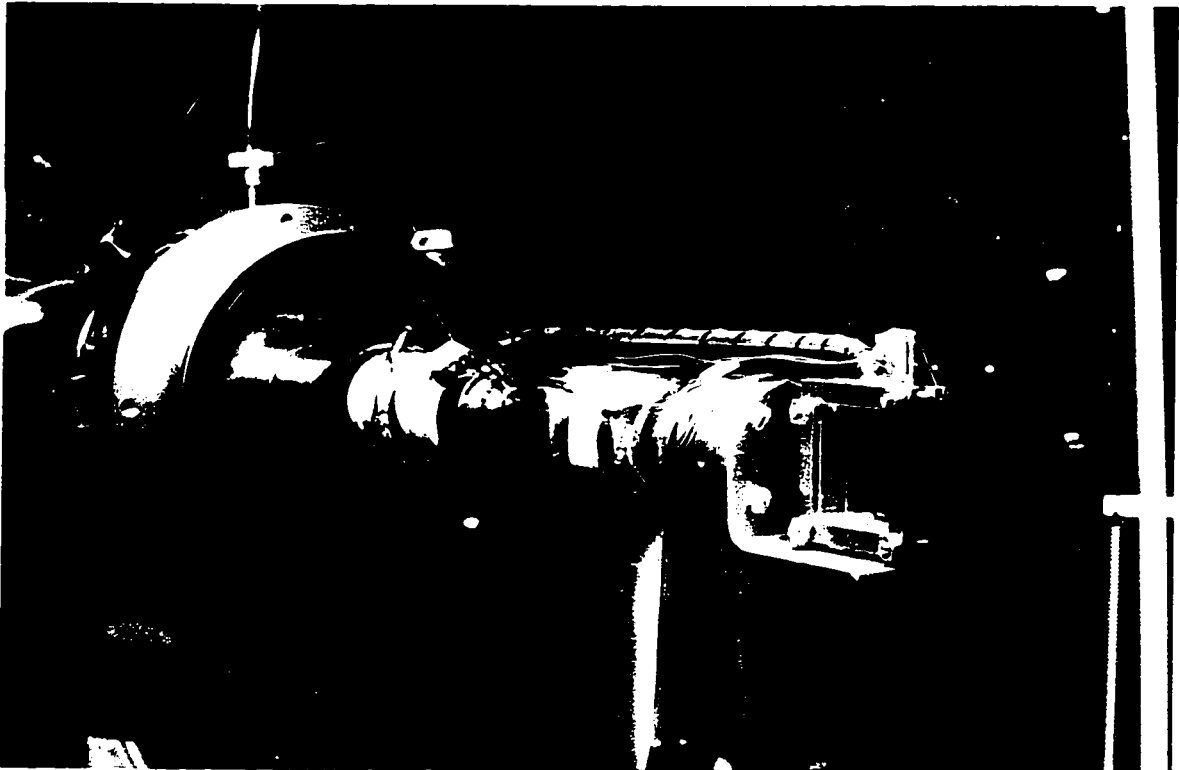


Figure 3.8: The interior parts of the coldfinger cryostat used for  $\mu SR$  experiments on solidified gases. The samples were condensed from the gas phase and frozen solid in the cell visible at the tip of the cold finger. Sample gas was allowed into the cell through the thin stainless tube, which was equipped with a heater to prevent blockages. (G.D. Morris)

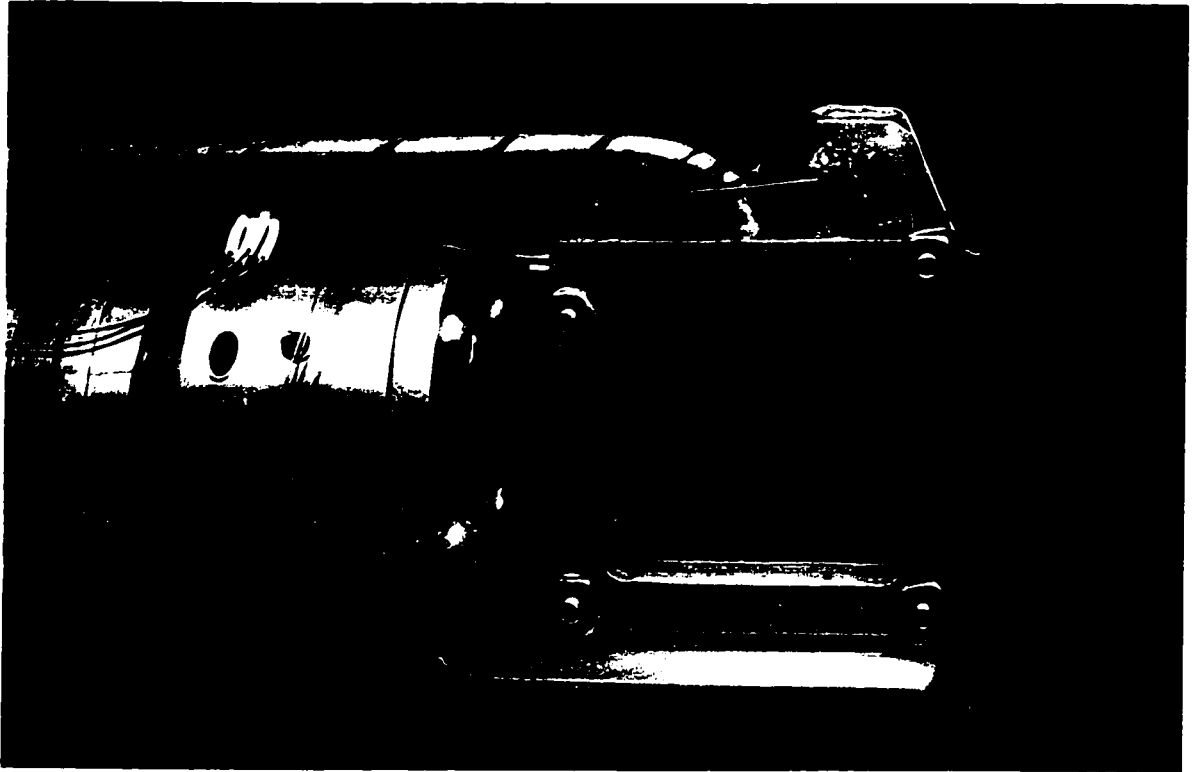


Figure 3.9: The sample cell used to condense gases to solids (approximately twice actual size), showing the attachment point to the cold finger and heater on the top of the cell. The flow of heat from top to bottom created a temperature difference of about 1 K down the cell walls. This is necessary to grow void-free crystals by ensuring that the sample freezes from the bottom up. The sample could be seen through the transparent mylar windows enclosing the front and back faces of the cell. (G.D. Morris)

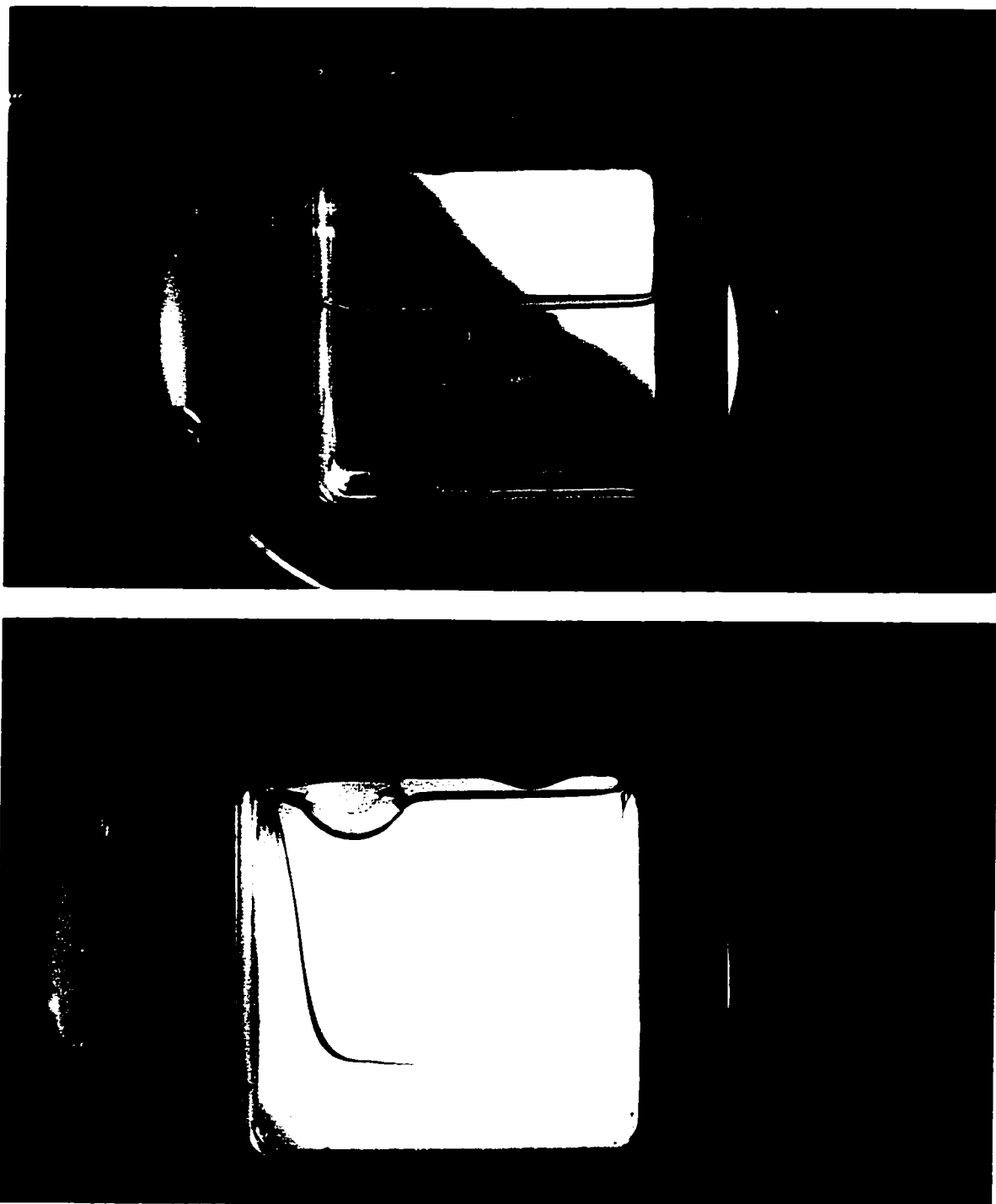


Figure 3.10: A sample of Ne being condensed and frozen; (a) The cell partially full of liquid Ne. (b) The cell full of Ne, some of which has solidified around the edges of the cell. (G.D. Morris)

### 3.3 Properties of Solid Nitrogen

Many properties of solid (and liquid) nitrogen are reviewed very thoroughly in an article by T.A. Scott [20]; the most important characteristics are briefly reviewed here.

The isolated nitrogen molecule  $\text{N}_2$  has dimensions, defined by the surface enclosing 95% of the electron density, of about  $3.39 \text{ \AA}$  diameter  $\times$   $4.34 \text{ \AA}$  in length. Spectroscopic studies of the vibrational (stretch) modes of the molecule indicate that in the condensed states the molecule is slightly distorted by interactions with neighbouring molecules.

Nitrogen exists as two stable isotopes - 99.63% is  $^{14}\text{N}$  with nuclear spin 1 and 0.37% is  $^{15}\text{N}$  with spin 1/2. With such a small fraction of  $^{15}\text{N}_2$  the properties of solid, natural  $\text{N}_2$  and solid pure  $^{14}\text{N}_2$  are virtually indistinguishable.

#### 3.3.1 Crystal Structures

Solid nitrogen has three known crystal structures - labelled  $\alpha$ -,  $\beta$ - and  $\gamma$ - $\text{N}_2$  - in the  $P - T$  plane. [20] The  $\gamma$  phase exists only under high pressures - greater than about 3500 atm, well beyond pressures attainable in thin-walled cells and is therefore not presently accessible with low energy surface muon beams.

The  $\alpha$  phase exists under equilibrium vapour pressure and at temperatures below  $T_{\alpha\beta}=36.61 \text{ K}$ , in which the  $\text{N}_2$  molecules are centred on the sites of an *fcc* lattice of space group  $\text{Pa}\bar{3}$ . In this structure the molecules are oriented (on average) lengthwise along body diagonals of the cubic cell. The x-ray structure yields a lattice constant  $a=5.660(2) \text{ \AA}$  at 20 K. [23]

Above  $T_{\alpha\beta}$ , also at low pressures, the  $\beta$  phase has the molecular *centres* on a *hcp* lattice of space group  $\text{P}6_3/\text{mmc}$ . The unit cell has dimensions  $a = 4.036 \text{ \AA}$  and  $c = 6.630 \text{ \AA}$ . [21] The molecules' *orientations* on this lattice are not fixed.

### 3.3.2 Librational Modes in Solid Nitrogen

The most important differences between the  $\alpha$  and  $\beta$  phases involve the librational motions of the  $\text{N}_2$  molecules. Motional narrowing of the nuclear quadrupole coupling by three orders of magnitude and disorder detected in the x-ray structure indicated that molecules in the higher temperature  $\beta$  phase do not have their orientations fixed with respect to the lattice: they are disordered by precession-like motion about the  $\hat{c}$  axis, with the molecular axes making an average angle of  $54.7^\circ$  to the  $\hat{c}$ -axis. [22]

Raman scattering studies have been able to measure the absorption lines corresponding to the high frequency ( $2200\text{--}2500\text{ cm}^{-1}$ ) molecular stretch mode and the lower frequency ( $<150\text{ cm}^{-1}$ ) librational and lattice modes at temperatures from 3.6 K to above the  $\alpha - \beta$  transition, under equilibrium vapour pressure. [24] As temperature is increased within the  $\alpha$  phase, the mean amplitude of librations away from the preferred orientations grows. This is apparent as a slight broadening of the molecular stretch line with increasing  $T$ , which is expected when the molecules are no longer in identical environments, beginning at about  $T=25\text{ K}$  and continuing into the  $\beta$  phase.

The low frequency lines, which are sharp at low temperatures in the  $\alpha$  phase, gradually become less distinct as the temperature rises to  $T_{\alpha\beta}$ , and become very broad features above  $T_{\alpha\beta}$ . This was interpreted as consistent with the build-up of large amplitude, anharmonic librations in the  $\alpha$  phase and a fully disordered, precessional motion in the  $\beta$  phase.

The disorder introduced by librations is of a short-ranged nature, but since these are soft modes, they are excited at relatively low temperatures - they fall among the acoustic phonons in the excitation spectrum of the lattice.

## Chapter 4

### Muonium formation in Insulators

A great deal of the early work and a much smaller fraction of current work in the field of  $\mu\mathcal{SR}$  deals with the question of what determines the final chemical state of the muon when it stops in a sample. This has been an important part of the development of  $\mu\mathcal{SR}$  as a tool, and recent developments may have an impact on both the interpretation of  $\mu\mathcal{SR}$  data in general and potential  $\mu\mathcal{SR}$  related technology (such as ultra-slow muon beams) in the near future.

This chapter lays the groundwork by first discussing models of muonium formation and evidence from conventional  $\mu\mathcal{SR}$  experiments that lead us to consider another mechanism – that electrons, stripped from atoms of the sample along the track of the muon, diffuse large distances through the sample to form muonium by recombination with the (positively charged) muon. Second, results from  $\mu\mathcal{SR}$  experiments in which an electric field was applied to the sample are presented. These experiments unambiguously demonstrate that, at least in some cryocrystals, muonium formation depends on the electron transport properties of the sample. It is quite likely that this is at least part of the answer to a long-standing puzzle regarding the differentiation of muons into diamagnetic and muonium fractions in so many (electrically) insulating materials - solids, liquids and gases.

This chapter is not an exhaustive discussion of electric-field  $\mu\mathcal{SR}$  (EF- $\mu\mathcal{SR}$ ). It is intended only to re-examine muonium formation in light of new results from cryocrystals, introduce the technique of using an electric field in  $\mu\mathcal{SR}$ , and to show that the amount

of muonium formed depends on the ability of radiolysis electrons, initially released by the muon much further from its final position than previously thought, to reach the stopped muon. Cryocrystals and cryoliquids have been instrumental in the discovery of this technique, so it is fitting that this be included in a thesis primarily concerned with muonium diffusion in cryocrystals.

#### 4.1 Models of Muonium Formation

Muonium is a light hydrogen-like neutral atom composed of an electron bound to a positive muon ( $\text{Mu} = e^- + \mu^+$ ), commonly produced when muons are implanted in non-metals including gases, liquids and solids ranging from semiconductors to fullerenes. One of the oldest unanswered questions in the field of  $\mu\text{SR}$  is “*How is muonium formed when a muon stops in one of these materials?*” The literature on this subject records a number of experiments devoted to answering this and the related question. “*What properties of the sample influence muonium formation?*” Until recently only reasoned guesses based on indirect evidence have been possible.

Following the first observation of muonium in highly purified water by  $\mu\text{SR}$  [7] the diamagnetic fraction (free  $\mu^+$  and  $\mu^+$ -substituted molecules) was measured in the presence of electron scavengers [8]. The increase in diamagnetic fraction with the concentration of  $\text{NO}_3^-$  ions was attributed to an increased probability of thermal, unsolvated muons becoming hydrated and subsequently forming  $\text{MuOH}$  by fast proton transfer, instead of capturing an electron to form muonium. One model proposed to explained this behavior pictured the muon losing kinetic energy near the end of the track by the creation of free electrons, ions and radicals in a radiation spur [8, 9]. The thermal muon in the vicinity of the terminal spur could then form muonium by simply capturing a free electron from among the spur products. This model was borrowed from the analogous theory of



positronium formation when positrons are injected into condensed media [10].

Another model of muonium formation proposed that the eventual distribution of muons among various states is determined by processes that occur while the  $\mu^+$  is still losing its initial kinetic energy [18, 11, 12, 13]. At high velocity (as from a surface muon beam) the muon should behave like any fast charged particle and undergo energy loss by Bethe-Bloch ionization of the medium: no significant amount of muonium should form until the kinetic energy has dropped to several tens of keV, where the muon velocity becomes comparable to the orbital velocity of electrons of the medium. Then charge exchange collisions become important as the muon undergoes a rapid series of several hundred electron pickup and stripping cycles, shedding energy each time atoms of the medium or the muonium is ionized.

At an energy of order 100 eV charge exchange is no longer dominant and the fraction of muonium at these energies is expected to be influenced by the relative electron affinities of the muon and atoms of the sample. In materials with ionization potentials smaller than that of muonium (13.5 eV) most muons are expected to emerge from this stage as hot muonium atoms. Further thermalization of both muons and muonium atoms will continue by elastic and inelastic collisions with neutral atoms and hot atom reactions which may, depending on the stopping medium, produce  $\mu^+$ -substituted molecules and/or molecular ions. The final distribution of muon charge states will be determined by the reactions that  $\mu^+$  and Mu undergo in the last few steps. In low pressure rare gases there is a strong correlation between muonium formation and ionization potential of the gas, which seems to support this model.

The principal distinction between these two models lies chiefly in *when* and *at what energy* muonium is formed. “Hot” muonium formation is a “prompt” process, occurring during a time when the muon is rapidly losing energy, within a few tens of ps after entering a condensed sample. Muonium formation *after* the muon has come to thermal

equilibrium with its surroundings requires time for electrons to diffuse to the muon, and is therefore termed “delayed” muonium formation.

## 4.2 Muonium Formation and Electron Transport in Insulators

### 4.2.1 Muonium in Solid Nitrogen

Muon spin relaxation experiments were carried out on samples of solid, pure nitrogen using conventional time-differential transverse field (TF) techniques. In the low temperature  $\alpha$  phase a large muonium signal and a smaller diamagnetic muon signal together account for virtually all the muon polarization. In  $\beta$ - $N_2$  and  $\ell$ - $N_2$  some of the diamagnetic fraction appears as an additional fast-relaxing signal (with initial asymmetry  $A_D^f$  and relaxation rate  $\lambda_D^f$ ) and all the asymmetries are temperature dependent. The total asymmetry therefore has the form

$$A(t) = A_{Mu} \exp(-\lambda_{Mu}t) \cos(-\omega_{Mu}t + \phi_{Mu}) + [A_D^s \exp(-\lambda_D^s t) + A_D^f \exp(-\lambda_D^f t)] \cos(\omega_D t). \quad (4.1)$$

The slowly-relaxing diamagnetic asymmetry  $A_D^s$  and muonium asymmetry  $A_{Mu}$  obtained are shown in Fig. 4.11. The most striking feature in the temperature dependence of these is the obvious anticorrelation between them at temperatures near  $T_{\alpha\beta}$ , suggesting the presence of competing processes in which the stopping muon either captures an electron to form muonium, or eventually becomes incorporated into a molecular ion. Since only half of the muonium asymmetry is experimentally observable, (the other half oscillating too fast to be resolved - see Appendix A) loss of some of the diamagnetic species to muonium formation results in an increase in the muonium asymmetry half as large. The total  $A_D^s + A_D^f + 2A_{Mu}$  is nearly temperature independent. Since the free

electron mobility in  $\beta$ -N<sub>2</sub> increases with temperature below  $T_{\alpha\beta}$  like the muonium fraction. this strongly suggests that *transport* of electrons through the lattice is involved in muonium formation in solid nitrogen. The electron mobility measured in solid nitrogen by Loveland *et al.* is shown in Fig. 4.12. From 63 K down to 53 K the mobility  $\mu_e(T)$  is constant at about  $1.7 \times 10^{-3} \text{ cm}^2\text{s}^{-1}\text{V}^{-1}$ ; it then decreases gradually to half this value at  $T_{\alpha\beta}$ [19]. The available mobility data below  $T_{\alpha\beta}$  doesn't reveal the trend in  $\alpha$ -N<sub>2</sub> but it does indicate that the mobility is sharply increased to about  $2.0 \times 10^{-3} \text{ cm}^2\text{s}^{-1}\text{V}^{-1}$  in the  $\alpha$  phase. Over this range in  $T$  the muonium asymmetry changes by about the same fraction as the electron mobility, at least in the  $\beta$  phase.

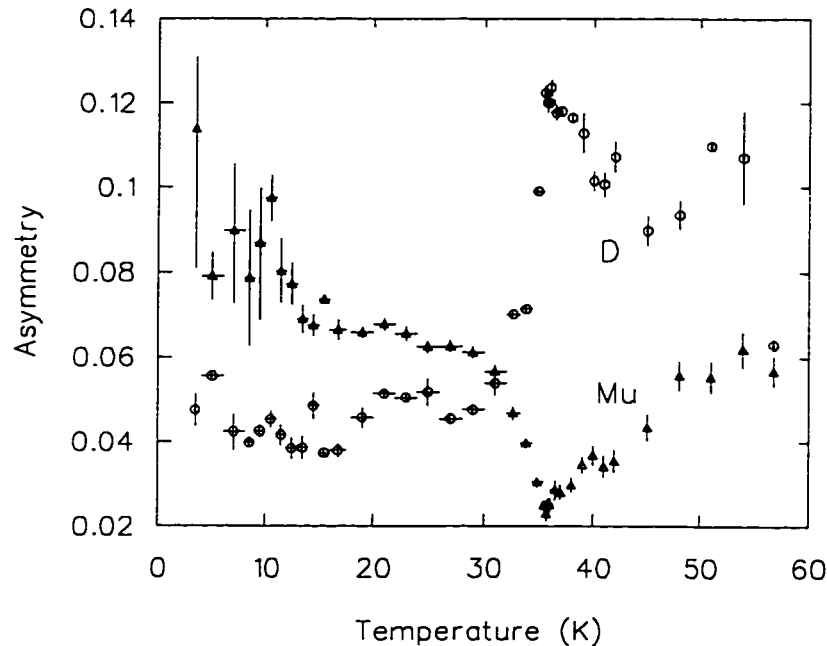


Figure 4.11: Muonium and slowly relaxing diamagnetic asymmetries measured in solid nitrogen.

### 4.2.2 Muonium in Neon

Muonium was found to be abundant in solid Ne as a long-lived species, amounting to 80% of the total asymmetry. In liquid Ne muonium accounts for about 5% of the asymmetry. The complete absence of muonium in Ne gas was once considered a key argument that the crucial factor to muonium formation was the relative size of the ionization potential of the stopping medium compared to that of muonium. [18]. Clearly, this is not the complete picture, at least for solid rare gases. Ne has a vacuum ionization potential of 22 eV, well above that of muonium, so that once the muon kinetic energy has fallen below about 8 eV, it is impossible for muonium to be formed by a hot muon colliding with a Ne atom. Likewise, once the muon has reached thermal equilibrium with

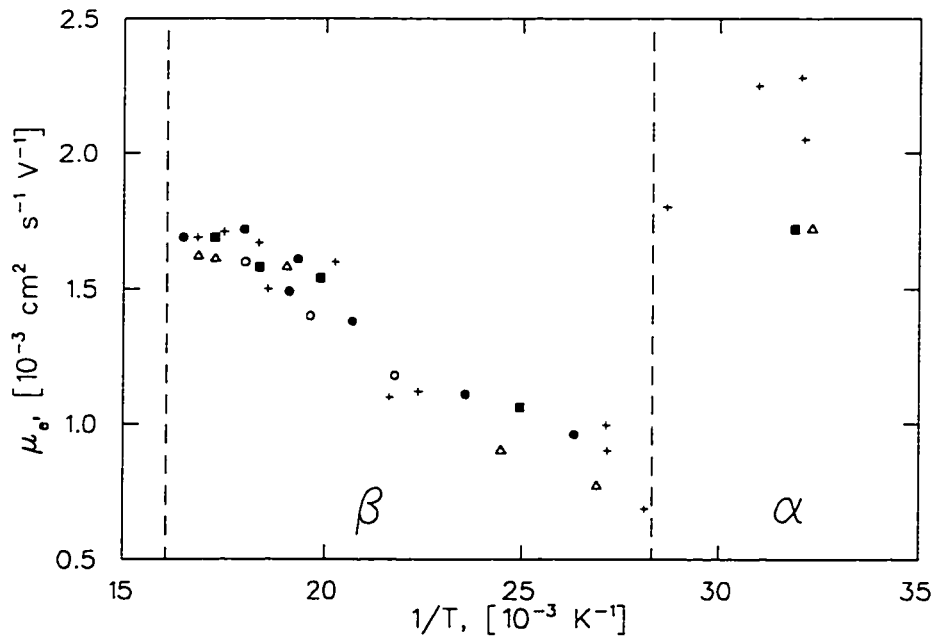


Figure 4.12: Electron mobility in solid nitrogen measured by Loveland *et al.* [19] using a direct time-of-flight method. Various symbols indicate different samples.

the lattice, muonium cannot be formed by simply abstracting an electron from a nearby atom. Formation of muonium while the muon is still energetic ought to be unaffected by the phase of the material, at least in the condensed phases. Since muonium is abundant only in *solid* Ne, it appears to be a result of properties unique to the solid phase. Free electrons in solid Ne are known to have an extremely high mobility, on the order of 2000 cm/V-s, about the same as in typical semiconductors, and 6 orders of magnitude less in the liquid phase where they form voids in the liquid due to their zero-point motion pushing Ne atoms apart. Taken together the evidence indicates that it is the electron transport properties of the crystalline state that enable formation of some of the muonium in solid N<sub>2</sub> and almost all the muonium in solid Ne.

### 4.3 $\mu\mathcal{SR}$ in Electric Fields

A fundamental experiment that has the potential to show whether motion of free electrons is involved in Mu formation is to measure the muonium polarization function in a sample to which an external electric field has been applied. The idea is very simple – if an external electric field does have an effect, then the muonium must be formed from a free electron and muon that are initially well separated. When muonium is formed *directly* by collisions of energetic muons with neutral atoms, the muon and electron are never separated by a distance sufficient to allow a modest external field to have much effect against the overwhelming coulomb force between charged particles in close proximity.

Previously, only a very few  $\mu\mathcal{SR}$  experiments have been performed in which samples were subjected to electric fields. Ito *et al.* investigated the effect of an external electric field on the muonium signal in liquid hydrocarbons with fields up to 20 kV/cm and in fused quartz up to 60 kV/cm, observing no effect on either the asymmetry or relaxation

rate. [14, 15]

### 4.3.1 Liquid Helium in an Electric Field

The first  $\mu SR$  experiments in which an external electric field had a measurable effect was performed by Krasnoperov *et al.* in superfluid and normal helium. [28, 26, 27] In the superfluid, in zero electric field, about 90% of the muons formed muonium atoms. The effect of an external electric field was asymmetric: a field along the initial muon direction sharply decreased the muonium amplitude. In the opposite direction the amplitude first reached a maximum (at 50V/cm) then decreased more gradually as the electric field increased. In normal liquid He the mobilities of both positively and negatively charged particles are much lower and consequently the formation times longer. A small muonium signal was detected in a very weak magnetic field of 0.4 G. With an electric field pushing the charged particles together, the formation time was reduced so that muonium formed over a shorter time with less dephasing, resulting in a larger muonium amplitude. For both of these samples the results were interpreted in terms of the motion of a positively charged helium “snowball” and a negatively charged “bubble” that form around the muon and electron respectively. It was concluded that the electrons were distributed asymmetrically with respect to the thermal muon at the end of the muon’s track. It was estimated that the muons came to rest some 300-400 nm further downstream than the electrons.

In the present work this technique has been extended to other samples, demonstrating muonium formation via the convergence of electrons and muons in solids for the first time. The principal result is definitive data showing that the muon is *not* isolated from its own radiolysis track products, and that electrons from the track *do* reach the muon in insulating solids. We now have strong evidence that muonium is often formed as a result of recombination with these electrons and some estimates of the distances and timescales

involved.

### 4.3.2 Solid Nitrogen in an Electric Field

An electric field was applied to a sample of solid nitrogen ( $s\text{-N}_2$ ) by the addition to the sample cell of two fine wire grids outside the sample cell spaced 3.0 mm from the mylar cell windows. High positive and negative voltages (with respect to ground) were then applied to the grids to establish an electric field through the sample. Conventional time-differential spectra were measured by TF  $\mu\text{SR}$  with the electric field either along or opposed to the direction of the incoming muon beam, producing the asymmetries shown in Fig. 4.13. A positive  $E$  denotes an electric field parallel to the muon's momentum (the conventional forward direction); negative  $E$  in the opposite direction. The magnitude  $E$  is simply the potential difference between the grids divided by the separation of 1.2 cm.

The results unambiguously indicate *directional* asymmetry in the effect of an electric field. With  $\vec{E}$  in the  $+\hat{z}$  direction the muon fraction was increased and muonium decreased. With the direction of the electric field reversed, the asymmetries change in the opposite way. This is consistent with a mechanism for muonium formation in which free electrons generated in the muon's radiolysis track neutralize the positive muon. Applying an external electric field drives these electrons either toward or away from the stopped muon, increasing or decreasing the likelihood of muonium formation by putting more or fewer electrons in the vicinity of the thermal muon. Muonium formation in this way is always exothermic and therefore can proceed after the muon has come to thermal energies. Assuming this model, we can conclude that the electrons originate predominantly *behind* the muon. This model implies that the muon stops downstream from the end of its ionization track, more or less preserving its direction of travel while slowing down.

In order for the external field to have much effect on the trajectory of electrons in the Coulomb fields of nearby ions and the muon, the electron that eventually reaches the

muon must be far enough away from them, at least for part of the time-of-flight. One way for this to happen may result from the end of the cyclic charge exchange part of the muon track. A hot muonium atom can undergo a collision with a neutral atom and ionize itself, leaving the electron in the lattice while the bare muon can continue on with the last few eV and eventually come to rest further down stream. In this picture neither the electron or muon are in the immediate vicinity of any other ion. Most importantly, this electron that has been carried in a muonium atom away from the ion from which it came is the closest one to the muon and therefore is the electron that reaches the thermal muon first. This model implies that the direction of travel of the muon, at the very end of the track, is still on average in the direction of the muon beam.

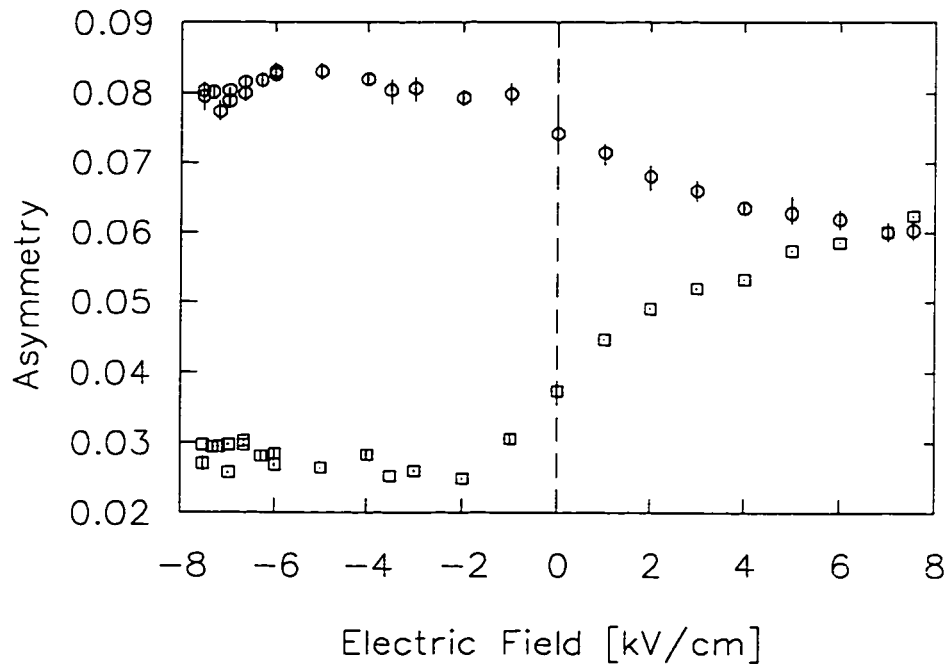


Figure 4.13: Slowly relaxing diamagnetic asymmetry  $A_S$  and muonium asymmetry  $A_{Mu}$  (boxes and circles respectively) measured in a sample of solid nitrogen at  $T=20$  K with an external electric field applied either along ( $E > 0$ ) or opposite ( $E < 0$ ) to the incoming muon beam direction.



In order for an external electric field to have an appreciable effect on the motion of electrons in the vicinity of the muon, the magnitude of the external electric field would have to be comparable to (or larger than) the electric field due to the muon's charge. One can then estimate the typical initial distance between the electron and muon from the electric field dependence of the asymmetries. An electric field of about 3 kV/cm falls midway on the curve between  $E = 0$  and saturation of the effect. Taking the electric field of the muon at the electron to be  $E_0 = 3.0$  kV/cm, one may conclude that the typical electron-muon distance is approximately  $R = \sqrt{e/\epsilon E_0} = 60$  nm, in which  $\epsilon = 1.3$  is the dielectric constant of solid nitrogen.

#### 4.4 Delayed Muonium Formation

Muonium formation involving electrons originating in the radiolysis track depends on the transport of these electrons to the muon under the influence of their mutual Coulomb attraction and any external fields. The associated time-of-flight can be large enough to have an observable effect on timescales accessible by  $\mu\mathcal{SR}$  if the initial separation is great enough.

While a muon awaits the arrival of an electron its spin will precess in an external transverse magnetic field at the muon Larmor frequency  $\omega_\mu$ , and if it decays during this time it will contribute to the diamagnetic signal. Those muons that do not decay while in a diamagnetic state will, upon forming muonium, begin to precess in the opposite sense at the characteristic frequencies  $\omega_{12}$  and  $\omega_{23}$ , possibly contributing to the muonium signal instead. (A complete discussion of the muonium signal is given in Appendix A. In weak fields we may characterize the muonium signal by the average frequency  $\omega_{\text{Mu}}$ .) The elapsed time between muons entering the sample and the arrival of electrons at the muons will have some distribution, so the coherent diamagnetic polarization will be converted

to muonium polarization over a range of times, with a corresponding distribution in the apparent initial phase of the muonium precession. Since  $\omega_\mu$  is very small compared to the muonium precession frequencies, the dephasing is almost entirely due to precession in the higher frequency final state starting at different times. The conversion of coherent muon polarization to partially dephased muonium polarization results in a measurable loss of asymmetry whenever the formation time is comparable to or larger than the muonium precession period. Delayed muonium formation is experimentally observable in principle in the shape of the diamagnetic relaxation function  $G_\mu(t)$ , but it is more easily observed in the resulting muonium amplitude and phase after all Mu formation is complete. A stronger magnetic field results in proportionally more dephasing and therefore a reduced polarization of the delayed part of the muonium ensemble. One can thus estimate the characteristic time of muonium formation from the magnetic field dependence of the amplitude of the muonium signal.

At any time the instantaneous polarization is the vector sum of all muon spins present including diamagnetic, delayed and prompt muonium. If the distribution of formation times is  $D(\tau)$  [the probability of muonium formation between times  $\tau$  and  $\tau + d\tau$  is  $D(\tau) d\tau$ ] then the total polarization at time  $t$  is

$$\begin{aligned} \tilde{P}(t) = & (1 - f_0) \left[ 1 - \int_0^t D(\tau) d\tau \right] e^{i\omega_\mu t} G_\mu(t) \\ & + \frac{1}{2} (1 - f_0) \int_0^t e^{-i\omega_{\text{Mu}}(t-\tau)} G_{\text{Mu}}(t - \tau) D(\tau) e^{i\omega_\mu \tau} G_\mu(\tau) d\tau \\ & + \frac{1}{2} f_0 e^{-i\omega_{\text{Mu}} t} G_{\text{Mu}}(t), \end{aligned} \quad (4.1)$$

in which  $f_0$  is the prompt muonium fraction. For clarity here we are ignoring the splitting of the muonium signal that would be apparent in transverse fields greater than about 10 G. In fitting the data, one must replace the single muonium signal above with the usual sum of two components at frequencies  $\omega_{12}$  and  $\omega_{23}$ . The first term in Eq. (4.1) is the coherent diamagnetic polarization remaining at time  $t$ . The second term is the sum

over all phases of the accumulated *delayed* muonium ensemble. The third term is the prompt muonium polarization.

After all muonium formation is complete, the resulting muonium precesses at the same frequency and undergoes spin relaxation according to the same function as the prompt muonium fraction. In this way the long-time muonium ensemble can be characterized by a single amplitude and phase. Figure 4.14 shows the asymmetry of the muonium ensemble (the total muonium signal) in liquid nitrogen at  $T = 75$  K in various transverse magnetic fields, obtained by fitting the  $\mu\mathcal{SR}$  spectra starting at  $t = 50$  ns. The solid line is the empirical maximum asymmetry  $A_0$  multiplied by the theoretical polarization in Eq. (4.1), and in which the distribution of formation times is

$$D(\tau) = \frac{1}{\tau_{\text{del}}} e^{-\tau/\tau_{\text{del}}}.$$

[Although it is possible in principle to obtain  $D(\tau)$ , which may be a complicated function of the spatial distribution of electrons, the present data are not sufficient to reveal the real shape of  $D(t)$ .] The characteristic formation time  $\tau_{\text{del}}$  estimated in this way was 14(4) ns and the muonium asymmetry (in the limit of  $B \rightarrow 0$ ) resulting from delayed formation was

$$A_{\text{del}} = \frac{A_0}{2} \int_0^\infty D(\tau) d\tau = 0.011(2),$$

while prompt muonium contributed  $A_0 f_0 = 0.038(2)$ . From this we conclude that delayed formation accounts for at least 22% of the muonium in liquid nitrogen. (Muonium formed by the “delayed” process within a time very short in comparison to the precession period is indistinguishable from the prompt hot muonium fraction, so the “delayed” fraction could be larger.)

Similar experiments on solid nitrogen and rare gas solids have not shown magnetic field dependence of asymmetries, presumably because the time of flight is too short due to greater electron mobility and/or reduced distance.

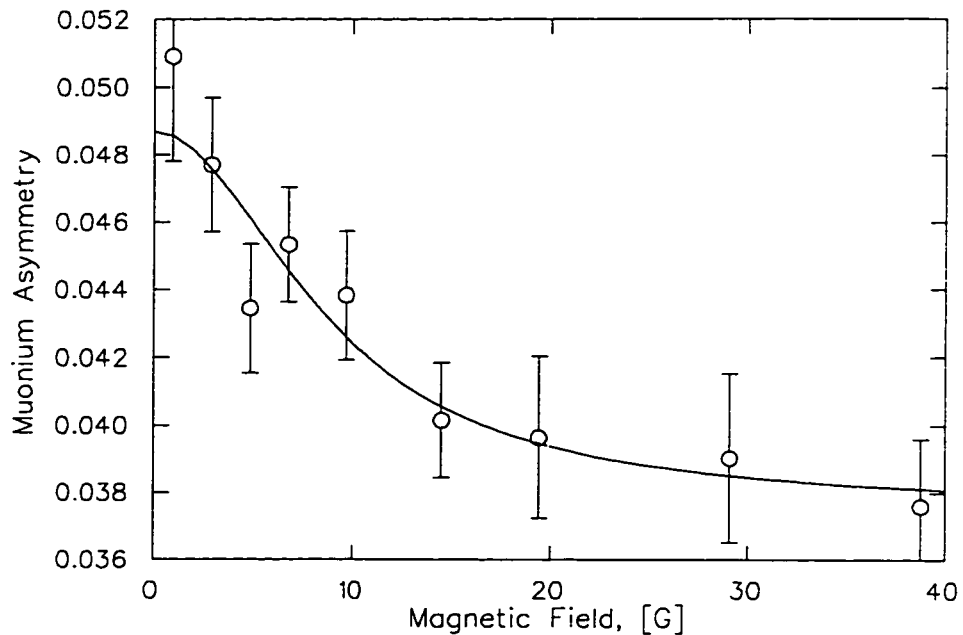


Figure 4.14: Total muonium asymmetry measured in liquid nitrogen ( $T=75$  K) at long times where delayed muonium formation has ceased. The solid line represents a fit to theory, yielding a characteristic muonium formation time of  $0.014(4)\mu\text{s}$ .

If the electrons were initially much further away from the muon than the width of their spatial distribution, then the maximum muonium formation rate could be displaced from  $t = 0$  by an amount  $\tau_0$ . In this case, if the prompt muonium had time to precess one or more full revolutions while the electrons were diffusing to the muon, the total muonium polarization would be a periodic function of magnetic field. This would yield a direct measurement of the formation time

$$\tau_0 = \frac{1}{2\pi\gamma_{\text{Mu}}B},$$

where  $B$  is the period in magnetic field. Such convincing evidence of delayed muonium formation has not yet been observed, but is possible in principle.

#### 4.5 Implications of Delayed Muonium Formation for $\mu\mathcal{SR}$

Until now it has always been assumed that the muon could be considered an extremely dilute impurity, inserted one at a time into a sample without much affecting the bulk of the sample, and certainly not beyond the immediate vicinity of the muon. We now know that the electrons generated along the muon track *do* interact with the muon on time scales important to  $\mu\mathcal{SR}$ . It is probable that in all insulators, including semiconductors, at least some of the muonium results from the delayed formation process.

There are two principal concerns related to this. First, there is the question of how much the muon and muonium signals in various (insulating) materials are affected by direct interaction with the stray electrons. For both muons and muonium, the most obvious affect would be a contribution to the relaxation rate of the polarization function. Second, the bulk properties of the sample in the vicinity of these stray electrons may also be affected, and have an indirect influence on the muon or muonium signals. In both situations it is possible that a misleading result could be obtained in the measurement of other unrelated phenomena. At the present time neither of these potential problems can be ruled out. More electric field experiments on a variety of “conventional” samples will be necessary to determine the circumstances under which such effects may safely be ignored, but until such time that this is fully understood, practitioners of  $\mu\mathcal{SR}$  in insulators should bear this in mind.

## Chapter 5

### Quantum Diffusion I: Theory

#### 5.1 An Introduction to Quantum Diffusion in Insulators

The theory of quantum tunnelling diffusion in the presence of strong coupling to lattice excitations has been developed in large part by Holstein, [31] Andreev and Lifshitz, [32] Flynn and Stoneham, [33] and most recently by Kagan, Klinger, Maksimov and Prokof'ev. [34, 35, 36, 40] The derivation of the principal equations which appear in the literature regarding one- and two-phonon mediated tunnelling diffusion is outlined here. Some details are omitted in the interest of keeping this discussion to a readable length but these may be found in the review articles, most recently by Kagan and Prokof'ev. [53] Although much of this has been published previously, the literature lacks a concise treatment of quantum diffusion that would serve experimentalists well. It is hoped that a short review of this model will serve as a guide to the uninitiated in understanding the theory, and in particular the origin of temperature dependences which one can measure.

We are concerned here with the tunnelling diffusion of a light, neutral interstitial atom in an otherwise (nearly) perfect insulating crystal. The picture one should have in mind is of the particle, such as a muonium or hydrogen atom, occupying interstitial sites between atoms of an otherwise regular lattice at temperature  $T$ . The interstitial's potential is minimized by nearby lattice atoms relaxing slightly from their usual equilibrium sites to take on a new configuration where each atom resides in a potential well not very different from the perfect lattice. In the absence of a Coulomb interaction with conduction

electrons, the dependence of the interstitial's potential on the displacement of nearby lattice atoms from their equilibrium positions is the principal interaction. The interstitial then is in a potential minimum partly of its own making and is therefore said to be self-trapped. The neutral interstitial together with the associated lattice distortion is called a *small polaron*. For example, electrons in semiconductors can induce a small polaron which extends over many more lattice sites and results in a large increase in effective mass.

Owing to the mass of our interstitial Mu atom (much heavier than electrons) the characteristic tunnelling bandwidth  $\Delta_0$  is small compared to energies of typical lattice excitations  $\omega_D$  (we set  $\hbar = k_B = 1$  throughout this chapter) and, for the experiments described here, also small compared to the temperature of the lattice. At low temperatures where the number of lattice excitations is sufficiently small, the interstitial atom can propagate almost freely in a band-like (Bloch) state. At higher temperatures scattering with lattice excitations (phonons) occurs, more so as the number of excitations increases, and in this regime the diffusion rate decreases with increasing temperature. This results from the “dynamical destruction of the band” when there are sufficient numbers of phonons that there is a significant probability of scattering during the time the interstitial spends at a given site. Under these conditions diffusion of the interstitial can still proceed via quantum tunnelling through the barrier, though the scattering results in the loss of phase coherence of the particle wavefunction. Therefore, in this regime the particle diffusion is said to be incoherent.

One can imagine that if the interstitial atom diffused to a site where the surrounding atoms were initially unadjusted to its presence, the lattice would eventually respond, on a time scale set by the lattice vibrational modes, by re-establishing the polaron at the new site. It is much easier for the interstitial to diffuse by tunnelling from one site to another if the lattice fluctuates into a configuration so that, effectively, the entire polaron

tunnels to the new site. When a particular fluctuation of the lattice brings the potential at an adjacent site into resonance with the interstitial's present potential, the interstitial can tunnel to the new site through the barrier. Transient configurations may also lead to an increase of the tunnelling rate by shifting the atoms that define the potential barrier to positions where the height and width of the barrier are reduced. In this model thermally excited fluctuations of lattice atoms' positions in these ways will play an important role in determining the tunnelling rate. In both the low- and high-temperature regimes it is through the temperature dependence of the phonon population that one can indirectly vary the particle's diffusion rate. This provides us with the principal experimental handle on the problem.

Generally the spectrum of lattice excitations can be divided into two parts: those that follow the interstitial particle adiabatically and those that are too slow to respond before the particle has moved. In the case of a light interstitial such as muonium in a lattice of much heavier atoms, the entire phonon spectrum must be considered non-adiabatic. The interstitial can easily follow the motion of the atoms, but the lattice can only respond slowly to the motion of the muonium atom, and therefore sees the muonium at its average position at the centres of the (slightly modified) potential wells. We can therefore treat the problem by writing the wave function of the system as a product of fast intra-well states and slow environmental states in the adiabatic approximation.

We shall assume that the diffusing particle occupies the lowest energy state of the intrawell part of the wave function, so that the overall temperature dependence of the hop rate is due to the overlap of states of the lattice. Intrawell degrees of freedom will play essentially no role since they are associated with relatively high energy excitations. We are therefore interested in calculating the transition rate  $W_{12}$  from state  $\Psi_n(\mathbf{R}_1)$ , the wave function of the lattice when the particle is at  $\mathbf{R}_1$ , to  $\Psi_m(\mathbf{R}_2)$ , where  $m, n$  label the configuration of the lattice.



## 5.2 Renormalization of the One-Phonon Interaction

We would like to be able to write the wave functions of the lattice with the particle present,  $\Psi_m(\mathbf{R}_i)$ , in terms of the normal modes of the lattice without an interstitial. However,  $\Psi_m(\mathbf{R}_i)$  is an eigenfunction of the Hamiltonian which includes the lattice-interstitial interaction.

$$\begin{aligned}\mathcal{H} &= \mathcal{H}_0 + \mathcal{H}_{\text{int}} \\ &= \sum_{\beta} \omega_{\beta} (b_{\beta}^{\dagger} b_{\beta} + 1/2) + \mathcal{H}_{\text{int}}\end{aligned}\quad (5.1)$$

while the wave functions of the lattice without the interaction  $\Psi_n^{(0)}$  is an eigenfunction of  $\mathcal{H}_0$  - the Hamiltonian of the bare lattice.

By performing a transformation of the one-phonon interaction we can write these wave functions in the same basis, allowing us to evaluate the overlap,

$$\langle \Psi_n(\mathbf{R}_i) | \Psi_m^{(0)} \rangle.$$

We define the *polaron operator*  $\hat{\Lambda}$ , a unitary operator, relating these two complete sets of wave functions by the sum

$$\Psi_m(\mathbf{R}_i) = \sum_n \Lambda_{nm}(\mathbf{R}_i) \Psi_n^{(0)}.\quad (5.2)$$

The operator  $\Lambda(\mathbf{R}_i)$  here describes, in terms of the normal modes of the lattice, how the lattice wave functions change when the lattice responds to the presence of the interstitial at site  $\mathbf{R}_i$ .

Overall, the method of calculating the interstitial diffusion rate will be to describe the shifted atomic positions in both the initial and final states in terms of linear combinations of non-interacting environmental states, which include temperature-dependent numbers of phonons. The overlap between initial and final states is then given by the coefficients

in these sums. Most of the following derivation will be the evaluation of the temperature dependence of these coefficients.

Fermi's Golden Rule then gives the transition rate

$$W_{12} = 2\pi\Delta_0^2 \sum_{mn} \left| \langle \Psi_n^{(0)} | \Lambda^\dagger(\mathbf{R}_2) \Lambda(\mathbf{R}_1) | \Psi_m^{(0)} \rangle \right|^2 \delta(E_n - E_m) \quad (5.3)$$

We will consider two cases of coupling to lattice excitations - corresponding to the linear and quadratic terms of a Taylor expansion of the Hamiltonian - which govern the behavior at high and low temperatures respectively. In this theory, displacements of atoms from their equilibrium positions in a harmonic potential are being written in terms of the normal modes of the lattice.

Let us first consider a very simple example to introduce the idea of writing oscillator displacement in terms of operators. In general, the Hamiltonian of a harmonic oscillator is the sum of kinetic and potential energies

$$\mathcal{H} = \frac{p^2}{2m} + \frac{m\omega^2 q^2}{2} \quad (5.4)$$

$$= \omega(a^\dagger a + 1/2) \quad (5.5)$$

where  $p$  and  $q$  are the momentum and oscillator displacement and the raising and lowering operators are defined as

$$\begin{aligned} a^\dagger &= \sqrt{\frac{m\omega}{2}} q + i\sqrt{\frac{1}{2m\omega}} p \\ a &= \sqrt{\frac{m\omega}{2}} q - i\sqrt{\frac{1}{2m\omega}} p. \end{aligned} \quad (5.6)$$

It follows that we can write the displacement of the harmonic oscillator from equilibrium, in terms of these operators,

$$q = \sqrt{\frac{1}{2m\omega}} (a + a^\dagger). \quad (5.7)$$

Analogously, the displacement of atoms in a lattice can be written, in terms of a sum over the phonons present,

$$q(\mathbf{R}) = \sum_{\beta} \sqrt{\frac{1}{2M\omega_{\beta}}} (b_{\beta} + b_{-\beta}^{\dagger}) e^{i\mathbf{k}_{\beta} \cdot \mathbf{R}}. \quad (5.8)$$

in which  $b_{\beta}^{\dagger}$  ( $b_{\beta}$ ) is the operator that creates (annihilates) a phonon of frequency  $\omega_{\beta}$ , where  $\pm\beta = (\pm\mathbf{k}, \lambda)$ , the wavevector and branch index respectively.

### 5.3 Linear Coupling; One-Phonon Diffusion

In the case of a particle-phonon coupling linear in  $(b_{\beta} + b_{-\beta}^{\dagger})$  we write the Hamiltonian of the excitations of the lattice plus the interaction between the lattice atoms and the interstitial muonium (which, in the adiabatic approximation is at the centre of the well, so this Hamiltonian depends on displacements of the lattice atoms only)

$$\mathcal{H} = \mathcal{H}_0 + \mathcal{H}_{\text{int}} = \sum_{\beta} \omega_{\beta} (b_{\beta}^{\dagger} b_{\beta} + 1/2) + \sum_{\beta} C_{\beta} (b_{\beta} + b_{-\beta}^{\dagger}), \quad (5.9)$$

where the sum is over all phonons present. The coupling constant  $C_{\beta} \propto \sqrt{\omega_{\beta}}$  governs the strength of the interaction with the interstitial. [54, 53]

The effect of the polaron deformation and the origin of the associated trapping potential become apparent in calculating  $\Lambda_{nn}$ . We start by using a normal oscillator shift  $e^{\hat{S}}$  in which

$$\hat{S} = \sum_{\beta} \left( \frac{C_{\beta}^*}{\omega_{\beta}} b_{\beta}^{\dagger} - \frac{C_{\beta}}{\omega_{\beta}} b_{\beta} \right) \quad (5.10)$$

to define new operators  $\bar{b}_{\beta}, \bar{b}_{\beta}^{\dagger}$ ,

$$\bar{b}_{\beta} = e^{\hat{S}} b_{\beta} e^{-\hat{S}} = b_{\beta} - \frac{C_{\beta}^*}{\omega_{\beta}} \quad (5.11)$$

$$\bar{b}_{\beta}^{\dagger} = e^{\hat{S}} b_{\beta}^{\dagger} e^{-\hat{S}} = b_{\beta}^{\dagger} - \frac{C_{\beta}}{\omega_{\beta}}. \quad (5.12)$$

Substituting these operators into the Hamiltonian, Eq. (5.9) becomes (noting that  $C_\beta^* = C_{-\beta}$ )

$$\mathcal{H} = \sum \omega_\beta (\bar{b}_\beta^\dagger \bar{b}_\beta + 1/2) - \frac{|C_\beta|^2}{\omega_\beta} \quad (5.13)$$

which simply corresponds to a new set of harmonic oscillators with a shift in energy, but the one-phonon interaction has now been eliminated.

The wave functions we need to construct are then

$$\Psi_n(\mathbf{R}_i) = e^{-\hat{S}} \Psi_n^{(0)} \quad (5.14)$$

$$= \exp \left\{ - \sum_\beta \left( \frac{C_\beta^*(\mathbf{R}_i)}{\omega_\beta} b_\beta^\dagger - \frac{C_\beta(\mathbf{R}_i)}{\omega_\beta} b_\beta \right) \right\} \Psi_n^{(0)}. \quad (5.15)$$

We are now able to write the matrix elements of  $\hat{\Lambda}$

$$\Lambda_{nm} = \langle \Psi_n^{(0)} | \exp \left\{ - \sum_\beta \frac{C_\beta^*}{\omega_\beta} b_\beta^\dagger - \frac{C_\beta}{\omega_\beta} b_\beta \right\} | \Psi_m^{(0)} \rangle. \quad (5.16)$$

The *polaron effect* corresponds to the diagonal elements  $\Lambda_{nn}$ ,

$$\Lambda_{nn} = \exp \left\{ - \frac{1}{2} \sum_\beta \frac{|C_\beta|^2}{\omega_\beta^2} (2N_\beta + 1) \right\} \quad (5.17)$$

which, with the number of phonons of frequency  $\omega_\beta$  now a function of temperature

$$\langle b_\beta^\dagger b_\beta \rangle = N_\beta(T) \sim \frac{1}{e^{\omega_\beta/T} - 1}, \quad (5.18)$$

reduces to (suppressing an overall constant)

$$\Lambda_{nn} = \exp \left\{ - \sum_\beta \frac{|C_\beta|^2}{2\omega_\beta^2} \coth \left( \frac{\omega_\beta}{2T} \right) \right\}. \quad (5.19)$$

It is usual in the literature to define the “polaron exponent” as the sum

$$\phi(T) = \sum_\beta \frac{|C_\beta|^2}{2\omega_\beta^2} \coth(\omega_\beta/2T), \quad (5.20)$$

so that the polaron effect manifests itself as a renormalization (reduction) of the raw tunnelling bandwidth  $\Delta_0$

$$\tilde{\Delta}(T) = \Delta_0 e^{-\phi(T)}. \quad (5.21)$$

#### 5.4 Barrier Fluctuations

A second effect, called by Kagan and Klinger *fluctuational preparation of the barrier* (FPB), will always tend to increase the tunnelling rate. Thermal motion of the atoms that define the potential barrier between two sites will sometimes raise and other times lower the height of the barrier. The total tunnelling rate will be determined largely by the rate during the time when the atoms take on configurations most conducive to the transition; the path of least resistance contributes the most. Both of these effects depend on the thermal fluctuations of atomic positions, and so are expected to have a larger influence as temperature rises. Barrier fluctuations will have their greatest effect at high temperatures since long-wavelength phonons simply shift whole regions of the lattice without changing the *relative* positions of atoms close to the interstitial. Short wavelength phonons will produce shifts in the separation of adjacent atoms, the ones that define the shape of the barrier, and are excited at temperatures approaching the Debye temperature. The transition rate including the effects of both polaron deformation and barrier fluctuations is

$$W_{12} = 2\pi\Delta_0^2 \sum_{nm} \left| \langle \Psi_n(\mathbf{R}_2) \Lambda^\dagger(R_2) e^{\hat{B}} \Lambda(R_1) \Psi_n(\mathbf{R}_1) \rangle \right|^2 \delta(\xi + E_n - E_m) \quad (5.22)$$

where  $\xi$  is any small energy shift that may exist between initial and final sites, which must be taken up by differences in phonon energies, and the coupling to barrier fluctuations is characterized by the operator

$$\hat{B} = \sum_{\beta} \frac{B_{\beta} b_{\beta}^{\dagger} + B_{\beta}^{*} b_{\beta}}{\tilde{\omega}_0}, \quad (5.23)$$

where  $\tilde{\omega}_0$  is the frequency of the interstitial in its harmonic potential well, included as a normalization factor to make  $\hat{B}$  dimensionless.

Expanding the square of the matrix element in Eq. (5.22) and writing the  $\delta$ -function

in terms of its Fourier transform, we can write the hop rate as an integral over time

$$W_{12} = \Delta_0^2 \int_{-\infty}^{\infty} \langle \Lambda^\dagger(R_1) e^{B^\dagger} \Lambda(R_2) \Lambda^\dagger(R_2, t) e^{B(t)} \Lambda(R_1, t) \rangle e^{i\xi t} dt \quad (5.24)$$

$$= \Delta_0^2 \int_{-\infty}^{\infty} e^{-F_1(t) + i\xi t} dt \quad (5.25)$$

The rest of the problem is in the calculation of  $F_1(t)$ , which contains all the physics.

Expanding each part in terms of the creation and annihilation operators  $b_\beta^\dagger, b_\beta$ . (for which we have the commutator  $[b_\beta^\dagger, b_\beta] = 1$  since phonons are bosons)

$$\langle \Lambda(R_2) e^{\hat{B}} \Lambda(R_1) \rangle = \langle \exp\{(C_\beta(R_2) b_\beta^\dagger - C_\beta^*(R_2) b_\beta)/\omega_\beta\} \times \quad (5.26)$$

$$\exp\{(B_\beta(R_1, R_2) b_\beta^\dagger + B_\beta^*(R_1, R_2) b_\beta)/\tilde{\omega}_0\} \times$$

$$\exp\{(C_\beta^*(R_1) b_\beta - C_\beta(R_1) b_\beta^\dagger)/\omega_\beta\} \rangle$$

$$= e^{B_0} \prod_\beta \left\langle \exp \left\{ \left( \frac{C_\beta}{\omega_\beta} + \frac{B_\beta}{\tilde{\omega}_0} \right) b_\beta^\dagger - \left( \frac{C_\beta}{\omega_\beta} - \frac{B_\beta}{\tilde{\omega}_0} \right) b_\beta \right\} \right\rangle \quad (5.27)$$

where the factor  $e^{B_0}$  is a scalar resulting from the commutators which arise in the product of these operators, in which

$$B_0 = \sum_\beta -\frac{B_{-\beta}[C_\beta(R_1) + C_\beta(R_2)]}{\omega_\beta \tilde{\omega}_0}. \quad (5.28)$$

Doing the same calculation with the second set of time-dependent operators. [with  $b_\beta(t) \rightarrow b_\beta e^{-i\omega_\beta t}$ ] and then calculating the expectation value of the product of all six operators gives the result

$$e^{-F_1(t)} = \exp \left\{ 2B_0 - \sum_\beta \left[ \left( \frac{C_\beta}{\omega_\beta} + \frac{B_\beta}{\tilde{\omega}_0} \right) \left( \frac{C_\beta}{\omega_\beta} - \frac{B_\beta}{\tilde{\omega}_0} \right)^* (2N_\beta + 1) \right. \right. \\ \left. \left. - \left| \frac{C_\beta}{\omega_\beta} + \frac{B_\beta}{\tilde{\omega}_0} \right|^2 (N_\beta + 1) e^{-i\omega_\beta t} - \left| \frac{C_\beta}{\omega_\beta} - \frac{B_\beta}{\tilde{\omega}_0} \right|^2 N_\beta e^{i\omega_\beta t} \right] \right\} \quad (5.29)$$

which now becomes a function of temperature through the temperature dependence of the phonon population.

$$e^{-F_1(t)} = \exp \left\{ 2B_0 + 4G(T) - \sum_\beta \left[ \left| \frac{C_\beta}{\omega_\beta} \right|^2 + \left| \frac{B_\beta}{\tilde{\omega}_0} \right|^2 \right] \{ \coth(\omega_\beta/2T) [1 - \cos(\omega_\beta t)] + i \sin(\omega_\beta t) \} \right\}$$

$$- \sum_{\beta} \frac{C_{\beta} B_{\beta}^* + C_{\beta}^* B_{\beta}}{\omega_{\beta} \tilde{\omega}_0} \left[ \cos(\omega_{\beta} t) - i \sin(\omega_{\beta} t) \coth(\omega_{\beta}/2T) \right] \Bigg\} \quad (5.30)$$

with

$$G(T) = \frac{1}{2} \sum_{\beta} \frac{|B_{\beta}|^2}{\tilde{\omega}_0^2} \coth(\omega_{\beta}/2T). \quad (5.31)$$

Introducing two more sums over the phonon spectrum

$$\Omega_{1\text{ph}}(\omega) = \pi T \sum_{\beta} \frac{1}{\omega_{\beta}} \left[ |C_{\beta}|^2 + \frac{\omega_{\beta}^2}{\tilde{\omega}_0^2} |B_{\beta}|^2 \right] \delta(\omega_{\beta} - \omega) \quad (5.32)$$

$$h(\omega) = \sum_{\beta} \frac{C_{\beta} B_{\beta}^* + C_{\beta}^* B_{\beta}}{\omega_{\beta}} \delta(\omega_{\beta} - \omega) \quad (5.33)$$

results, with more algebra, in the general expression

$$\begin{aligned} F_1(t) &= -2B_0 - 4G(T) + \int \frac{d\omega}{\omega} \frac{\Omega_{1\text{ph}}(\omega)}{\pi T \sinh(\omega/2T)} [\cosh(\omega/2T) - \cosh(i\omega t - \omega/2T)] \\ &\quad + \int \frac{d\omega}{\omega} \frac{h(\omega)}{\sinh(\omega/2T)} [\sinh(i\omega t - \omega/2T)] \end{aligned} \quad (5.34)$$

By shifting the contour on the complex plane, this is

$$\begin{aligned} F_1(t) &= -2B_0 - 4G(T) + \int \frac{d\omega}{\omega} \frac{\Omega_{1\text{ph}}(\omega)}{\pi T \sinh(\omega/2T)} [\cosh(\omega/2T) - \cos(\omega t)] \\ &\quad + \int \frac{d\omega}{\omega} \frac{ih(\omega)}{\sinh(\omega/2T)} \sin(\omega t) \end{aligned} \quad (5.35)$$

Due to the presence of the oscillating terms,  $e^{-F_1(t)}$  is peaked about  $t = 0$ , and so makes the largest contribution to the integral in Eq. (5.25) near  $t, \omega = 0$ . For small  $\omega t$  and  $\omega/2T$  several approximations can be made to further simplify these expressions, leading to an expression that yields its (approximate) temperature dependence in a more intuitive way.

$$\cosh(\omega/2T) - \cos(\omega t) \approx \omega^2 \left[ \frac{1}{8T^2} + \frac{t}{2} \right] \quad \frac{\sin(\omega t)}{\sinh(\omega/2T)} \approx \frac{\omega t}{\omega/2T} \quad (5.36)$$

and

$$\coth(\omega/2T) \approx \frac{2T}{\omega} \left[ 1 + \frac{\omega^2}{12T^2} \right].$$

Using these approximations and defining the following functions enables us to write an expression for the hop rate in which all the sums over the phonon population have been integrated out.

$$\begin{aligned} 1/E_b &= 4 \sum_{\beta} \frac{|B_{\beta}|^2}{\tilde{\omega}_0^2 \omega_{\beta}} & E &= 1/4 \sum_{\beta} \frac{|C_{\beta}|^2}{\omega_{\beta}} \\ \gamma &= 1/4 \sum_{\beta} \omega_{\beta} \frac{|B_{\beta}|^2}{\tilde{\omega}_0^2} & \zeta &= 4 \sum_{\beta} \frac{C_{\beta} B_{\beta}}{\tilde{\omega}_0 \omega_{\beta}} \end{aligned} \quad (5.37)$$

In terms of these functions we obtain

$$W_{12} = (\Delta_0 e^{B_0})^2 e^{-E/T + T/E_b} \int_{-\infty}^{\infty} dt \exp\{4(E + \gamma)Tt^2 - i\zeta Tt\} \quad (5.38)$$

This integral can be solved exactly, giving a simple expression for the hop rate

$$W_{12} = \frac{\sqrt{\pi}}{2} \frac{(\Delta_0 e^{B_0})^2}{\sqrt{(E + \gamma)T}} \exp\left\{-\frac{E}{T} + \frac{T}{E_b} - \frac{\zeta^2 T}{16(E + \gamma)}\right\} \quad (5.39)$$

If the coupling to barrier fluctuations turns out to be negligible (that is, letting all the  $B_{\beta}$ 's go to zero) then we recover the familiar expression

$$W_{12} = \frac{\sqrt{\pi} \Delta_0^2}{2\sqrt{ET}} e^{-E/T} \quad (5.40)$$

giving the hop rate of the particle and associated polaron in the absence of any effect of barrier height fluctuations, which was originally obtained by Flynn and Stoneham. Here,  $E$  is just the barrier height which would exist between two adjacent polaron-deformed sites.

The motivation for making all of these approximations was to allow one to write a simple expression for the hop rate. It turns out that the existence of an upper cut-off



frequency (essentially the Debye frequency  $\omega_D$ ) in the sums over the phonon modes makes it possible to calculate the integrals in the general form, Eq. (5.35), by numerical methods without making any further approximations. This approach is taken in the analysis of Mu diffusion in solid Xe.

### 5.5 Quadratic Coupling: Two-Phonon Limited Diffusion

The second case we consider has the coupling to lattice excitations taking a form quadratic in atomic displacements so we now write the Hamiltonian, in terms of the same shifted-mode phonon operators as before, as

$$\mathcal{H} = \sum_{\beta} \omega_{\beta} (b_{\beta}^{\dagger} b_{\beta} + 1/2) + \sum_{\beta\beta'} C_{\beta\beta'} (b_{\beta} + b_{-\beta}^{\dagger})(b_{\beta'} + b_{-\beta'}^{\dagger}). \quad (5.41)$$

We continue in the same framework we used in solving the one-phonon problem. Again, we are interested in finding out how much the initial and final states overlap, so we want to construct these states in terms of unitary transformations of the environmental states. Now the full polaron operator in Eq. (5.24) becomes, with an additional unitary operator for the two-phonon interaction,  $\Lambda = \Lambda_1 \Lambda_2$ . Again, we write the transition rate, making use of the Fourier transform of the  $\delta$ -function,

$$W_{12} = \Delta_0^2 \int_{-\infty}^{\infty} dt \langle e^{-B(t)} \Lambda(t)^{\dagger} \Lambda(0) e^B \rangle \delta(\xi + E_2 - E_1). \quad (5.42)$$

Here  $\Lambda_2$  is composed of two parts that arise from the cross terms in the product  $(b_{\beta} + b_{-\beta}^{\dagger})(b_{\beta'} + b_{-\beta'}^{\dagger})$ .

$$\begin{aligned} \Lambda_2 = & \exp \left\{ - \sum_{\beta\beta'} \left[ \frac{C_{\beta\beta'} b_{\beta}^{\dagger} b_{\beta'}}{\omega_{\beta} - \omega_{\beta'}} - \frac{C_{\beta\beta'}^* b_{\beta} b_{\beta'}^{\dagger}}{\omega_{\beta} - \omega_{\beta'}} \right] \right\} \\ & \times \exp \left\{ - \sum_{\beta\beta'} \left[ \frac{C_{\beta\beta'} b_{\beta}^{\dagger} b_{\beta'}^{\dagger}}{\omega_{\beta} + \omega_{\beta'}} - \frac{C_{\beta\beta'}^* b_{\beta} b_{\beta'}}{\omega_{\beta} + \omega_{\beta'}} \right] \right\} \end{aligned} \quad (5.43)$$

There are two kinds (not counting complex conjugates) of two-phonon terms in this: those of the form  $b_{\beta} b_{\beta'}$ , that create (or annihilate) two separate phonons, and those of the

form  $b_\beta^\dagger b_{\beta'}$  that annihilate one phonon and create another, therefore allowing *scattering* of one phonon from one state to another. The largest contribution to the transition rate comes from those terms where the shift of the phonon frequency due to scattering is small;  $\omega_\beta \approx \omega_{\beta'}$ . For this reason the scattering part of the two-phonon interaction is said to preserve the phonon population, but strictly speaking it is not *precisely* unchanged. We are in a regime where coherent (band) diffusion is partially ruined by the scattering of phonons. Further, in the limit of a small shift in phonon frequencies so that  $\omega_\beta \approx \omega_{\beta'}$ , we have approximately

$$N_\beta(N_{\beta'} + 1) \approx \frac{e^{\omega_\beta/T}}{(e^{\omega_\beta/T} - 1)^2}$$

and we shall see the usual phonon density of states enters as  $g^2(\omega)$ , *not* as a density of two-phonon states. Keeping only the scattering terms from Eq. (5.43)

$$\Lambda_2 \approx \exp \left\{ \sum_{\beta\beta'} \frac{C_{\beta\beta'} b_\beta^\dagger b_{\beta'} - C_{\beta\beta'}^* b_\beta b_{\beta'}^\dagger}{\omega_\beta - \omega_{\beta'}} \right\}. \quad (5.44)$$

We write out the matrix element by the same method as we used for the one-phonon interaction and consider now each mode as separable,

$$\begin{aligned} \langle e^{-B(t)} \Lambda(t) \Lambda^\dagger(0) e^{-B(0)} \rangle &= \langle e^{-B(t)} \Lambda_1(t) \Lambda_2(t) \Lambda_2^\dagger(0) \Lambda_1^\dagger(0) e^{-B(0)} \rangle \\ &= \langle e^{-B(t)} \Lambda_1(t) \Lambda_1^\dagger(0) e^{-B(0)} \rangle \langle \Lambda_2(t) \Lambda_2^\dagger(0) \rangle. \end{aligned} \quad (5.45)$$

We see that renormalization of the tunnelling bandwidth  $\Delta_0$  by the 1-phonon interaction still holds, but now we are also including what will turn out to be a reduction of the effective bandwidth due to the contribution of the two-phonon interaction, corresponding to the terms of the form  $b_\beta^\dagger b_{\beta'}$  in  $\langle \Lambda_2^\dagger \Lambda_2 \rangle$ .

By the same method as we used earlier, we write out the expectation value in terms of the boson operators

$$\langle \Lambda_2(R_2, t)^\dagger \Lambda_2(R_1, 0) \rangle = \left\langle -\frac{1}{2} \sum_{\beta\beta'} \left[ \frac{|C_{\beta\beta'}(R_2)|^2 b_\beta^\dagger b_{\beta'} b_\beta b_{\beta'}^\dagger}{(\omega_\beta - \omega_{\beta'})^2} + \frac{|C_{\beta\beta'}(R_1)|^2 b_\beta^\dagger b_{\beta'} b_\beta b_{\beta'}^\dagger}{(\omega_\beta - \omega_{\beta'})^2} \right] \right\rangle$$

$$- \left. \frac{C_{\beta\beta'}(R_2)C_{\beta\beta'}^*(R_1) + C_{\beta\beta'}^*(R_2)C_{\beta\beta'}(R_1)}{(\omega_\beta - \omega_{\beta'})^2} b_{\beta'}^\dagger b_{\beta'} b_\beta b_{\beta'}^\dagger \right] \rangle \quad (5.46)$$

$$= - \sum_{\beta\beta'} \frac{|C_{\beta\beta'}(R_1) - C_{\beta\beta'}(R_2)|^2}{(\omega_\beta - \omega_{\beta'})^2} N_\beta (N_{\beta'} + 1) \quad (5.47)$$

For small frequency shifts  $\omega_\beta - \omega_{\beta'}$  this is, to very good approximation.

$$\langle \Lambda_2^\dagger \Lambda_2 \rangle = \exp \left\{ - \int_0^{\omega_{\max}} \frac{d\omega}{\omega} \frac{\Omega_2(T, \omega)}{2\pi T} \coth(\omega/2T) \right\} \quad (5.48)$$

with

$$\Omega_2(T, \omega) = \pi T \sum_{\beta\beta'} \frac{|C_{\beta\beta'}(R_2) - C_{\beta\beta'}(R_1)|^2}{\omega_\beta - \omega_{\beta'}} (N_\beta - N_{\beta'}) \delta(\omega_\beta - \omega_{\beta'} - \omega) \quad (5.49)$$

We have put  $\Omega_2(T)$  in this form so we can write

$$\int_0^{\omega_{\max}} \frac{d\omega}{\omega} \frac{\Omega_2(T)}{\pi T} \frac{\cosh(\omega/2T) - 1}{\sinh(\omega/2T)} + \int_0^{\omega_{\max}} \frac{d\omega}{\omega} \frac{\Omega_2(T)}{\pi T} \frac{1 - \cos(\omega t)}{\sinh(\omega/2T)} = -\Omega_2(T)|t| \quad (5.50)$$

in which we have dropped the time-independent term, since it is small for temperatures low compared to typical  $\omega$ , and the frequency dependence of  $\Omega_2$  since we are in the limit of small differences between phonon frequencies.

The hop rate is then

$$W_{12} = \Delta_0^2 e^{\xi/2T} \int_{-\infty}^{\infty} e^{i\xi t - \Omega_2 |t|} dt. \quad (5.51)$$

What is the function  $\Omega_2(T)$ ? Here it is clear that  $\Omega_2$  (which is always a positive, real quantity) takes on the role of an exponential relaxation (or damping) rate of the transition amplitude. The initial and final states during the tunnelling transition have almost exactly the same energy, but *phase* coherence is lost in the process of scattering phonons. Coherence is suppressed when the transition time  $\tau$  is relatively long so that  $\Omega_2 \tau > 1$ . The integral in Eq. (5.51) converges to

$$W_{12} = \frac{2\Delta_0^2 \Omega_2(T)}{\xi^2 + \Omega_2^2(T)}. \quad (5.52)$$

The temperature dependence of the hop rate is then determined by the de-coherence rate  $\Omega_2(T)$  and the interplay with the typical site-to-site energy shift  $\xi$ . In the following section we will show that  $\Omega_2(T)$  is a strongly increasing function of temperature and also explore the influence of the phonon density of states on the diffusion rate.

## Chapter 6

### Quantum Diffusion II: Experimental Results

#### 6.1 Two-Phonon Quantum Diffusion

At temperatures well below the Debye temperature of the host solid, the tunnelling diffusion rate will be determined by the full coherent transition amplitude as long as the rate of loss of phase coherence,  $\Omega_2(T)$ , is small compared to the inverse of the under-barrier transition time. Without scattering, the mean free path can exceed the lattice constant so the particle propagates in a band-like state. As the temperature is increased, two things happen: the enhanced phonon population causes a very rapid increase in  $\Omega_2(T)$ , suppressing the coherent channel; meanwhile the hop rate due to the one-phonon, thermally-activated tunnelling mechanism increases exponentially. The contribution of one-phonon hopping becomes dominant when  $\Omega_2$  exceeds  $\tilde{\Delta}_0$ , providing a natural division of the temperature scale. For the purpose of discussing quantum diffusion, “low” temperature means temperatures where the 2-phonon incoherent channel, though partly diminished by phonon scattering, still exceeds the contribution of thermally-activated hopping mediated by the one-phonon interaction. In this section we will consider in more detail the predictions of theory in the incoherent regime and compare these with experimental results.

Previously we showed that the incoherent diffusion rate in the presence of an interstitial-lattice coupling quadratic in lattice displacements (*i.e.* two-phonon coupling) is

$$1/\tau_c = 2 \frac{\tilde{\Delta}_0^2 \Omega_2}{\xi^2 + \Omega_2^2} \quad (6.1)$$

where the tunnelling bandwidth renormalized by the one-phonon interaction is

$$\tilde{\Delta}_0 = \Delta_0 \exp[B_0 - \phi(T) + G(T)] \quad (6.2)$$

with  $\Delta_0$  the bandwidth in a perfect lattice and  $\xi$  the typical site-to-site static level shift. The temperature dependent parameters in the exponent characterize the polaron effect and barrier fluctuations and are respectively

$$\phi(T) = \sum_{\beta} \frac{|C_{\beta}(R_1) - C_{\beta}(R_2)|^2}{2\omega_{\beta}^2} \coth(\omega_{\beta}/2T) \quad (6.3)$$

and

$$G(T) = 1/2 \sum_{\beta} |B_{\beta}|^2 \coth(\omega_{\beta}/2T). \quad (6.4)$$

The de-coherence rate  $\Omega_2(T)$  was defined in terms of the two-phonon coupling parameters  $C_{\beta\beta'}(R_1, R_2) = C_{\beta\beta'}(R_1) - C_{\beta\beta'}(R_2)$  and phonon numbers  $N_{\beta}$  by

$$\Omega_2(\omega, T) = \pi T \sum_{\beta\beta'} \frac{|C_{\beta\beta'}(R_1, R_2)|^2}{\omega_{\beta} - \omega_{\beta'}} (N_{\beta'} - N_{\beta}) \delta(\omega_{\beta} - \omega_{\beta'} - \omega). \quad (6.5)$$

Recalling that the largest contribution from phonon scattering comes from those terms where  $(\omega_{\beta} - \omega_{\beta'}) \rightarrow 0$ , we can write the difference  $N_{\beta'} - N_{\beta}$  in this limit as

$$\begin{aligned} N_{\beta'} - N_{\beta} &= \frac{dN}{d\omega}(\omega_{\beta'} - \omega_{\beta}) \\ &= -\frac{e^{\omega_{\beta}/T}}{T(e^{\omega_{\beta}/T} - 1)^2}(\omega_{\beta'} - \omega_{\beta}) \end{aligned} \quad (6.6)$$

In this limit  $\Omega_2(\omega, T)$  becomes frequency-independent and is given by

$$\lim_{\omega \rightarrow 0} \Omega_2(T) = \pi \sum_{\beta\beta'} |C_{\beta\beta'}(R_1, R_2)|^2 N_{\beta}(N_{\beta'} + 1) \delta(\omega_{\beta} - \omega_{\beta'}). \quad (6.7)$$

Frequency independence of the damping rate  $\Omega_2(T)$  implies that two-phonon scattering is an example of an Ohmic coupling to the medium in the Caldeira-Leggett theory of dissipation. [38, 39] In order to obtain the hop rate as an explicit function of temperature

we approximate the summation over phonons by an integral over the phonon density of states  $g(\omega)$

$$\Omega_2(T) = \int_0^{\omega_D} d\omega \lambda(\omega) g^2(\omega) \frac{e^{\omega/T}}{(e^{\omega/T} - 1)^2} \quad (6.8)$$

where  $\lambda(\omega) = |C_{\beta\beta}|^2$  is the matrix element in Eq. (6.5) averaged over the branches of the phonon modes.

At this stage it is possible to determine the temperature dependence of the hop rate at least qualitatively for temperatures  $T \ll \Theta_D$ . Solids generally have phonon spectra that at long wavelengths - the only modes excited at low  $T$  - closely follow the Debye model with  $g(\omega) \propto \omega^2$  and the coupling constant  $|C_\beta|^2 \propto \omega_\beta^2$ . In the low temperature limit Eq. (6.8) then gives us  $\Omega_2(T) \propto T^7$ .

We are now in a position to consider the qualitative temperature dependence of the interstitial diffusion rate. In the case that  $\Omega_2 > \xi$ , Eq. (6.1) reduces approximately to

$$1/\tau_c = \frac{2\tilde{\Delta}_0^2}{\Omega_2(T)} \quad (6.9)$$

and where  $\Omega_2(T) < \xi$  to

$$1/\tau_c = \frac{2\tilde{\Delta}_0^2 \Omega_2(T)}{\xi^2}. \quad (6.10)$$

Since  $\Omega_2(T)$  always increases monotonically with temperature we have two possible situations. We expect that at sufficiently low temperatures (but still large compared to the bandwidth) there is the possibility that Eq. (6.10) applies and in the low temperature limit  $T \ll \Theta_D$  we have  $1/\tau_c \propto T^7$ . In this case the scattering of phonons actually helps the diffusing particle to overcome the static level shifts  $\xi$ . The other possibility (generally at some higher temperature) is that the static shifts are comparatively small in which case Eq. (6.9) applies and  $1/\tau_c \propto T^{-7}$ ; phonon scattering then hinders the band-like diffusion in the periodic potential of the lattice.

## 6.2 Muonium Diffusion in KCl

Although nominally outside the terms of reference of this thesis, the following example serves to illustrate the application of the preceding theory, to clear up an historical misunderstanding and to provide continuity with recent studies of muonium diffusion.

Experiments performed by Kiefl *et.al.* [66] and MacFarlane *et.al.* [67] measured the muonium hop rate in KCl over a wide temperature range, clearly showing the position of the minimum hop rate, characteristic of the crossover from two-phonon limited diffusion to one-phonon activated diffusion, at  $T_{\min} \approx 70$  K. The measured hop rate below  $T_{\min}$  was fitted to a power law relation  $D(T) \propto T^{-\alpha}$ , yielding a value  $\alpha = 3.3(1)$ . It was noted at the time that the low temperature limiting value of  $\alpha$  predicted by theory was 7 (or 9 in a perfect fcc lattice if the sites are symmetric with respect to the phonon modes); the discrepancy with the measured result remained unexplained.

To answer the question of why the hop rate in KCl did not follow a  $T^{-7}$  dependence, Kagan and Prokof'ev argued in their 1990 paper [54] that if one used the real phonon spectrum in Eq. (6.8) one could obtain agreement with the measured  $T$ -dependence. They wrote also in their review article [53] that the “experimentally found temperature dependence in this region is considerably weaker than that predicted by the limiting law [ $T^{-7}$ ]. That is, however, associated not with the loss of the dominant role by two-phonon processes but with the real structure of the phonon spectrum of these crystals.” Their calculation of  $\alpha$  with the real phonon spectrum in Eq. (6.8) obtained the result  $\alpha = 3.5$ . We will show here that their interpretation of the role of structure in the phonon spectrum is not correct. The relative weakness of the temperature dependence (*i.e.* reduction of  $\alpha$  from 7) is a result predicted by this theory, which *would* be present even if the actual phonon spectrum were entirely Debye-like. The *structure* present in the phonon density



of states of KCl is *not* responsible for this. Here we will repeat the calculation performed by Kagan and Prokof'ev, and also the case where the phonon spectrum is a featureless, smooth Debye-like function.

The total phonon density of states of KCl, measured by inelastic neutron scattering [55], is shown in Fig. 6.15. The damping rate  $\Omega_2(T)$  can then be calculated using this spectrum for  $g(\omega)$  in a numerical integration over phonon frequency  $\omega$ . (The Debye temperature of KCl is about 230 K, but the real phonon density of states has its upper cut-off at  $\hbar\omega_{\max}/k_B \approx 305$  K.) In this calculation,  $g(\omega)$  is normalized so that its integral is unity, which does not affect its  $T$ -dependence, only an overall factor. The correct normalization of the phonon density of states can be obtained by calculating the lattice specific heat

$$c(T) = \frac{1}{V} \frac{d}{dT} \int \frac{\omega g(\omega)}{e^{\omega/T} - 1} d\omega \quad (6.11)$$

Figure 6.16 shows the temperature dependence of  $\Omega_2(T)$ , along with the result obtained if it is assumed that  $g(\omega) \propto \omega^2$ . Figure 6.17 shows the temperature dependence of the power law exponent

$$\alpha(T) = \frac{T}{\Omega_2(T)} \frac{d\Omega_2(T)}{dT}$$

for the same cases.

The principal cause of the weak temperature dependence of the muonium hop rate in KCl is that the temperature where the hop rate minimum occurs is already a sufficiently large fraction of  $\Theta_D$  that the entire phonon spectrum contributes to  $\Omega_2$ . The population of low frequency phonons for which  $\omega/T \ll 1$  increases only linearly with  $T$ ; the temperature dependence of  $\Omega_2$  drops off. Since the temperature at which the minimum hop rate occurs is 70 K, a substantial fraction of the Debye temperature, we are far from the low temperature limit where one obtains  $\alpha = 7$ . It can be seen from the graph that this is the case whether the real spectrum or a Debye-like  $g(\omega)$  is used. It is an intrinsic property

of two-phonon diffusion, *not* the structure in the spectrum, that causes  $\Omega_2(T)$  to be characterized by a lower  $\alpha$  at temperatures greater than about  $\Theta_D/10$  or so. The structure in the real  $g(\omega)$  has a small effect on  $\Omega_2(T)$ , as can be seen, but the overall shape of the function is hardly affected. A weak temperature dependence of the 2-phonon diffusion rate will occur in any crystal for which  $T_{\min}$  (the temperature where the crossover between two-phonon and one-phonon regimes occurs) happens to be more than about  $\Theta_D/10$ , so that two-phonon diffusion is important at relatively high temperatures. Related to this, it must be stressed that the  $T^{\pm 7}$  dependence is expected *only* in the low temperature limit  $T \ll \Theta_D$ . It is a simple exercise to show that in the high temperature limit (several times  $\Theta_D$ ),  $\Omega_2(T) \propto T^2$ . At all intermediate temperatures, the characteristic exponent  $\alpha$  is a function of temperature, and it is not very meaningful to apply a single value to  $\alpha$  over a range of temperatures. It is also possible that the coupling to high-frequency modes doesn't follow the simple low frequency limiting behavior. If this is the case, the model will fail completely at higher temperatures.

### 6.3 Experimental Results in Solid Nitrogen

In solid nitrogen muonium diffusion was studied using both longitudinal and transverse field muon spin rotation/relaxation techniques. From the relaxation rates of the muon polarization one can extract the muonium hop rate as a function of temperature. This is compared to the behavior predicted by theory, finding agreement at low temperatures only.

With a weak longitudinal magnetic field of a few Gauss applied to the sample, the muon and electron spins in muonium are strongly coupled by the hyperfine interaction. As the muonium atom diffuses among atoms of the host lattice, the nuclear hyperfine (nhf) interaction between the spins of the muonium electron and the randomly-oriented

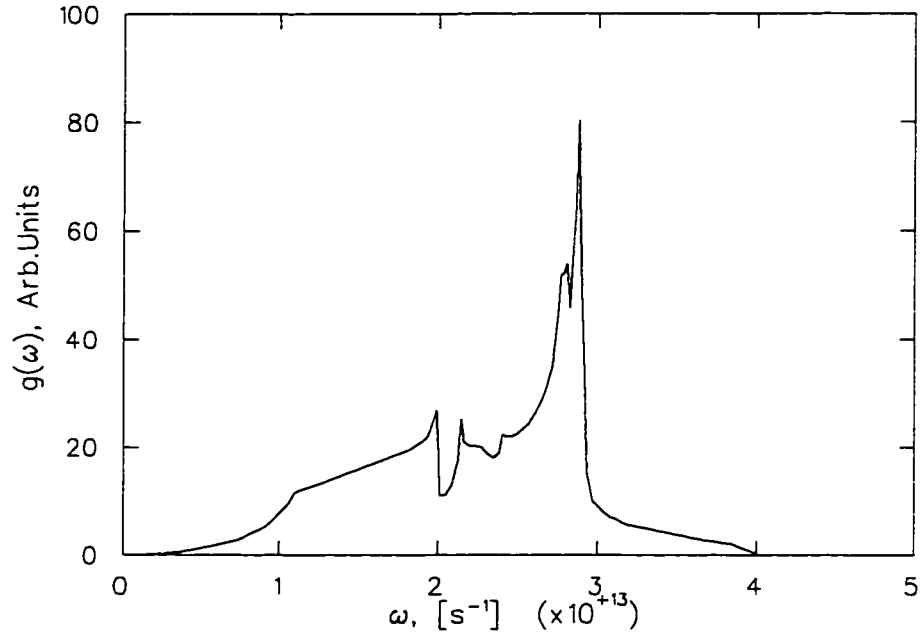


Figure 6.15: Phonon density of states  $g(\omega)$  of KCl, from MacPherson and Timusk. *Can. J. Phys.* **48**, 2917 (1970)

lattice nuclear moments undergoes fluctuations. The resulting time-dependent effective magnetic field felt by the muonium atom excites transitions among states of the muonium atom, and the original polarization of the muon spin is lost. Figure 6.18 shows the temperature and magnetic field dependence of the muon asymmetry measured in  $s\text{-N}_2$  in longitudinal field. To a good approximation, in weak magnetic fields the muon spin polarization relaxes with an exponential time dependence

$$P_z(t) = P_z(0)e^{-t/T_1} \quad (6.12)$$

where the relaxation rate  $1/T_1$  depends on the hop rate  $1/\tau_c$  according to

$$1/T_1 \approx \frac{\delta_{\text{nhf}}^2 \tau_c}{1 + \omega_{12}^2 \tau_c^2}. \quad (6.13)$$

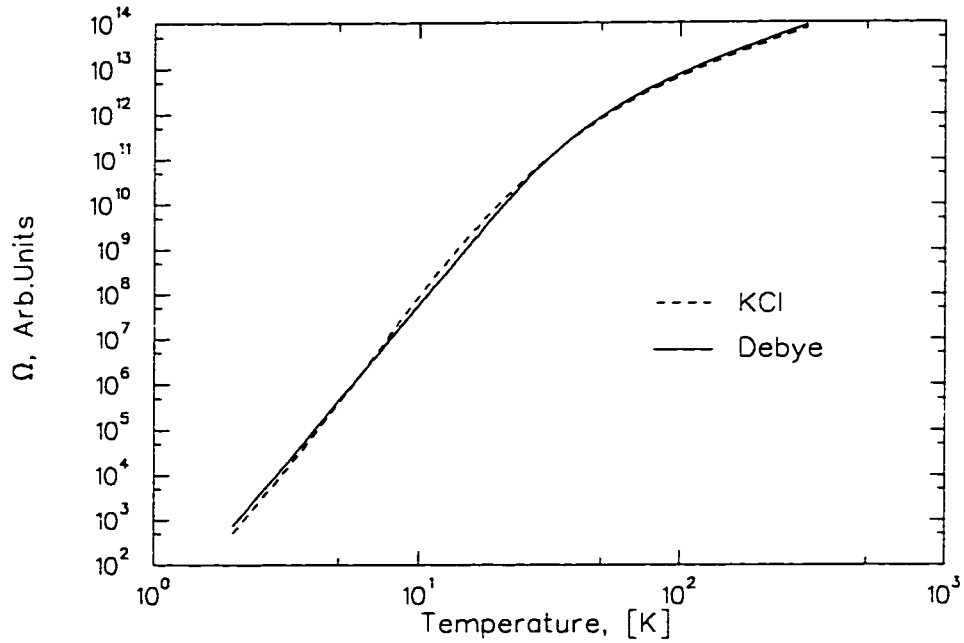


Figure 6.16: Dashed line:  $\Omega_2(T)$  calculated in the case where  $g(\omega)$  is the real phonon density of states of KCl. Solid line: the same calculation performed assuming a Debye model.

Equation (6.13) also predicts the presence of a  $1/T_1$  maximum where  $\tau_c = 1/\omega_{12}$ . Such maxima are evident in the relaxation rates, which peak at different temperatures depending on the field, allowing one to make an unambiguous determination of the diffusion rate independent of the absolute scale of the relaxation rate.

Figure 6.19 shows examples of muonium spin precession signals measured in a weak transverse field (wTF) of 5 G. In weak magnetic fields the two observable muonium frequencies  $\omega_{12}$  and  $\omega_{23}$  are very nearly equal (see Appendix A for definitions of these and the other muonium frequencies  $\omega_{\pm}$  and  $\omega_0$ ) the splitting between these two lines is

$$\omega_{23} - \omega_{12} = \sqrt{\omega_0^2 + 4\omega_{\mp}^2} - \omega_0, \quad (6.14)$$

and in fields  $B \ll B_0$  this is approximately  $2\omega_{\mp}^2/\omega_0$ . In a transverse magnetic field of

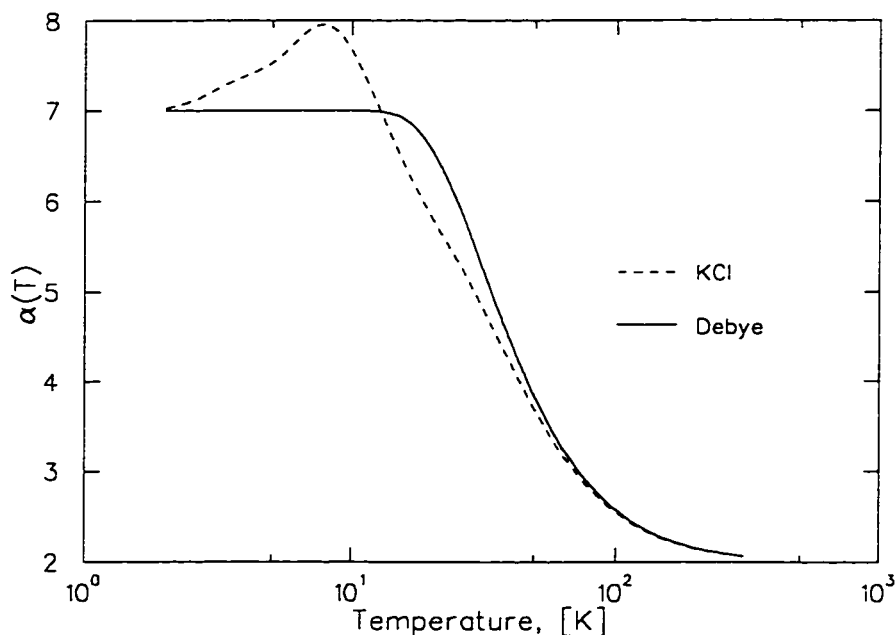


Figure 6.17: Temperature dependence of the exponent  $\alpha = \frac{T}{\Omega_2} \frac{d\Omega_2}{dT}$  calculated for KCl with the real phonon spectrum (dashed line) and Debye-like phonon density of states (solid line).

8 G or less, and when the muonium relaxation rate is greater than about  $0.25 \mu\text{s}^{-1}$ . “beating” of the two triplet muonium frequencies is not apparent within the  $10 \mu\text{s}$  time range of the histogram; the muonium spin precesses with one signal at the mean frequency  $\omega_{\text{Mu}} = (\omega_{12} + \omega_{23})/2 = 1.3961 \text{ MHz/G} \times B$ . (However, in slightly larger magnetic fields, or if the spin relaxation rate is extremely low, the beat envelope will masquerade as a Gaussian relaxation function which, if one mistakenly fitted the asymmetry with a single signal, would result in a misleading contribution to the real relaxation rate.) The asymmetry measured in  $s\text{-N}_2$  was fitted to a sum of signals for fast and slowly relaxing diamagnetic fractions and the muonium fraction:

$$A(t) = e^{-t/\tau_\mu} \left[ A_D^f \cos(\omega_\mu t + \phi_D) e^{-t/T_2^f} \right]$$

$$\begin{aligned}
& + A_D^s \cos(\omega_\mu t + \phi_D) e^{-t/T_2^s} \\
& + A_{Mu} \cos(\omega_{Mu} t + \phi_{Mu}) e^{-t/T_2^{Mu}} \Big] + b
\end{aligned} \tag{6.15}$$

In transverse field the polarization relaxation function depends on the particle hop rate due to the motional narrowing of the precession frequency linewidth. Assuming that the local (effective nhf) field correlation function is described by

$$\langle B(t)B(0) \rangle = \delta^2 e^{-t/\tau_c} \tag{6.16}$$

(where  $\tau_c$  is the correlation time and  $\delta$  is the width of the field distribution) the relaxation function is [56]

$$G_{xx}(t) = \exp\{-\delta^2 \tau_c^2 (t/\tau_c - 1 + e^{-t/\tau_c})\}. \tag{6.17}$$

In the case of sufficiently slow hopping when  $t/\tau_c \ll 1$ , the TF relaxation function approaches the Gaussian form of the static limit

$$\begin{aligned}
G_{xx}(t) & \approx e^{-\delta^2 t^2/2} \\
& \approx e^{-\frac{1}{2}(t/T_2)^2}
\end{aligned} \tag{6.18}$$

independent of  $\tau_c$ , with relaxation rate  $1/T_2 = \delta$ . In the case of fast hopping the effective nhf field is averaged over many sites resulting in the motional narrowing of the linewidth: the relaxation function tends to an exponential form:

$$\begin{aligned}
G_{xx}(t) & \approx e^{-\delta^2 \tau_c t} \\
& \approx e^{-t/T_2}
\end{aligned} \tag{6.19}$$

with the smaller relaxation rate  $1/T_2 = \delta^2 \tau_c$ . In the limit of fast hopping the TF and LF experiments should give the same relaxation rates. Figure 6.20 shows examples of the relaxation function for several correlation times corresponding to mean hop rates from 0 to  $50 \mu\text{s}^{-1}$ .

Figure 6.21 shows the muonium spin relaxation rates measured in  $s\text{-N}_2$  by TF and LF  $\mu\text{SR}$  experiments. The *qualitative* temperature dependence of the relaxation rates and the hop rate is entirely consistent with the following interpretation. At low temperatures ( $T < 5\text{K}$ ) muonium is nearly static; the TF experiment measured a  $T$ -independent relaxation rate as expected in the slow-hopping limit. Between about 9 K and 20 K the TF relaxation rate drops, as expected if the muonium diffuses faster as temperature rises. The LF relaxation rates in 4, 8 and 12 G reach their maxima, where

$$\omega_{12}(B)\tau_c(T) = 1$$

is satisfied, at progressively higher temperatures. Between about 11 K and 15 K the relaxation rate in LF becomes field-independent and approaches the TF relaxation rate, also indicating that the hop rate increases with temperature in this part of the data.

Making use of Eqs. (6.13),(6.18) and (6.19) we can extract the muonium hop rate  $1/\tau_c$  as a function of temperature, as shown in Fig. 6.22. The LF experiments measured a diffusion rate increasing as  $T^{6.7(1)}$  up to 15 K. The TF data extend this to higher temperatures where the correlation time  $\tau_c$  is so short that the LF relaxation rate becomes nearly independent of magnetic field and approaches the TF relaxation rate. Between about 20 and 30 K the hop rate reaches its maximum; the TF relaxation rate become  $T$ -independent at about  $0.4 \mu\text{s}^{-1}$ . If the hop rate here is limited only by the coherent tunnelling bandwidth, we can estimate

$$\tilde{\Delta}_0 \approx \frac{\hbar}{2\sqrt{2}\tau_c} = 0.003 \text{ K } k_B.$$

It is also possible that the relaxation rate due to the motionally averaged nuclear hyperfine interaction with  $\text{N}_2$  moments is even smaller, but is overwhelmed by spin relaxation due to other causes, such as the muonium atoms diffusing to chemically active impurities or impurities with electronic moments such as  $\text{O}_2$  that immediately depolarize any muonium

atom that strays near. Above about 50 K the TF relaxation rate increases as the hop rate drops with increasing temperature, a key characteristic of incoherent (2-phonon) quantum diffusion, although theory predicts a much weaker temperature dependence at such a large fraction of the Debye temperature.

#### 6.4 Numerical Calculations: Solid Nitrogen

Figure 6.23 shows the phonon density of states  $g(\omega)$  of solid nitrogen at 22 K, measured by Cardini *et al.*[57]. With this spectrum Eq. (6.8) may be evaluated by numerical methods, assuming a particle-phonon coupling  $\lambda(\omega) \propto \omega^2$ , giving  $\Omega_2(T)$  as shown in Fig. 6.24. Since we do not know the coupling constant we cannot attach an absolute scale to  $\Omega_2$ ; only the temperature dependence is obtained. Also shown is the case where the phonon spectrum is taken to be due to a Debye-like density of states  $g(\omega) \propto \omega^2$  over the entire phonon spectrum; the two outcomes are not very different.

At low temperatures ( $T \ll \Theta_D = 83.5$  K), theory predicts that  $\Omega_2(T)$  should be proportional to  $T^7$ . This should hold up to temperatures of about 10 K, where the temperature dependence should drop off gradually to a  $T^2$  dependence for  $T \sim \Theta_D$  and greater. (The high temperature regime is mentioned here only to exemplify the  $T^2$  behavior; *s*-N<sub>2</sub> melts at 63 K).

It is not necessary that  $\xi$  itself be temperature-dependent for there to be a cross-over from the low-temperature, defect-dominated behavior to the higher temperature, homogeneous regime. Since  $\Omega_2(T)$  is always a monotonically increasing function of  $T$ , it may be that  $\xi$  simply becomes negligible and the hopping behavior changes from Eq. (6.10) to Eq. (6.9) at a temperature near 20 K. At sufficiently low temperatures  $\Omega_2$  will inevitably drop below  $\xi$  and the behavior we expect in the limit of  $T \rightarrow 0$ , as long as the damping rate is sufficient that we still have incoherent tunnelling, will always be



a hop rate  $1/\tau_c \propto T^7$ . However, there is reason to believe that  $\xi$  may be temperature dependent in  $s\text{-N}_2$ . It is known that the  $\alpha\text{-N}_2$  lattice undergoes a transition at about 22 K, below which the molecules take on preferred orientations, rotating at a fixed angle about the diagonals of the cubic unit cell. Above this temperature they are free rotators, and the muonium atom should see the same averaged potential well at each site. The orientational disorder introduced by this transition may be responsible for creating level shifts that hinder tunnelling according to Eq. (6.10).

Impurities in the sample evidently do not affect the muonium diffusion rate at low temperatures. Experiments were performed on samples of  $s\text{-N}_2$  with CO concentrations of 0.01% and 0.1%. Carbon monoxide has the same molecular mass as  $\text{N}_2$  and freezes in the lattice as a random substitutional impurity. The results are shown in Fig. 6.25 along with the results from the most carefully annealed sample of solid ultra high purity  $\text{N}_2$ . At temperatures where muonium diffuses rapidly (between 20 and 30 K) the TF relaxation rate  $1/T_2$  increases with CO concentration, up to  $40 \mu\text{s}^{-1}$  with 0.1% CO, well above the rate measured for nearly static muonium in pure  $\text{N}_2$  at low temperatures. This is due to muonium diffusing to the CO where it undergoes a fast chemical reaction to form a diamagnetic species, so the relaxation rate measures the time-of-flight of the muonium to the site of the CO molecule. However, at low temperatures the relaxation rates are independent of impurity concentration. Thus the static shift  $\xi$  that seems to become important at low temperatures is not due to impurities, at least at this level: its origin seems to be intrinsic to  $s\text{-N}_2$ .

The very strong temperature dependence predicted by the two-phonon model is convincingly demonstrated in the case of muonium diffusion in solid  $\alpha\text{-N}_2$  below 15 K. At higher temperatures, particularly 30–50 K, theory predicts a much weaker dependence than was measured, as was the case for KCl, so we cannot claim to fully understand muonium diffusion quantitatively in this temperature range. However, the rapid *increase*

in hop rate as temperature *decreases* is still strong qualitative evidence that the muonium is diffusing by incoherent quantum tunnelling mediated by phonon scattering. It is possible that this quantitative failure of the model results from the breakdown of our (rather simple) assumptions regarding the frequency dependence of the coupling constants.

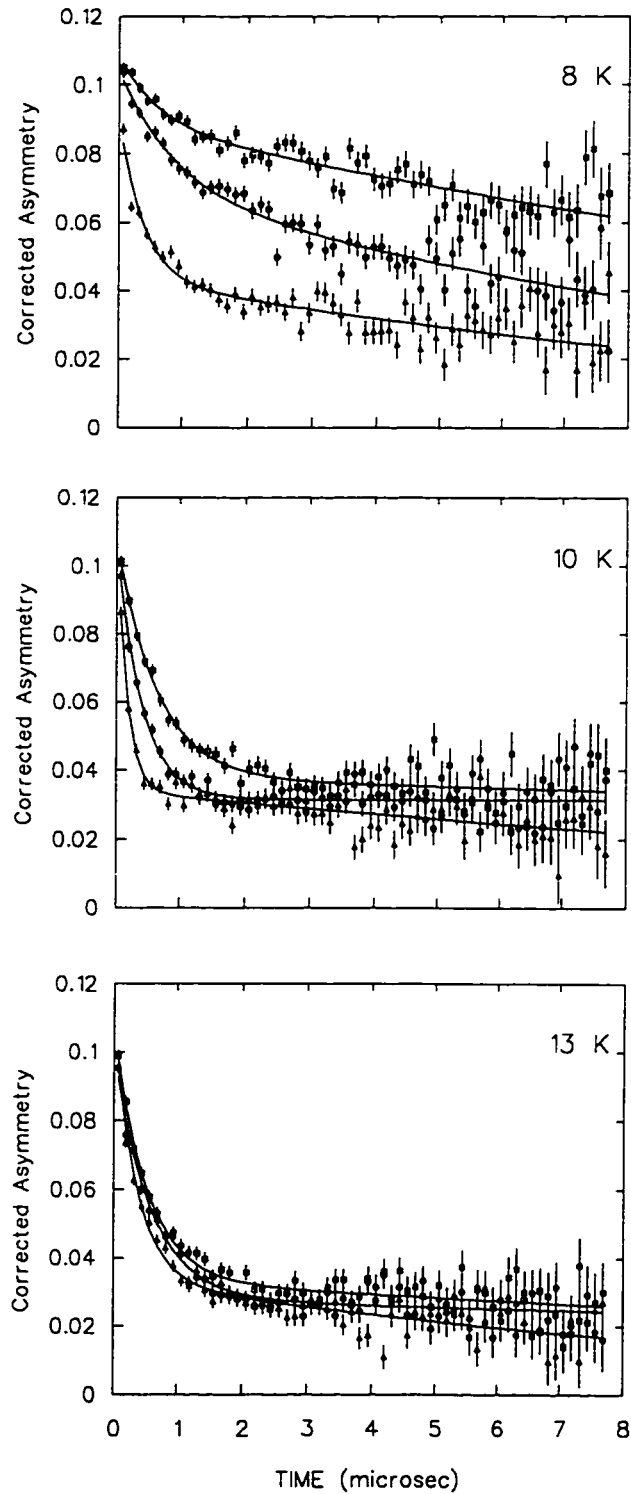


Figure 6.18: Asymmetries measured in solid  $N_2$  at various temperatures in weak longitudinal magnetic fields of (from bottom to top in each plot) 4, 8 and 12 G.

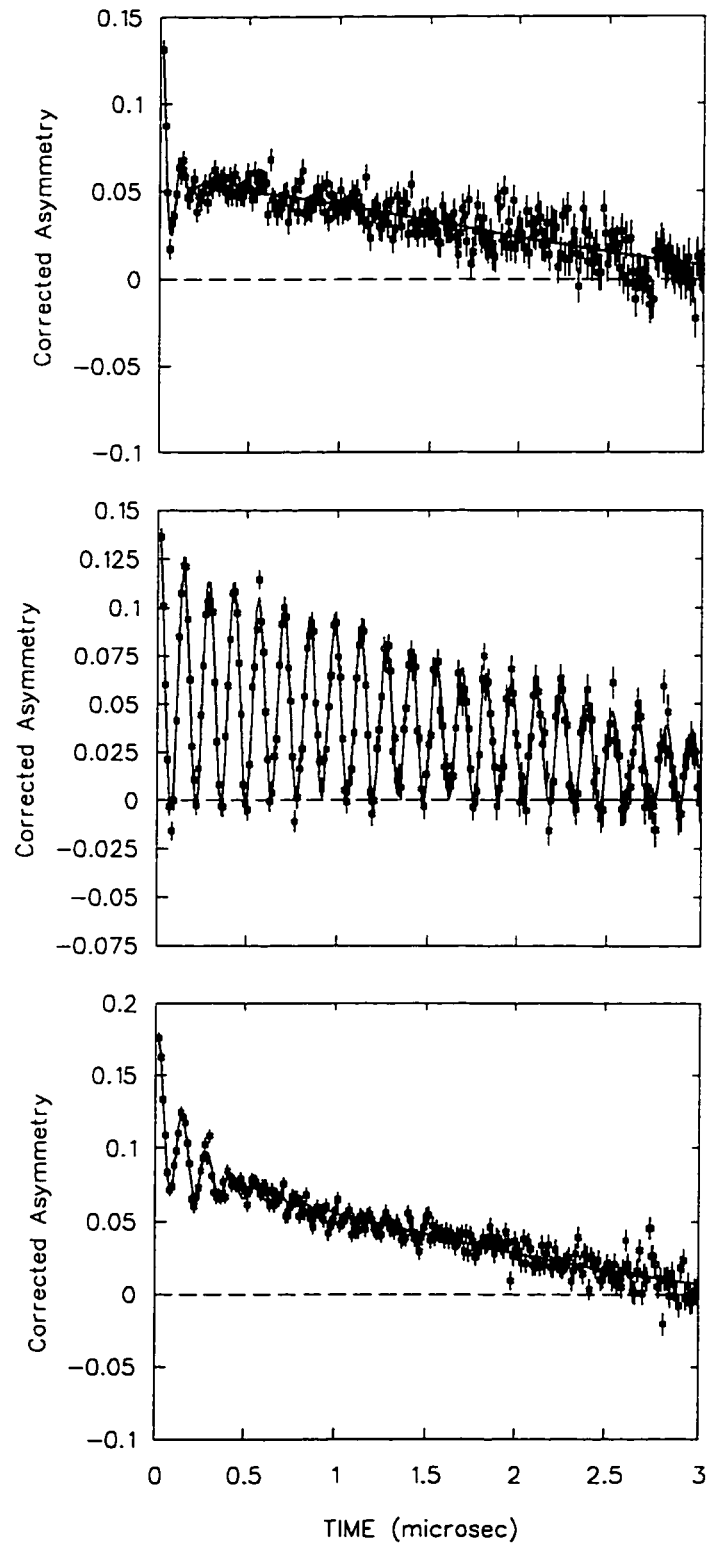


Figure 6.19: Muon spin polarization asymmetries measured in a transverse magnetic field of 5.2 G at temperatures of, from top to bottom,  $T=3.45$ , 19 and 54 K in a sample of solid, pure  $N_2$ .

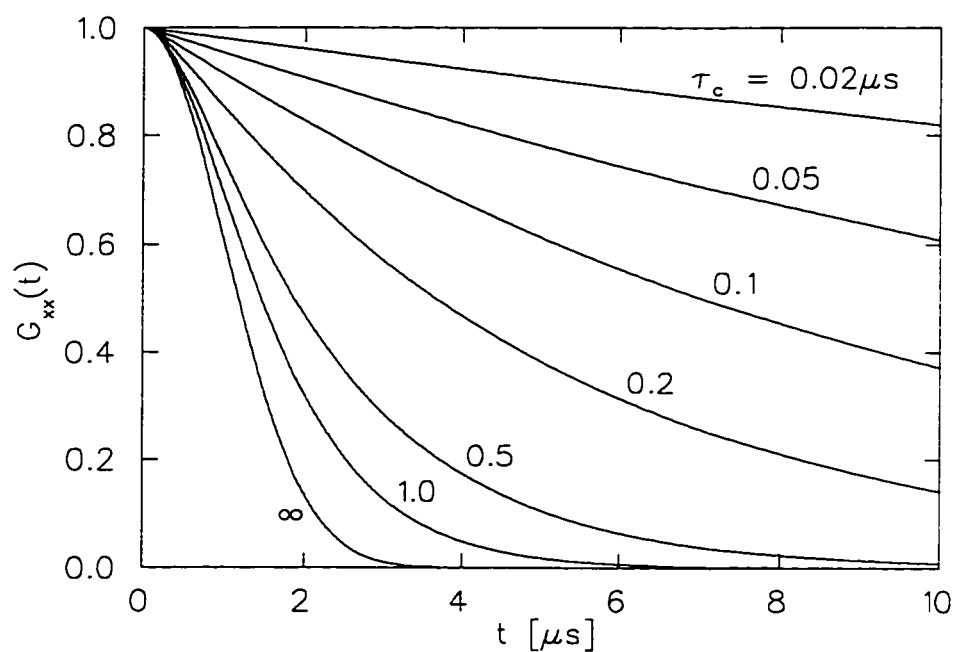


Figure 6.20: Theoretical muonium spin relaxation functions in transverse field, showing the change from Gaussian to exponential form and reduction in the relaxation rate due to motional narrowing. For all curves  $\delta = 1 \mu\text{s}^{-1}$ .

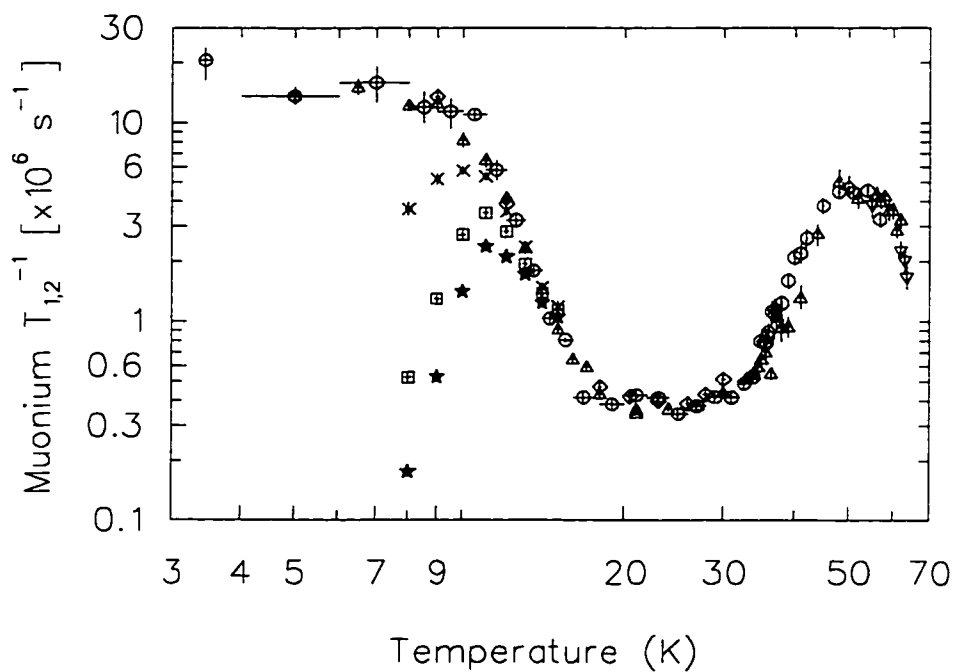


Figure 6.21: Muonium spin polarization relaxation rates measured in solid nitrogen. Stars (12G), boxes (8G) and crosses (4G) indicate the LF data and all other points are in TF  $\sim 5\text{G}$  for different samples.

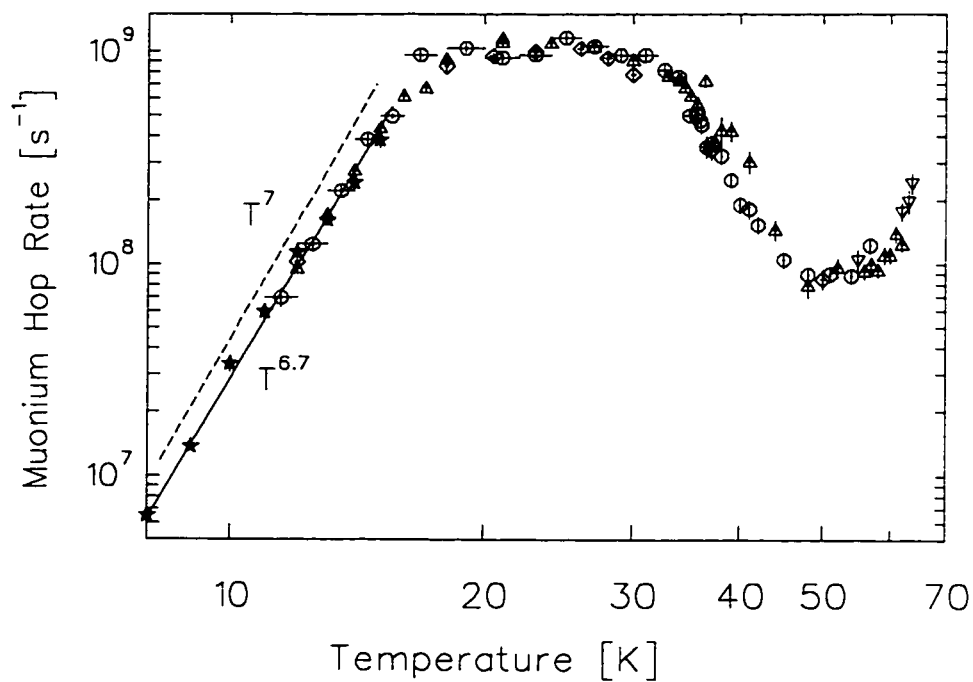


Figure 6.22: Muonium hop rate  $1/\tau_c$  in solid  $\text{N}_2$  obtained from the spin relaxation rates  $1/T_1$  and  $1/T_2$  measured in LF and TF respectively. Stars indicate the results from LF data; all other points are from TF data. The power-law fit is shown by the solid line; the nearly parallel  $T^7$  theoretical dependence is shown by the dashed line, offset for clarity.

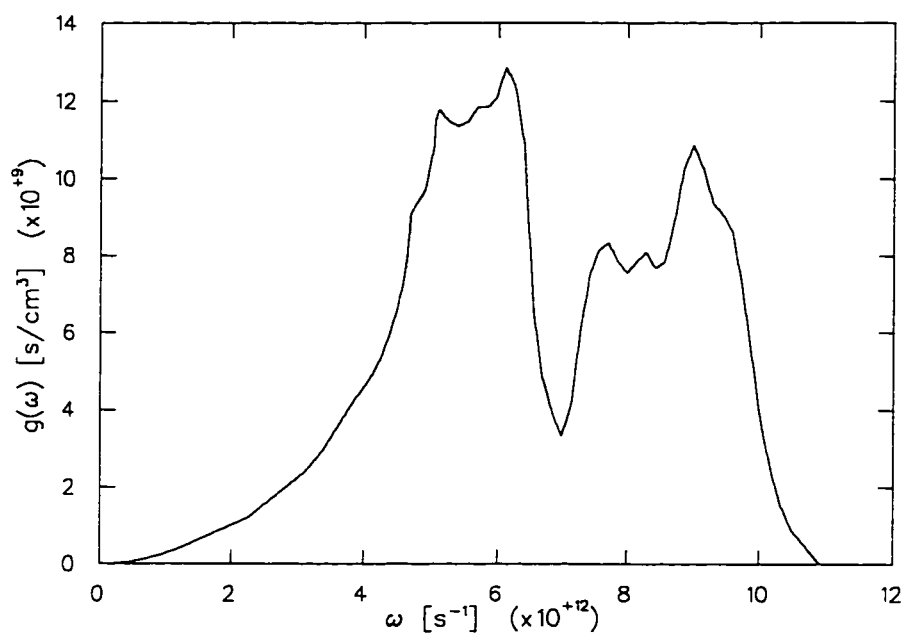


Figure 6.23: Phonon density of states  $g(\omega)$  of solid nitrogen at 22 K, data from Ref.[57].



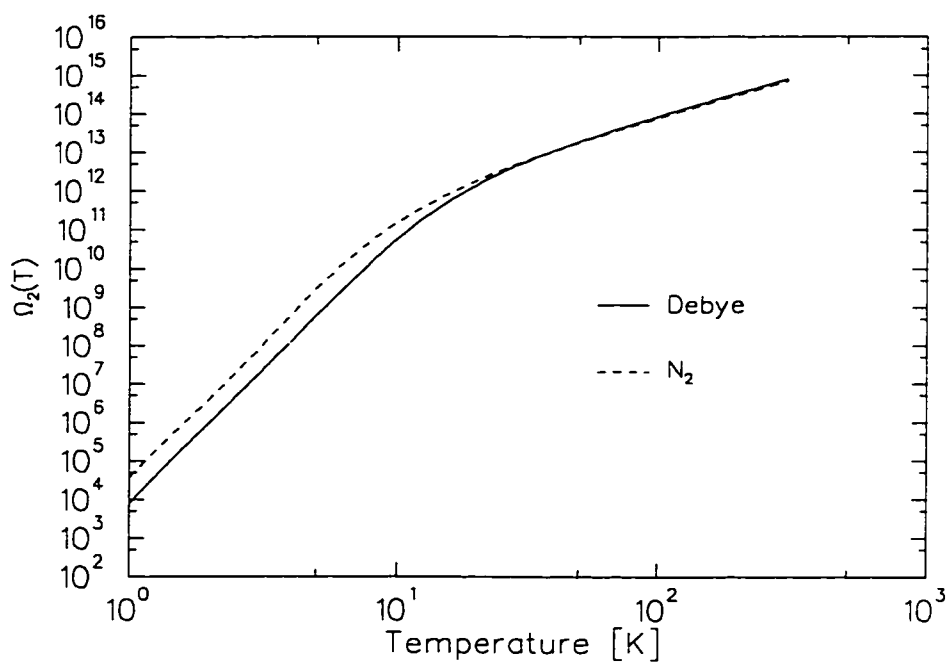


Figure 6.24:  $\Omega_2(T)$  for solid nitrogen, calculated from both the real (dashed line) and Debye model (solid line) phonon density of states  $g(\omega)$ .

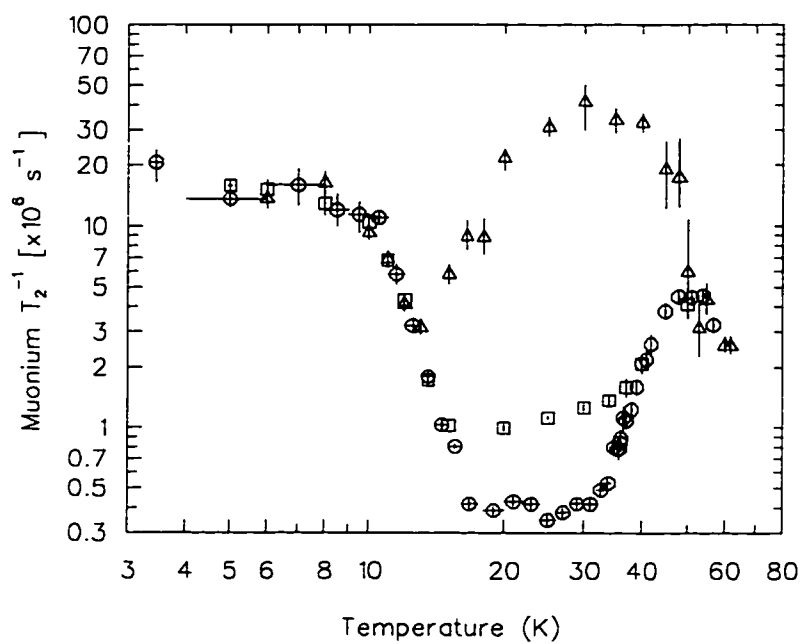


Figure 6.25: Muonium spin relaxation rates  $1/T_2$  in slowly cooled, solid high-purity  $\text{N}_2$  (circles),  $\text{N}_2$  with 0.01% CO (boxes) and  $\text{N}_2$  with 0.1% CO (triangles).

### 6.5 One-Phonon Quantum Diffusion in Solid Xe

Understanding the most important ways phonons affect the tunnelling rate is the key problem in quantum diffusion of neutral interstitials. Short-wavelength phonons produce the greatest relative motion of adjacent atoms, so these should have the greatest influence in re-shaping the potential barrier between sites. We can therefore expect that the effect of *barrier fluctuations* on the tunnelling rate should be most apparent when these phonons are excited – at temperatures comparable to the Debye temperature.

The influence of the thermal motion of lattice atoms on the diffusion rate *via* barrier fluctuations is probably best detected by measuring the hop rate over as wide a range of temperatures as possible, so that the onset of barrier fluctuations becomes apparent, while tunnelling diffusion still dominates over classical over-barrier diffusion. A light interstitial can follow the fluctuations of the lattice adiabatically, and also has a larger bandwidth for tunnelling. It follows that the most favourable conditions for detecting the effect of thermal fluctuations on the tunnelling rate would be with a light interstitial in a lattice with a low Debye temperature. In such cases the lattice can be hot enough for the entire phonon spectrum to be appreciably excited, but still at temperatures where quantum effects should dominate interstitial diffusion. Muonium diffusion in solid Xe is an extreme example of a light particle in a heavy, weakly interacting lattice, ( $m_{\text{Xe}}/m_{\text{Mu}} = 1158$ ) and as such offers the best possibility to date of detecting the effect of lattice dynamics on light interstitial quantum diffusion.

Earlier we derived an expression, Eq. 5.35, for the hop rate at intermediate temperatures where the interstitial diffuses by phonon-mediated activated hopping. This can be rewritten in the form

$$1/\tau_c = 4\Delta_0^2 e^{2(G-\phi)} \int_{-\infty}^{\infty} dt \left[ e^{\Psi(t)-i\psi(t)} - 1 \right] \quad (6.20)$$

in which

$$2(G - \phi) = \sum_{\alpha} \left\{ \left| \frac{B_{\alpha}}{\bar{\omega}_0} \right|^2 - \left| \frac{C_{\alpha}}{\omega_{\alpha}} \right|^2 \right\} \coth \left( \frac{\omega_{\alpha}}{2T} \right) \quad (6.21)$$

and

$$\bar{\Psi}(t) = \sum_{\alpha} \left\{ \left| \frac{C_{\alpha}}{\omega_{\alpha}} \right|^2 + \left| \frac{B_{\alpha}}{\bar{\omega}_0} \right|^2 \right\} \frac{\cos \omega_{\alpha} t}{\sinh \frac{\omega_{\alpha}}{2T}} \quad (6.22)$$

$$\Psi(t) = 2 \sum_{\alpha} \frac{C_{\alpha} B_{-\alpha}}{\omega_{\alpha} \bar{\omega}_0} \frac{\sin \omega_{\alpha} t}{\sinh \frac{\omega_{\alpha}}{2T}} \quad (6.23)$$

The couplings are assumed to follow the long wavelength asymptotic behavior. [53]

$$|C_{\alpha}|^2 = \lambda_p \omega_{\alpha} \Theta_D \quad (6.24)$$

$$\left| \frac{B_{\alpha}}{\bar{\omega}_0} \right|^2 = \lambda_B \frac{\omega_{\alpha}}{\Theta_D} \quad (6.25)$$

Replacing the sums over phonons by integrals over the phonon density of states this is approximately

$$2(G - \phi) = \int d\omega g(\omega) \coth \left( \frac{\omega}{2T} \right) \left[ \lambda_B \frac{\omega}{\Theta_D} - \lambda_p \frac{\Theta_D}{\omega} \right] \quad (6.26)$$

$$\bar{\Psi}(t) = \int d\omega g(\omega) \frac{\cos \omega t}{\sinh \frac{\omega}{2T}} \left[ \lambda_B \frac{\omega}{\Theta_D} + \lambda \frac{\Theta_D}{\omega} \right] \quad (6.27)$$

$$\Psi(t) = 2(\lambda_p \lambda_B)^{\frac{1}{2}} \int d\omega g(\omega) \frac{\sin \omega t}{\sinh \frac{\omega}{2T}} \quad (6.28)$$

In the literature the high temperature behavior is obtained by expanding Eq. (6.20) in a small region about  $t = 0$ , which contains most of the contribution to the integral. However, this leads to the approximate expression

$$1/\tau_c = \frac{2(\Delta_0 e^B)^2 \pi^{1/2}}{[(E + \gamma)T]^{1/2}} \exp \left[ -\frac{E}{T} + \frac{T}{E_B} - \frac{T\xi_B^2}{16(E + \gamma)} \right] \quad (6.29)$$

with six parameters, which we defined earlier in Eq. (5.38), that is unwieldy to use in fitting the data since the parameters are not independent, but are related through various

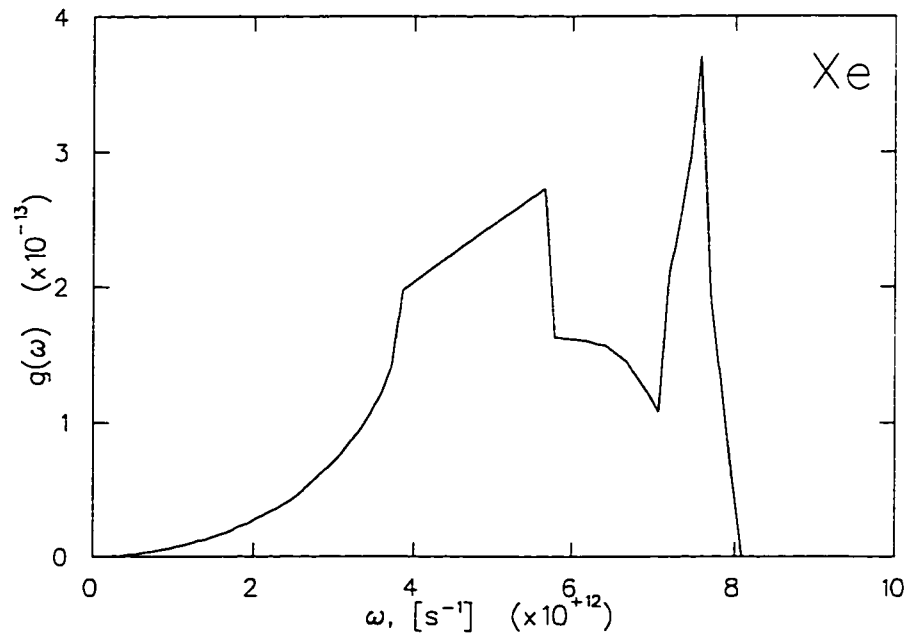


Figure 6.26: The phonon density of states of solid Xe used in the numerical evaluation of integrals over the phonon spectrum.

functions of the phonon spectrum. A more satisfactory approach is to evaluate Eq. (6.20) directly with only 3 parameters and without making the approximations in Eq. (5.36).

The integrals above are calculated here by numerical methods to yield hop rates as a function of the dimensionless coupling constants  $\lambda_{p,b}$ , temperature and an overall scale factor due to the normalization of the phonon spectrum. Figure 6.26 shows the phonon density of states  $g(\omega)$  of solid Xe used in the numerical evaluation of Eqs. (6.26, 6.27, 6.28), adapted from data by Klein [59].

However, we shall need the measured hop rate before we can proceed with this calculation, so first we digress to the experiment.

## 6.6 Experimental Results in Solid Xe

Muonium spin polarization spectra were measured in solid Xe by both TF and LF methods. The relaxation of the polarization in the LF case occurs as a result of the motion of the Mu atom among atoms of the host lattice, some of which are isotopes with nuclear moments. The nuclear hyperfine (nhf) interaction between the electron bound in the Mu atom and surrounding nuclear moments leads to an additional term in the Hamiltonian describing Mu spin dynamics:

$$V_{\text{nhf}} = \sum_{\mathbf{n}} A_{\mathbf{n}} \vec{\sigma}_{\mu} \cdot \vec{\sigma}_{\mathbf{n}}(t). \quad (6.30)$$

This problem is made tractable by approximating this interaction with an effective time-dependent magnetic field  $B_{\text{eff}}(t)$  which fluctuates both in direction and magnitude as a result of the motion of the Mu atom. The Fourier transform of  $B_{\text{eff}}(t)$  gives the spectral function  $J(\omega)$  of the fluctuating effective field. Transitions among the states of the Mu atom differing in energy by  $\hbar\omega_{ij} = \hbar(\omega_i - \omega_j)$  are induced in proportion to  $J(\omega_{ij})$ , hence changing the muon spin state and irreversibly reducing the muon spin polarization. The resulting muon spin polarization function was calculated by Celio and Meier [63] and Celio and Yen [64, 65].

For slowly diffusing muonium where  $1/\tau_c$  is small compared to all transition frequencies except the smallest -  $\omega_{12}$  - the relaxation function is well approximated by a simple exponential with a relaxation rate

$$1/T_1 = \frac{\delta^2 \tau_c}{1 + \omega_{12}^2 \tau_c^2}. \quad (6.31)$$

The temperature dependence of this relaxation rate is shown in Fig. 6.27, demonstrating that, at least for temperatures from 40 to 120 K, the muonium hop rate increases with temperature.

In general the time evolution of the muon polarization is a complicated function of the inverse correlation time  $1/\tau_c$ , the exchange coupling  $\delta$  and LF field  $B$ , which can be calculated numerically by the algorithm due to Celio. The muonium diffusion hop rate  $1/\tau_c$  at each temperature is extracted from the LF data by simultaneously fitting the polarization functions measured in several different magnetic fields to the complete theoretical polarization function. The resultant temperature dependence of the Mu hop rate is shown in Fig. 6.28.

In order to elucidate the nature of the peculiar change in relaxation rate at temperatures above  $T = 130$  K, a TF experiment on a sample of solid  $^{136}\text{Xe}$  was also performed. The resulting relaxation rate  $1/T_2$  is also shown in Fig. 6.27. Since  $^{136}\text{Xe}$  atoms do not have nuclear moments there should not be any contribution to spin relaxation due to dipolar broadening. Electric field  $\mu\mathcal{SR}$  experiments were unable to cause any change in the polarization function at any temperature, so we cannot be certain exactly what caused the additional relaxation, however it is probably of a chemical nature, and comes into effect at high temperatures where the muonium is most rapidly diffusing. We will therefore restrict ourselves to temperatures below 120 K where this anomalous contribution to the relaxation rate in longitudinal field is negligible.

The same results are also presented in the form of an Arrhenius plot in Fig. 6.30. The hop rate as a function of temperature can be fitted quite adequately to an Arrhenius function,

$$1/\tau_c = \nu_0 e^{-E_a/k_B T} \quad (6.32)$$

representing a simple over-barrier classical hopping mechanism with hop attempt rate  $\nu_0$  and activation energy  $E_a$ . Such a fit yields  $\nu_0 = 1.75(1) \times 10^{12} \text{ s}^{-1}$ , about twice the Debye frequency, and a barrier height  $E_a = 0.0482(2) \text{ eV}$ . It is difficult to immediately rule out this mechanism on grounds of the barrier height, since it is not unreasonable.

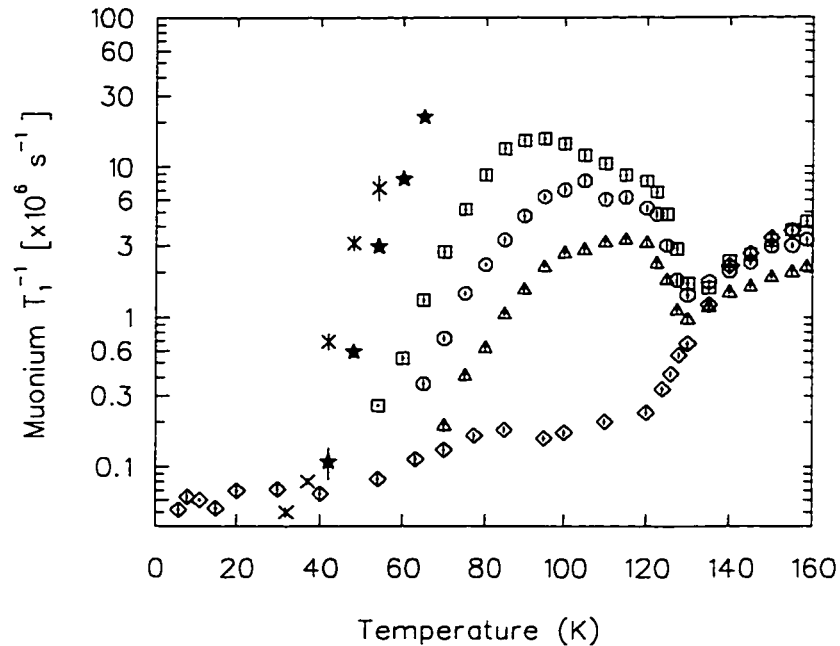


Figure 6.27: Muonium spin relaxation rates in solid Xe. Longitudinal relaxation rates  $1/T_1$  measured in natural solid Xe in various magnetic fields (triangles:1451 G, circles:725 G, squares:363 G, stars: 72 G and crosses:21 G). The other points (diamonds) are  $1/T_2$  measured in solid  $^{136}\text{Xe}$ .

(We shall, however, discuss a calculation of the shape of the potential well of Mu in Xe in Section 6.8, which estimates the depth of the potential well to be about 1 eV.) On the other hand, the indicated attempt frequency is more than a factor of 10 smaller than what one expects. The attempt rate on the barrier in the case of over-barrier activation would be the zero-point frequency  $\tilde{\omega}_0$  of the particle in the well. Since the interaction between atoms of a van der Waals solid has the same origin as the barrier to diffusion of muonium atoms we can make a rough estimate of  $\tilde{\omega}_0$  by assuming that the interstitial occupies a site where it is subject to a potential similar to that which holds the lattice atoms at their equilibrium positions. Assuming a harmonic potential, we may scale the Debye frequency by the root of the ratio of the lattice atom's mass to the interstitial's



mass:

$$\tilde{\omega}_0 \simeq \sqrt{m_{Xe}/m_{Mu}} \omega_D \simeq 34\omega_D. \quad (6.33)$$

Measurements of the vibrational frequencies of hydrogen and deuterium embedded in solid Xe agree quite well with this approximation. [58, 60] Consequently, this result allows us to rule out classical over-barrier hopping being responsible for the observed hop rate since the expected frequency is about 17 times larger than the Arrhenius plot indicates.

### 6.7 Numerical Evaluation of 1-Phonon Diffusion Theory

The direct evaluation of Eq. (6.20) by numerical methods was performed to generate the theoretical function used in fitting the temperature dependence of the Mu hop rate

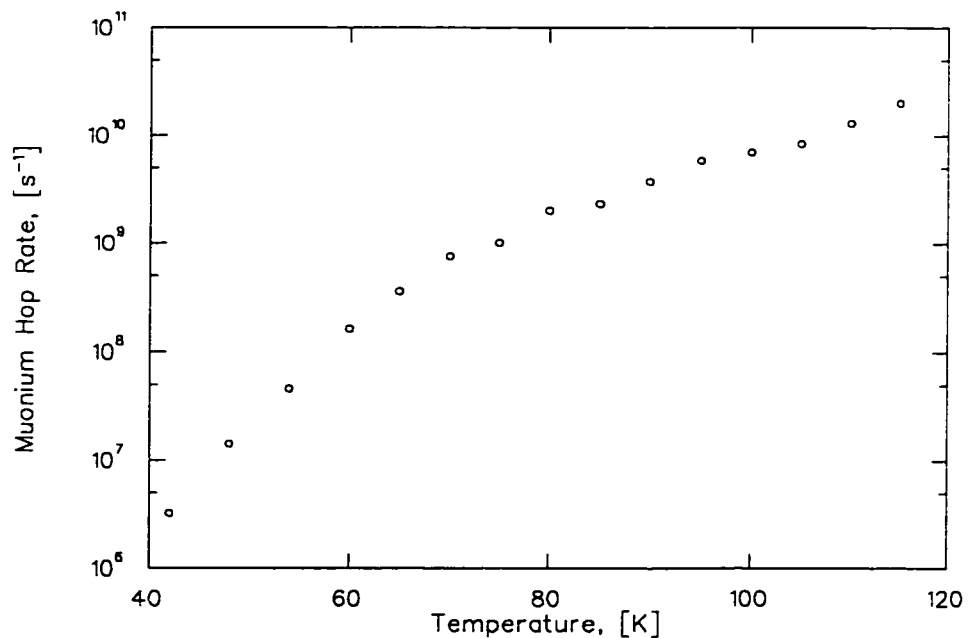


Figure 6.28: Muonium hop rate in solid Xe extracted from the LF data by simultaneous fits to data in different magnetic fields at each temperature.

in terms of three parameters; the tunnelling bandwidth  $\Delta_0$ , and dimensionless coupling parameters  $\lambda_B$  and  $\lambda_p$ . Since the phonon spectrum includes an arbitrary normalization that is folded into the coupling parameters, the overall normalization is arbitrary. However, the ratio of the coupling parameters tells us their relative strength, and determines the course of the temperature dependence.

Figure 6.29(a) shows an example of the integrand of Eq. (6.20), a function of time. The point to be made here is that the high temperature expansion of the general theory is clearly not appropriate for all values of the coupling constants. The structure in this function away from  $t = 0$  is due to phonons in the middle of the phonon spectrum; the highest frequencies contribute most to the region near  $t = 0$ .

Numerical evaluation of the integrals is made difficult due to the oscillatory nature of the integrand, which contains terms in  $\cos(\omega t)$  while  $\omega t$  ranges from zero to, in principle, infinity. However, the existence of an upper cut-off in the phonon spectrum at the Debye frequency allows one to carry out the integration to a time  $t$  such that an accurate estimate of the integral in the limit that  $t \rightarrow \infty$  can be made. (The program that performs this calculation is discussed in Appendix B, complete with the code.) Fitting the data with hop rates calculated in this model gives the parameter values  $\lambda_b = 1.19(1)$  and  $\lambda_p = 38.8(1)$ . The resulting curve is also shown by the solid line in figure Fig. 6.30. The values of the parameters imply that the suppression of tunnelling due to the polaron self-trapping is overwhelmingly large in comparison to the benefit gained from barrier height fluctuations. A fit with the model of Flynn and Stoneham, with the hop rate given by Eq. (5.40) in which the barrier fluctuations do not enter, gives a similar fit with parameter values  $\Delta_0 = 2.50(5) \mu\text{s}^{-1}$  and activation energy  $E = 0.0508(2) \text{ eV}$ , also essentially indistinguishable from the full one-phonon theory.

### 6.8 Activated Tunnelling From Excited States

There also remains the possibility that the Mu tunnels rapidly from excited states, in which the barrier height and width would be reduced, so that the temperature dependence in the hop rate we measure is merely due to the temperature dependence of the probability of muonium occupying an excited state. We consider here a calculation of the vibrational frequency and the energy level separation of the harmonic oscillator modes of the muonium atom in the potential well defined by the xenon cage.

When several levels may be populated the total tunnelling rate from one potential well to another is the sum, assuming the states are populated according to the Boltzmann distribution,

$$\nu(T) = \frac{1}{Z} \sum_i \nu_i e^{-E_i/k_B T} \quad (6.34)$$

where  $E_i$  is the energy of level  $i$ ,  $\nu_i$  the tunnelling rate from that level and  $Z = \sum_i e^{-E_i/k_B T}$  is the partition function. In the FCC Xe lattice there are two sites, tetrahedral and octahedral, where the muonium atom may find space between the Xe atoms. We can calculate the shape of the potential well for these sites by summing the Xe–Mu pair potentials over the nearest Xe atoms at these sites, and from this obtain estimates of the energies of states in the harmonic well.

The Xe–H pair potential, at close distances  $r$  where the interaction is strongly repulsive, is approximated using the Born-Mayer potential

$$V_{\text{BM}}(r) = A e^{-\beta r} \quad (6.35)$$

with  $A=1023.3$  eV and  $\beta = 3.068$  Å. [61]

The Lennard-Jones (6,12) potential for the Xe–H pair

$$V_{\text{LJ}} = \eta \left[ (r_0/r)^{12} - 2(r_0/r)^6 \right] \quad (6.36)$$

with depth  $\eta=7.08$  meV and equilibrium separation  $r_0 = 3.82$  Å [62] is probably less accurate here since the equilibrium distance between each Xe atom and caged Mu atom is much shorter than the isolated Xe–Mu pair equilibrium separation of the Lennard-Jones potential. (The lattice constant of solid Xe at 30 K is 6.197 Å.) If the Xe cage around the Mu atom does not relax, the Mu atom is 0.72 Å into the repulsive term of the potential, not near the minimum where the Lennard-Jones potential is more appropriate.

Within about 1 Å of the equilibrium position of the Mu atom in the Xe cage this potential is very well approximated by a harmonic oscillator potential

$$V_{\text{BM}}(r) = 1/2 D_{\text{BM}} |r - r_0|^2 + \text{const.} \quad (6.37)$$

where  $|r - r_0|$  is the displacement from the equilibrium position  $r_0$  at the potential minimum in the well, and  $D_{\text{BM}}$  is the restoring force constant. The energy levels of the quantum harmonic oscillator are spaced by an amount

$$\hbar\omega_{\text{sho}} = \hbar\sqrt{D_{\text{BM}}/m} \quad (6.38)$$

for a particle of mass  $m$  in the well. Along the (111) direction in solid Xe the resulting constant is  $D_{\text{BM}} = 1.12$  eV/Å<sup>2</sup> and this gives the Mu vibrational energy  $\hbar\omega_{\text{sho}} = 0.202$  eV, compared to the activation energy obtained from the Arrhenius plot  $E_a = 0.048$  eV. A similar calculation with the steeper Lennard-Jones potential and also with the Born-Mayer potential at the tetrahedral site, which allows less volume for the Mu atom, gives yet higher excitation energies.

If the Xe atoms are allowed to move away from the Mu atom, relaxing the strain imposed by the short Xe-Mu distance, the larger space for the Mu atom lowers the energy levels. The size of this shift can be estimated by iteratively minimizing the potential energy of Xe atoms and the Mu atom in a finite cluster of atoms. This calculation was done for a  $5 \times 5 \times 5$  unit cell cluster, with the Xe atoms at the surfaces of the cluster

held at fixed positions of the undisturbed Xe lattice, and a Mu atom at the octahedral site of the central unit cell. After allowing all of the interior Xe atoms to find their new local potential minima, the new sites of the 6 nearest-neighbour Xe atoms that define the octahedral site are found to be displaced  $0.20 \text{ \AA}$  away from the Mu atom. The potential of the Mu atom was then computed along the (111) direction through the octahedral site, with the lattice atoms now fixed, as shown in Fig. 6.31. (The heavy Xe atoms will not be able to follow the fast motion of the Mu atom.) Near the octahedral site the Mu potential is characterised by a force constant  $d = 0.485 \text{ eV/\AA}^2$ , and is indicated by the dashed line. The first few energy levels of the resulting quantum harmonic oscillator  $E_n = \hbar\omega_{\text{sho}}(n + \frac{1}{2})$  are also shown, in which  $\hbar\omega_{\text{sho}} = 0.131 \text{ eV}$ , about 2.7 times larger than the measured activation energy  $E_a$ .

We should conclude from this that classical thermal activation to excited states cannot be ruled out as being responsible for the temperature dependence of the Mu diffusion rate: the similarity of the calculated energy to the measured activation energy is simply too close for this question to be settled by this model. If muonium diffuses in solid Xe by quantum tunnelling, there is no evidence that barrier fluctuations play a role at any temperature, even under the most promising conditions for its detection.

At the temperatures being considered here there is a difficulty with any model involving coupling to phonons: the lack of knowledge of the frequency-dependence of the coupling parameters at frequencies that are no longer small compared to the Debye frequency. Further progress in understanding exactly how the interstitial couples to lattice excitations at frequencies where the solid is no longer Debye-like is clearly necessary if we are to fully understand the role of phonons in quantum diffusion. For example, direct measurement of the coupling constants as a function of wave vector (and polarization with respect to the lattice) are in principle possible by measuring the muonium hop rate while injecting phonons of a single wave vector at low temperature. This would have

an enormous advantage over the indiscriminate thermal excitation of the entire phonon spectrum which has been the only method used thus far.

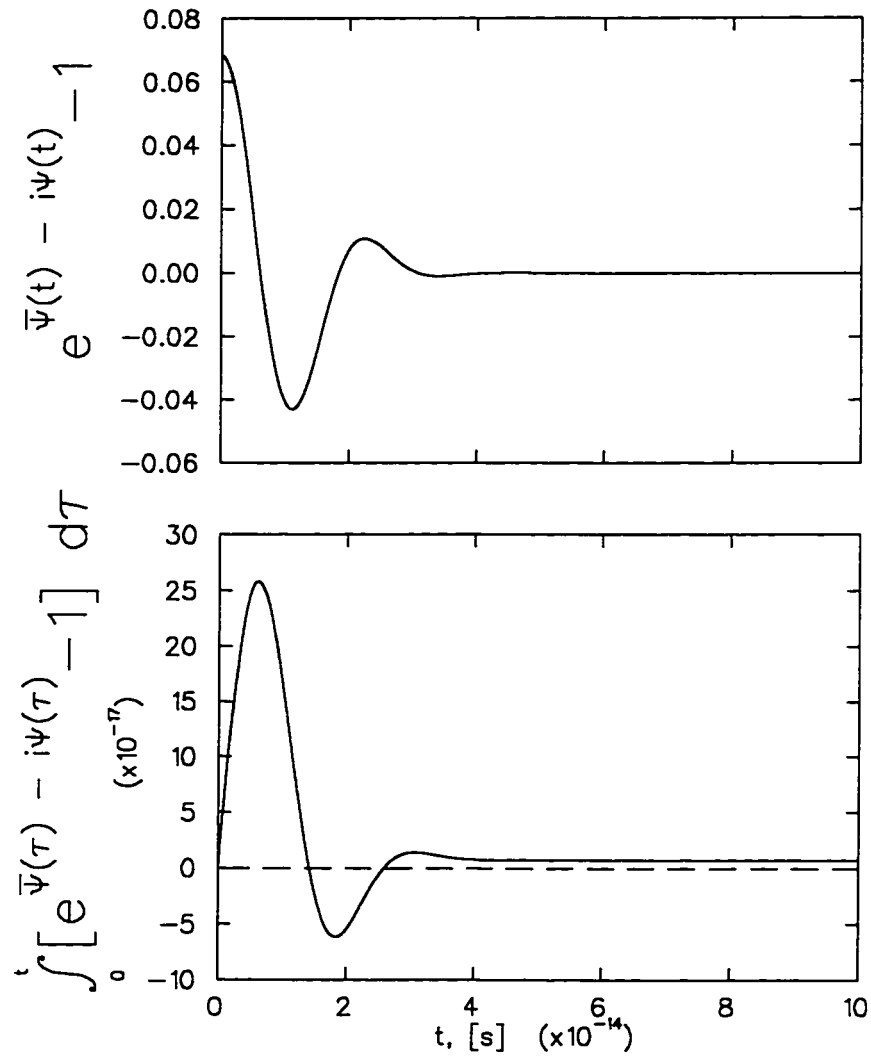


Figure 6.29: An example of the integrand (top) and integral (bottom) of Eq. 6.20 calculated with the phonon spectrum of solid Xe and parameter values  $\lambda_p/\lambda_B = 65$ . The difficulty in evaluating these multiple integrals arises from their oscillatory nature; the integral approaches a small constant value as  $t \rightarrow \infty$ . The parameters in this relatively forgiving example were chosen to make the limiting value of the integral visible by eye.

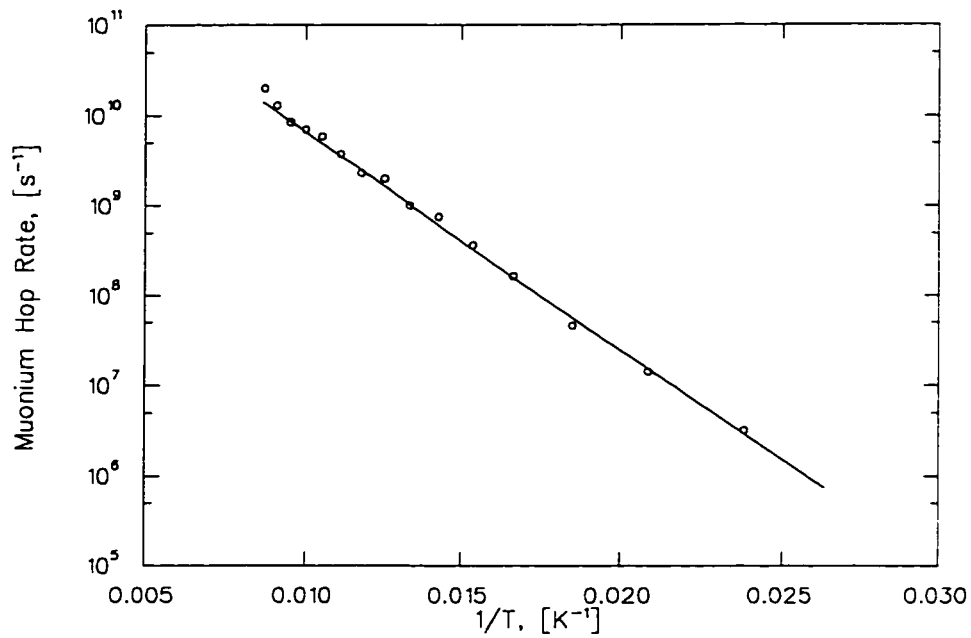


Figure 6.30: The Mu hop rate in solid Xe presented in an Arrhenius plot, with the solid line showing the fit to theory calculated by numerical integration. A simple classical model also falls on this line, as does the Flynn-Stoneham model, since all these models are of the same exponential form.



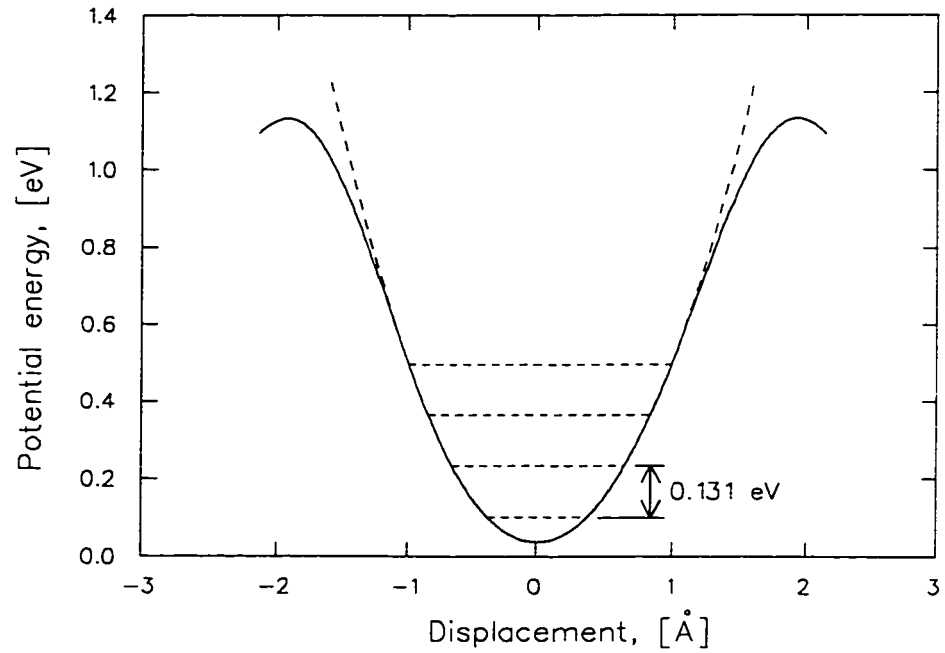


Figure 6.31: Potential energy of the Mu atom as a function of displacement from the centre of the octahedral site, along the [111] direction. The configuration of Xe atoms was computed by minimizing the potential of each atom in a  $5 \times 5 \times 5$  unit cell cluster, with the interstitial Mu at the centre.

## Chapter 7

### Conclusions

This thesis has presented experimental results about two separate topics within the field of muon spin rotation/relaxation/resonance ( $\mu\mathcal{SR}$ ) spectroscopy: The role of electron transport in muonium formation and quantum diffusion of muonium in insulators. These are summarized separately below.

#### 7.1 Muonium Formation *via* Electron Transport

The first part of this work presented results from  $\mu\mathcal{SR}$  experiments in which the muon and muonium asymmetries in insulators were measured in the presence of an externally applied electric field. These experiments have found that an electric field can, in some insulators, influence the fraction of muons that form muonium atoms. Furthermore, the amount of muonium formed depends also on the orientation of the electric field with respect to the initial momentum of the muon. These results imply that there is an anisotropic spatial distribution of electrons with respect to the muon, and that the electric field influences the probability of forming muonium by drifting these electrons either away from or toward the muon.

It can be concluded that muonium is formed, at least sometimes, from electrons that move considerable distances through the sample to the site of the muon. A modest electric field having any effect *at all* implies that the electron spends some time (between being stripped from an atom and finding the muon) in a low-field region far from these charged ions. Previously it had been thought that muonium formed when an electron

was stripped from an atom and promptly captured by the passing muon, which then thermalized with no further ionization. In this scenario the bare electron would never be sufficiently far from the muon or the ion left behind that an external electric field could compete with the Coulomb fields of their positive charges. It is likely that in most insulators that both mechanisms occur to varying degrees. For example, in solid nitrogen the magnetic field dependence of the muonium amplitude showed that at least 22% of the muonium was formed by the delayed mechanism, the remaining muonium fraction being formed rapidly would include hot (prompt) muonium.

One way for the delayed process to come about is by a hot muonium atom, after moving away from the last ion from which the electron came, undergoing a collision with a neutral atom, ionizing the muonium and putting the electron back into the lattice with a fraction of the muonium kinetic energy. The muon sometimes would continue on, still with the last few electron-volts of its initial kinetic energy, and eventually thermalize further downstream. In this picture neither the electron or muon are left in the immediate vicinity of any other ion. The electron is in an otherwise undisturbed region of the lattice where the magnitude of the Coulomb field of the muon can be comparable to the externally applied field, so the external field can affect the electron's subsequent trajectory. Most importantly, this electron is the closest one to the muon and therefore is the one that reaches the thermal muon first. The asymmetry of the electron distribution also implies that the direction of travel of the muon, at the very end of the track, is still predominantly in the direction of the muon beam.

Currently, one technology being developed for producing beams of spin polarized muons with kinetic energies of a few eV relies on cryogenic insulating materials, such as the solid rare gases, as moderators.[29, 30] A good understanding of low energy end-of-track processes of charged particles in general – which is still lacking – will be valuable

in selecting materials that should minimize muonium formation, and maximize the probability of these slow muons escaping the moderator surface.

## 7.2 Quantum Diffusion in Insulators

Diffusion of interstitial muonium in insulators was studied by making use of the effect of the motion of the muonium atom on the spin polarization relaxation functions in both transverse and longitudinal magnetic fields.

Quantum diffusion of neutral interstitials in insulators is dominated by the interaction of the particle with excitations of the lattice. These excitations are manifested in the displacements of the lattice atoms from their equilibrium positions, which results in the loss of translational symmetry (for the bare interstitial), reducing the tunnelling rate. For muons in metals this interaction is negligible compared to the Coulomb interaction with conduction electrons. Quantum diffusion of neutral interstitials in insulators gives us a means of studying this interaction.

Scattering of phonons results in a reduction of the effective tunnelling bandwidth. At temperatures where the incoherent channel has not been completely quenched the key characteristic of 2-phonon quantum diffusion (in an otherwise perfect lattice) is an increasing hop rate as the temperature decreases. Below about  $T = \Theta_D/10$  theory predicts that the hop rate will follow a  $T^{-7}$  power law. At a higher temperature this strong temperature dependence drops off as the phonon spectrum becomes fully excited. Structure in the phonon density of states is not very important to the overall temperature dependence of the hop rate.

At sufficiently low temperatures the site-to-site static level shifts that are always present in a real crystal will inevitably become important. The small difference between energy levels must be made up by differences in phonon energies, and in this situation

the 2-phonon hop rate increases with temperature as  $T^7$ , below about  $T = \Theta_D/10$ . This interplay between the phase damping rate  $\Omega_2$  and typical static shifts  $\xi$  was demonstrated by muonium diffusion in solid nitrogen. Between about 4 K and 20 K the muonium hop rate follows a  $T^{6.7(1)}$  power law, slightly weaker than the predicted  $T^7$  law for the case in which small static shifts are present, well below the Debye temperature. At higher temperatures, between 32 K and 46 K the hop rate was found to decrease with rising temperature, qualitatively consistent with theory for the case that  $\Omega_2$  completely dominates the static shifts. However, the measured temperature dependence was found to be much stronger than theory predicts at such a large fraction of the Debye temperature, assuming that it is phonons that are being scattered.

It is thought that at higher temperatures activated tunnelling diffusion of polarons should be sensitive to the fluctuations in the height and width of the potential barrier separating interstitial sites. The most favourable conditions for detecting this would therefore be at temperatures where short-wavelength phonons are excited. These phonons should cause the greatest relative motion of adjacent atoms which define the shape of the barrier.

Muonium diffusion in solid xenon was studied in an effort to detect this effect. However the data did not reveal a temperature dependence in the apparent activation energy. Furthermore, the results are consistent with diffusion from an excited state, so that the temperature dependence we measure reflects the thermal population of this excited state. A simple calculation based on Xe-Xe and Xe-H pair potentials shows that the separation of levels in the Xe cage, deformed to allow room for the muonium interstitial at the octahedral site, would be about the same as the measured activation energy.

It would appear that current theory is adequate for modelling phonon-mediated quantum diffusion at temperatures where solids are Debye-like and only the long-wavelength phonons are excited. Exactly which excitations are important at higher temperatures

has not yet been resolved. Perhaps the next stage in experimental work is to measure directly the contribution of various modes, not by measuring temperature dependences, but by measuring the diffusion rate while exciting only a narrow part of the excitation spectrum.

## Bibliography

- [1] *The 1986 CODATA Recommended Values of Fundamental Physical Constants*. E. Richard Cohen and Barry N. Taylor eds, *J. Res. National Bureau of Standards*. **92(2)**, 1 (1987).
- [2] A.E. Pifer, T. Bowen, K.R. Kendall, *Nucl. Instrum. Methods* **135**, 39 (1976).
- [3] T. Bowen, *Physics Today* **38(7)**, 22 (1985).
- [4] A. Schenck, *Muon Spin Rotation: Principles and Applications in Solid State Physics* (Adam Hilger, Bristol, 1986).
- [5] J.W. Schneider, "Longitudinal-Field Methods", *proc.  $\mu$ SR Summer School*. Maui. May 31 - June 4, 1993.
- [6] J.H. Brewer, "Muon Spin Rotation/Relaxation/Resonance" in *Encyclopedia of Applied Physics*, (1996).
- [7] P.W. Percival, H. Fischer, M. Camani, F.N. Gygax, W. Rüegg, A. Schenck, H. Schilling, H. Graf, *Chem. Phys. Lett.* **39**, 333 (1976).
- [8] P.W. Percival, E. Roduner, H. Fischer, *Chem. Phys.* **32**, 353 (1978).
- [9] P.W. Percival, E. Roduner, H. Fischer in *Positronium and Muonium Chemistry*, *Adv. in Chem. Ser.*, **175**, 335 (1979).
- [10] O.E. Mogensen, *J. Chem. Phys.* **60**, 998 (1974).
- [11] D.G. Fleming, D.M. Garner, L.C. Vaz, D.C. Walker, J.H. Brewer, K.M. Crowe in *Positronium and Muonium Chemistry*, *Adv. in Chem. Ser.* **175**, 279 (1979).
- [12] J.H. Brewer, K.M. Crowe, F.N. Gygax, A. Schenck in *Muon Physics* vol.3. V.W. Hughes, C.S. Wu eds. Academic Press, New York (1975).
- [13] R.E. Turner, M. Senba, *Proceedings of the Yamada Conference VII, Muon Spin Rotation*, Shimoda, Japan. *Hyp. Int.* **17-19**, 697 (1984).
- [14] Yasuo Ito, Yoneho Tabata, *Proceedings of the 5<sup>th</sup> International Conference on Positron Annihilation*, Japan, p.325 (1979).
- [15] Y. Ito, B.W. Ng, Y.C. Jean, D.C. Walker, *Hyp. Int.* **8**, 355 (1981).

- [16] S.F.J. Cox, *J. Phys. C* **20**, 3187 (1987).
- [17] D.G. Fleming *et al.*, *Phys. Rev* **A26**, 2527 (1982).
- [18] David C. Walker, *Muon and Muonium Chemistry*, Cambridge University Press (1983).
- [19] R.J. Loveland, P.G. Le Comber and W.E. Spear, *Phys. Rev.* **B6**, 3121. (1972).
- [20] T.A. Scott, *Phys. Rep. Phys. Lett.* **C27**, 89, (1976).
- [21] W.E. Streib, T.H. Jordan, W.N. Lipscomb, *J. Chem. Phys.* **37**, 2962 (1962).
- [22] F.W. Terman, T.A. Scott. *Bull. Am. Phys. Soc* **3**, 23 (1958).
- [23] V.S. Kogan, T.G. Omatov, *Soviet Phys JETP*, **17**, 1260 (1963).
- [24] G. Pangilinan, G. Guelachvili, R. Sooryakumar, K. Narahari Rao and R.H. Tipping. *Phys. Rev.* **B39**. 2522 (1989).
- [25] E.P. Krasnoperov, E.E. Meilikhov, A.N. Ponomarev, V.Yu. Pomyakushin, D.G. Eschenko, V.N. Duginov, V.A. Zhukov, T.N. Mamedov and V.G. Olshevskii, *Sov. Phys. JETP Lett.* **59**, 749 (1994),
- [26] E. Krasnoperov, E.E. Meilikov, D. Eschenko, D. Herlach, E. Morenzoni, U. Zimmermann, F.N. Gygax, A. Schenck, *Hyp. Int.* **85**, 1017 (1994).
- [27] E. Krasnoperov, E.E. Meilikov, D. Eschenko, D. Herlach. E. Morenzoni. U. Zimmermann, F.N. Gygax, A. Schenck, *Hyp. Int.* **85**, 1011 (1994).
- [28] E. Krasnoperov, E. Meilikov, R. Abela, D. Herlach, E. Morenzoni, F.N. Gygax. A. Schenck, D. Eschenko, *Phys. Rev. Lett.* **69**, 1560 (1992).
- [29] M. Meyberg, E. Morenzoni, T. Wutzke, U. Zimmermann, F. Kottmann, K. Jungmann, B. Matthias and T. Prokscha, *Hyp. Int.* **85**, 1075 (1994).
- [30] E. Morenzoni, M. Birke, H. Gluckler, A. Hofer, J. Litterst, M. Meyberg, C. Niedermayer, Th. Prokscha, G. Schatz and Th. Wutzke *Hyp. Int.* **106**, 229 (1996)
- [31] T. Holstein, *Ann. Physics* **8**, 343 (1959).
- [32] A.F. Andreev and I.M. Lifshitz, *Zh. Eksp. Teor. Fiz.* **56**, 2057 (1969) [*Sov. Phys. JETP* **29**, 1107 (1969)].
- [33] C.P. Flynn and A.M. Stoneham, *Phys. Rev.* **B1**, 3966 (1970).



- [34] Yu.M. Kagan and L.A. Maksimov, *Zh. Eksp. Teor. Fiz.* **65**, 622 (1973) [*Sov. Phys. JETP* **38**, 307 (1974)].
- [35] Yu.M. Kagan and M.I. Klinger, *J. Phys.* **C7**, 2791 (1974).
- [36] Yu. Kagan and M.I. Klinger, *Zh. Eksp. Teor. Fiz.* **70**, 255 (1976) [*Sov. Phys. JETP* **43**, 132 (1976)].
- [37] Yu.M. Kagan and N.V. Prokof'ev, "Quantum Tunneling Diffusion in Solids". in *Quantum Tunneling in Condensed Media*, eds. A.J. Leggett and Yu.M. Kagan (North-Holland, 1992), p. 37.
- [38] A.O. Caldeira and A.J. Leggett, *Phys. Rev. Lett.* **46**, 211 (1981).
- [39] A.J. Leggett, S. Chakravarty, A.T. Dorsey, Matthew P.A. Fisher, Anupam Garg, W. Zwerger, *Rev. Mod. Phys.* **59**, 1 (1987).
- [40] N.V. Prokofe'ev, *Phil. Trans. Roy. Soc. London*, **A350**, 287 (1995).
- [41] D. Steinbinder *et al.*, *Europhys. Lett.* **6**, 535 (1988).
- [42] R. Kadono, J. Imazato, T. Matsuzaki, K. Nishiyama, K. Nagamine, T. Yamazaki, D. Richter, J.-M. Welter, *Phys. Rev.* **B39**, 23 (1989).
- [43] R. Kadono, *Hyperfine Int.* **64**, 615 (1990).
- [44] R. Kadono, R.F. Kiefl, E.J. Ansaldo, J.H. Brewer, M. Celio, S.R. Kreitzman, G.M. Luke, *Phys. Rev. Lett.* **64**, 665 (1990).
- [45] R. Kadono, R.F. Kiefl, W.A. MacFarlane, S.R. Dunsiger, *Phys. Rev.* **B53**, 3177 (1996).
- [46] G.M. Luke, J.H. Brewer, S.R. Kreitzman, D.R. Noakes, M. Celio, R. Kadono, and E.J. Ansaldo, *Phys. Rev.* **B43**, 3284 (1991)
- [47] O. Hartmann, E. Karlson, E. Wäcklegard, r. Wäppling, D. Richter, R. Hempelman, and T.O. Niinikoski, *Phys. Rev.* **B37**, 4425 (1988).
- [48] J.W. Schneider *et al.*, *Phys. Rev. Lett.* **68**, 3196 (1992).
- [49] V. Storchak *et al.*, *Phys. Lett.* **A32**, 77 (1992).
- [50] J. Kondo, *Physica* **125B**, 279 (1984) and **126B**, 377 (1984)
- [51] K. Yamada, *Prog. Theor. Phys.* **72**, 195 (1984).
- [52] Yu.M. Kagan and N.V. Prokof'ev, *Phys. Lett.* **A159**, 289 (1991).

- [53] Yu. Kagan and N.V. Prokof'ev, in *Quantum Tunnelling in Condensed Matter*. Yu. Kagan and A.J. Legget eds., Elsevier Science Publishers B.V., 1992.
- [54] Yu. Kagan and N.V. Prokof'ev, *Phys. Lett.* **A150**, 320 (1990).
- [55] R.W. MacPherson and T. Timusk, *Can. J. Phys.* **48**, 2176; **48**, 2917 (1970).
- [56] R. Kubo, *Hyp. Int.* **8**, 731 (1981).
- [57] Cardini *et al.*, *J. Chem. Phys.* **93**, 1973 (1990)
- [58] J. Zoval and V.A. Apkarian, *J. Phys. Chem.* **98**, 7945 (1994).
- [59] M.L. Klein, in *Rare Gas Solids* Vol. 2, p. 964. M.L. Klein, J.A. Venables eds.. Academic Press (1976).
- [60] F. Wittl, J. Eberlein, Th. Epple, M. Dechant and M. Cruzberg, *J. Chem. Phys.* **98**, 9554 (1993).
- [61] K.T. Tang, J.P. Toennies, *Chem. Phys.* **156**, 413 (1991).
- [62] J.P. Toennies, W. Welz, and G. Wolf, *J. Chem. Phys.* **71**, 614 (1979).
- [63] M. Celio and P.F. Meier, *Physical Review B* **28**, 39 (1983).
- [64] M. Celio, *Helv. Phys. Acta* **60**, 600 (1987).
- [65] H.K. Yen, M.Sc. Thesis, University of British Columbia, (1988).
- [66] R.F. Kiefl, R. Kadono, J.H. Brewer, G.M. Luke, H.K. Yen, M. Celio, E.J. Ansaldo. *Phys. Rev. Lett.* **62**, 792 (1989).
- [67] W.A. MacFarlane, R.F. Kiefl, J.W. Scheider, K.H. Chow, G.D. Morris, T.L. Estle and B. Hitti, *Hyp. Int.* **85**, 23 (1994).
- [68] G. Gunnarsson and P. Hedegård, *Europhys. Lett.* **18**, 367 (1992).

## Appendix A

### Muonium Spin Polarization Function

In this Appendix we derive from first principles the eigenvalues and states of muonium. in the simplest case of free muonium in vacuum with a static magnetic field applied. The polarization functions with the applied magnetic field oriented either transverse to or along the initial muon spin are calculated. Spin relaxation is not considered in this calculation.

In the situation being considered the Hamiltonian of the muonium atom.

$$\mathcal{H} = \frac{\hbar\omega_0}{4}\boldsymbol{\sigma}_\mu \cdot \boldsymbol{\sigma}_e + \frac{g_e\mu_B}{2}B\sigma_e^z - \frac{g_\mu\mu_\mu}{2}B\sigma_\mu^z \quad (\text{A.1})$$

includes the Zeeman terms for the muon and electron spins, and the interaction between these spins. In order to determine the time dependence of the muon spin polarization we diagonalize this Hamiltonian and calculate the elements of the muon spin operator. In doing so we will obtain the muonium states and corresponding energies, which determine the precession frequencies observed in the muon spin polarization signal.

We start by defining a set of states of the muonium atom in terms of the individual

$g_\mu = 2.002331846$
$g_e = 2.002319304386$
$\mu_\mu = 4.4904514 \cdot 10^{-26} \text{ J} \cdot \text{T}^{-1}$
$\mu_e = 928.47701 \cdot 10^{-26} \text{ J} \cdot \text{T}^{-1}$

Table A.2: Muon and electron  $g$ -factors and magnetic moments.

electron and muon states,

$$\phi^{\delta\gamma} = \phi_{\mu}^{\delta} \phi_{e}^{\gamma}, \quad \delta, \gamma = \pm 1. \quad (\text{A.2})$$

the superscripts on  $\phi^{\delta\gamma}$  referring to the muon and electron spins projected onto the quantization axis, which we take to be the  $\hat{z}$  direction.

The spin operator  $\boldsymbol{\sigma} = (\sigma^x, \sigma^y, \sigma^z)$  has components given by the usual Pauli matrices and the muon and electron spin operators act only on their corresponding parts of the muonium wave function.

The operator in the first term of the Hamiltonian

$$\boldsymbol{\sigma}_e \cdot \boldsymbol{\sigma}_{\mu} \phi^{\delta\gamma} = (\sigma_{\mu}^x, \sigma_{\mu}^y, \sigma_{\mu}^z) \cdot (\sigma_e^x, \sigma_e^y, \sigma_e^z) \phi^{\delta\gamma} \quad (\text{A.3})$$

can be written in terms of raising and lowering operators which are defined by

$$\sigma_i^+ = \sigma_i^x + i\sigma_i^y \quad \text{and} \quad \sigma_i^- = \sigma_i^x - i\sigma_i^y, \quad (\text{A.4})$$

by expanding its first two terms into

$$\begin{aligned} \sigma_{\mu}^x \sigma_e^x &= \frac{1}{4} (\sigma_{\mu}^+ + \sigma_{\mu}^-) (\sigma_e^+ + \sigma_e^-) \\ &= \frac{1}{4} (\sigma_{\mu}^+ \sigma_e^+ + \sigma_{\mu}^+ \sigma_e^- + \sigma_{\mu}^- \sigma_e^+ + \sigma_{\mu}^- \sigma_e^-) \end{aligned} \quad (\text{A.5})$$

and similarly

$$\sigma_{\mu}^y \sigma_e^y = -\frac{1}{4} (\sigma_{\mu}^+ \sigma_e^+ - \sigma_{\mu}^+ \sigma_e^- - \sigma_{\mu}^- \sigma_e^+ + \sigma_{\mu}^- \sigma_e^-). \quad (\text{A.6})$$

The third term follows trivially from the definition of the spin along the quantization axis for both the muon and electron,

$$\sigma_i^z \phi_i^{\delta} = \delta \phi_i^{\delta}, \quad \text{with } \delta = \pm 1 \text{ and } i = \mu, e. \quad (\text{A.7})$$

The hyperfine interaction term is then the sum of Eqs. (A.5,A.6,A.7) and we obtain

$$\begin{aligned}\boldsymbol{\sigma}_\mu \cdot \boldsymbol{\sigma}_e &= \frac{1}{4}(\sigma_\mu^+ \sigma_e^+ + \sigma_\mu^+ \sigma_e^- + \sigma_\mu^- \sigma_e^+ + \sigma_\mu^- \sigma_e^- \\ &\quad - \sigma_\mu^+ \sigma_e^+ + \sigma_\mu^+ \sigma_e^+ + \sigma_\mu^+ \sigma_e^+ - \sigma_\mu^+ \sigma_e^+) + \sigma_\mu^z \sigma_e^z \\ &= \frac{1}{2}(\sigma_\mu^+ \sigma_e^- + \sigma_\mu^- \sigma_e^+) + \sigma_\mu^z \sigma_e^z.\end{aligned}\quad (\text{A.8})$$

Finally, noting that

$$(\sigma_\mu^+ \sigma_e^- + \sigma_\mu^- \sigma_e^+) \phi^{\delta\gamma} = \begin{cases} 2\phi^{\gamma\delta} & \delta \neq \gamma \\ 0 & \delta = \gamma \end{cases} \quad (\text{A.9})$$

Eq. (A.8) simplifies to

$$\boldsymbol{\sigma}_\mu \cdot \boldsymbol{\sigma}_e \phi^{\delta\gamma} = \delta\gamma \phi^{\delta\gamma} + (1 - \delta_{\delta\gamma}) \phi^{\gamma\delta}. \quad (\text{A.10})$$

For the two  $\delta = \gamma = \pm 1$  cases it then immediately follows that the eigenvalues are given by

$$\hbar\omega_1 = \frac{1}{4}\hbar\omega_0 + \frac{1}{2}(g_e\mu_B - g_\mu\mu_\mu)B \quad (\text{A.11})$$

$$= \frac{1}{4}\hbar\omega_0 + \hbar\omega_- \quad (\text{A.12})$$

and

$$\hbar\omega_3 = \frac{1}{4}\hbar\omega_0 - \frac{1}{2}(g_e\mu_B - g_\mu\mu_\mu)B \quad (\text{A.13})$$

$$= \frac{1}{4}\hbar\omega_0 - \hbar\omega_- \quad (\text{A.14})$$

where we have defined

$$\omega_\pm = \frac{1}{2}(\omega_e \pm \omega_\mu) \quad (\text{A.15})$$

with

$$\omega_e = g_e\mu_e B/\hbar \quad \text{and} \quad \omega_\mu = g_\mu\mu_\mu B/\hbar. \quad (\text{A.16})$$

In order to diagonalize the Hamiltonian in the other two cases where  $\delta \neq \gamma$  we define linear combinations of the basis vectors

$$\psi_2 = \cos\beta \phi^{-+} + \sin\beta \phi^{+-} \quad \text{and} \quad \psi_4 = -\sin\beta \phi^{-+} + \cos\beta \phi^{+-}. \quad (\text{A.17})$$

where the parameter  $\beta$  turns out to depend on the magnitude of the field  $B$ , as will be shown below.

Operating with the full Hamiltonian on the first of these, we obtain

$$\begin{aligned} \mathcal{H}\psi_2 &= \left[ \frac{\hbar\omega_0}{4} \sigma_\mu^z \sigma_e^z + \frac{\hbar\omega_0}{8} (\sigma_\mu^+ \sigma_e^- + \sigma_\mu^- \sigma_e^+) + B \left( \frac{g_e \mu_B}{2} \sigma_e^z + \frac{g_\mu \mu_\mu}{2} \sigma_\mu^z \right) \right] \psi_2 \\ &= \frac{\hbar\omega_0}{4} (-\psi_2) + \left[ \frac{\hbar\omega_0}{2} \sin\beta + \frac{\hbar\omega_-}{2} \cos\beta \right] \phi^{-+} \\ &\quad + \left[ \frac{\hbar\omega_0}{2} \cos\beta - \frac{\hbar\omega_-}{2} \sin\beta \right] \phi^{+-}. \end{aligned} \quad (\text{A.18})$$

If  $\psi_2$  is to be an eigenfunction of the Hamiltonian we must have both

$$\hbar\omega_0(\sin\beta + x \cos\beta) = C \cos\beta \quad (\text{A.19})$$

$$\hbar\omega_0(\cos\beta - x \sin\beta) = C \sin\beta \quad (\text{A.20})$$

where  $C$  is an arbitrary constant and we have defined

$$x = \frac{2\omega_+}{\omega_0}, \quad (\text{A.21})$$

from which it follows

$$x = [\tan(2\beta)]^{-1}. \quad (\text{A.22})$$

Equation (A.18) can now be simplified to

$$\mathcal{H}\psi_2 = -\frac{\hbar\omega_0}{4} \psi_2 + \frac{\hbar\omega_0}{2} (\tan\beta + x) \psi_2 \quad (\text{A.23})$$

and by using the trigonometric identity

$$2 \tan\beta = \tan(2\beta) (1 - \tan^2\beta) = \frac{1}{x} (1 - \tan^2\beta) \quad (\text{A.24})$$

to substitute

$$\begin{aligned}
\tan\beta + x &= \left[ \tan^2\beta + 2x \tan\beta + x^2 \right]^{1/2} \\
&= \left[ \tan^2\beta + (1 - \tan^2\beta) + x^2 \right] \\
&= (1 + x^2)^{1/2}
\end{aligned} \tag{A.25}$$

we obtain the final result

$$\mathcal{H}\psi_2 = \left[ -\frac{\hbar\omega_0}{4} + \hbar(\omega_0^2/4 + \omega_+^2)^{1/2} \right] \psi_2 = \hbar\omega_2\psi_2. \tag{A.26}$$

A similar calculation, operating on the wavefunction  $\psi_4$ , yields

$$\mathcal{H}\psi_4 = \left[ -\frac{\hbar\omega_0}{4} - \hbar(\omega_0^2/4 + \omega_+^2)^{1/2} \right] \psi_4 = \hbar\omega_4\psi_4. \tag{A.27}$$

The results so far are summarized in Figure A.32, which shows the four eigenvalues as functions of the magnetic field  $B$ .

We shall see that the polarization signal has components at frequencies determined by the transition energies  $\hbar\omega_{ij} = \hbar(\omega_i - \omega_j)$  between these states. These frequencies are

$$\omega_{12} = \omega_0/2 + \omega_- - \left( \frac{\omega_0^2}{4} + \omega_+^2 \right)^{1/2} \tag{A.28}$$

$$\omega_{23} = -\omega_0/2 + \omega_- + \left( \frac{\omega_0^2}{4} + \omega_+^2 \right)^{1/2} \tag{A.29}$$

$$\omega_{13} = 2\omega_- \tag{A.30}$$

$$\omega_{14} = \omega_0/2 + \omega_- + \left( \frac{\omega_0^2}{4} + \omega_+^2 \right)^{1/2}. \tag{A.31}$$

### A.1 Transverse Field

Now that we have the eigenvectors and eigenvalues of all four muonium states it is a straightforward task to calculate the matrix elements of the muon spin operator. Initially, the muon beam is virtually 100% spin polarized in any  $\mu\mathcal{SR}$  experiment using surface

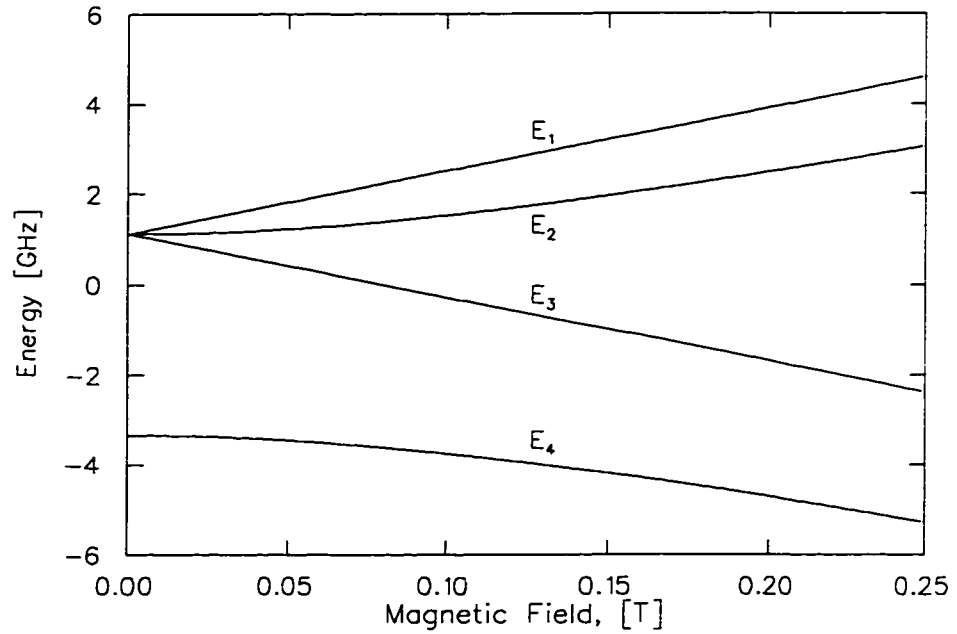


Figure A.32: Breit-Rabi energy level diagram of the four states of muonium in a magnetic field.

muons. In the case of a transverse field experiment the initial muon spin direction is perpendicular to the applied magnetic field, conventionally along the  $\vec{x}$  axis, so we have an initial muon state given by

$$|\phi_{\mu}(t=0)\rangle = \frac{1}{\sqrt{2}}(|\phi_{\mu}^{+}\rangle + |\phi_{\mu}^{-}\rangle). \quad (\text{A.32})$$

Since electrons of the stopping medium (which are captured by muons to form muonium) are unpolarized, we have two initial muonium states possible – with the electron spin either up or down. It has always been *assumed* that these are formed with equal probability; no observable departure from this has ever been reported, so we have equal contributions from each of the initial states

$$\begin{aligned} |\phi_1\rangle &= |\phi_{\mu}(0)\phi_e^{+}\rangle \quad \text{and} \\ |\phi_2\rangle &= |\phi_{\mu}(0)\phi_e^{-}\rangle. \end{aligned} \quad (\text{A.33})$$



Considering the first of these we can write, using Eq. (A.17),

$$|\phi_1\rangle = \frac{1}{\sqrt{2}}(|\phi^{++}\rangle + |\phi^{-+}\rangle) \quad (\text{A.34})$$

$$= \frac{1}{\sqrt{2}}(|\phi^{++}\rangle + \cos\beta |\psi_2\rangle - \sin\beta |\psi_4\rangle). \quad (\text{A.35})$$

At a later time  $t$ , when the initial state has evolved under the Hamiltonian, we have

$$\begin{aligned} \sigma_\mu^x e^{-i\mathcal{H}t/\hbar} |\phi_1\rangle &= \frac{\sigma_\mu^x}{\sqrt{2}} [e^{-i\mathcal{H}t/\hbar} |\phi^{++}\rangle + \cos\beta e^{-i\mathcal{H}t/\hbar} |\psi_2\rangle \\ &- \sin\beta e^{-i\mathcal{H}t/\hbar} |\psi_4\rangle] \end{aligned} \quad (\text{A.36})$$

Expanding the Hamiltonian in terms of operators and the wavefunctions in terms of the basis states, we have

$$\begin{aligned} &\frac{\sigma_\mu^+ + \sigma_\mu^-}{2\sqrt{2}} [e^{-i\omega_1 t} |\phi^{++}\rangle + \cos\beta e^{-i\omega_2 t} (\cos\beta |\phi^{-+}\rangle + \sin\beta |\phi^{+-}\rangle) \\ &\quad - \sin\beta e^{-i\omega_4 t} (-\sin\beta |\phi^{-+}\rangle + \cos\beta |\phi^{+-}\rangle)] \\ &= \frac{1}{2\sqrt{2}} [2e^{-i\omega_1 t} |\phi^{-+}\rangle + 2\cos^2\beta e^{-i\omega_2 t} |\phi^{++}\rangle + 2\cos\beta \sin\beta e^{-i\omega_2 t} |\phi^{--}\rangle \\ &\quad + 2\sin^2\beta e^{-i\omega_4 t} |\phi^{++}\rangle - 2\sin\beta \cos\beta e^{-i\omega_4 t} |\phi^{--}\rangle], \end{aligned} \quad (\text{A.37})$$

$$(\text{A.38})$$

giving

$$\begin{aligned} \sigma_\mu^x e^{-i\mathcal{H}t/\hbar} |\phi_1\rangle &= \frac{1}{2\sqrt{2}} [e^{-i\omega_1 t} |\phi^{-+}\rangle + (\cos^2\beta e^{-i\omega_2 t} + \sin^2\beta e^{-i\omega_4 t}) |\phi^{++}\rangle \\ &\quad + (\cos\beta \sin\beta e^{-i\omega_2 t} - \cos\beta \sin\beta e^{-i\omega_4 t}) |\phi^{--}\rangle]. \end{aligned} \quad (\text{A.39})$$

So we have, for that fraction of muonium formed with electron spin “up”, the contribution to  $\langle\sigma_\mu^x\rangle$  of

$$\langle\phi_1|e^{i\mathcal{H}t/\hbar}\sigma_\mu^x e^{-i\mathcal{H}t/\hbar}|\phi_1\rangle = \cos^2\beta \cos(\omega_{12}t) + \sin^2\beta \sin(\omega_{14}t). \quad (\text{A.40})$$

The other fraction, with an initial state in which the electron spin is “down”,

$$|\phi_2(0)\rangle = \frac{1}{\sqrt{2}}(|\phi_\mu^+\rangle + |\phi_\mu^-\rangle) \otimes |\phi_e^-\rangle = \frac{1}{\sqrt{2}}(|\phi^{+-}\rangle + |\phi^{--}\rangle) \quad (\text{A.41})$$

is treated in a similar way, giving

$$e^{-i\mathcal{H}t/\hbar}|\phi_2\rangle = \frac{1}{\sqrt{2}}e^{-i\mathcal{H}t/\hbar}(\sin\beta |\psi_2\rangle + \cos\beta |\psi_4\rangle + |\phi^{++}\rangle), \quad (\text{A.42})$$

and a contribution to the spin polarization of

$$\langle\phi_2|e^{i\mathcal{H}t/\hbar}\sigma_\mu^x e^{-i\mathcal{H}t/\hbar}|\phi_2\rangle = \sin^2\beta \cos(\omega_{23}t) + \cos^2\beta \cos(\omega_{34}t). \quad (\text{A.43})$$

The total polarization is simply the sum

$$P_\mu^x(t) = \frac{1}{2} \left\{ \cos^2\beta [\cos(\omega_{12}t) + \cos(\omega_{34}t)] + \sin^2\beta [\cos(\omega_{14}t) + \cos(\omega_{23}t)] \right\}. \quad (\text{A.44})$$

In weak magnetic fields of not more than about 8 G the difference between  $\omega_{12}$  and  $\omega_{23}$  is small enough that it can usually be ignored; the signal appears to have only one component at the average muonium frequency  $\omega_-$ . In higher field the splitting that originates with the hyperfine interaction term of the Hamiltonian is immediately apparent in the polarization function as beating of the these two components, the hyperfine frequency  $\omega_0$  can be obtained from the difference of the two frequencies

$$\omega_{23} - \omega_{12} = \left[ \omega_0^2 + 4\omega_+^2 \right]^{1/2} - \omega_0. \quad (\text{A.45})$$

For unperturbed muonium (in vacuum, for example) the hyperfine frequency is  $\omega_0/(2\pi) = 4463$  Mhz. [4] (In condensed matter nearby molecules can cause a distortion of the 1s orbital of the muonium electron, changing the electron spin density at the muon which is reflected in a shift of the hyperfine frequency.)

Since the high frequency transitions  $\omega_{14}$  and  $\omega_{34}$  are not resolved by the timing electronics of most  $\mu\mathcal{SR}$  spectrometers, those terms average to zero, and in fields sufficiently weak that the amplitudes of the remaining signals are approximately equal, the polarization function reduces to

$$P_\mu^x(t) \simeq \frac{1}{4} [\cos(\omega_{12}t) + \cos(\omega_{23}t)]. \quad (\text{A.46})$$

## A.2 Longitudinal Field Polarization

In the other case of interest the initial muon polarization is along the magnetic field direction. We are then interested in the time dependence of the  $\hat{z}$  component of the muon's spin in longitudinal field (LF). Since muons are produced (usually) from the decay of a charged pion (essentially at rest near the surface of the pion production target) into a two body final state *via*

$$\pi^+ \rightarrow \mu^+ + \bar{\nu}_\mu \quad (\text{A.47})$$

and since neutrinos always have negative helicity, the muon beam produced also has negative helicity. The initial polarization of the muon, having stopped in a sample, is therefore in the  $-\hat{z}$  direction. Again, muonium is formed with an electron captured from the medium with equal probability of having spin “up” or “down” with respect to the quantization axis. We are interested in the matrix elements

$$\langle \phi^{--} | e^{i\mathcal{H}t/\hbar} \sigma_\mu^z e^{-i\mathcal{H}t/\hbar} | \phi^{--} \rangle \quad (\text{A.48})$$

and

$$\langle \phi^{-+} | e^{i\mathcal{H}t/\hbar} \sigma_\mu^z e^{-i\mathcal{H}t/\hbar} | \phi^{-+} \rangle \quad (\text{A.49})$$

The first muonium state is an eigenfunction of the Hamiltonian and the matrix element given by Eq. (A.48) is therefore simply

$$\langle \phi^{--} | e^{i\omega_3 t} \sigma_\mu^z e^{-i\omega_3 t} | \phi^{--} \rangle = -1. \quad (\text{A.50})$$

Equation (A.49) can be written

$$(\cos\beta \langle \psi_2 | - \sin\beta \langle \psi_4 |) e^{i\mathcal{H}t/\hbar} \sigma_\mu^z e^{-i\mathcal{H}t/\hbar} (\cos\beta | \psi_2 \rangle - \sin\beta | \psi_4 \rangle). \quad (\text{A.51})$$

Thus, using Eq. (A.17) once again,

$$\langle \sigma_\mu^z \rangle = -(\cos^2\beta - \sin^2\beta)^2 - 4 \cos^2\beta \sin^2\beta \cos(\omega_{24}t). \quad (\text{A.52})$$

Noting that  $(\cos^2\beta - \sin^2\beta)^2 = 1 - \sin^2(2\beta)$  and that

$$\sin^2(2\beta) = \frac{1}{1+x^2},$$

this can be written

$$\langle \sigma_\mu^z \rangle = -1 + \frac{1}{1+x^2} - \frac{1}{1+x^2} \cos(\omega_{24}t) \quad (\text{A.53})$$

where  $x = 2\omega_+/\omega_0$ .

The total muon polarization  $P_\mu^z$  in longitudinal field is then the sum of these two parts, with muonium formed with equal probability in each state, giving

$$P_\mu^z = \frac{1}{2(1+x^2)} \left[ 1 + 2x^2 + \cos(\omega_{24}t) \right] \quad (\text{A.54})$$

The frequency  $\omega_{24}$  in Eq. (A.54) is sufficiently high that in most experimental situations, at this time, it is not directly observable in the data as an oscillatory signal, so this term is effectively averaged to zero by the timing resolution of the spectrometer.

Throughout this calculation we have not considered any relaxation of the muonium spin polarization.

## Appendix B

### Numerical Integration of a Highly Oscillatory Function

The complete program code that performs the numerical integration of Eq. (6.20) is given here. The evaluation of this integral is made complicated by the oscillatory nature of the integrand, and that we are integrating over both  $\omega$  and  $t$  in terms like  $\cos(\omega t)$ . Fortunately, there is a natural upper cut-off in frequency given by the highest lattice modes (approximately the Debye frequency) but  $t$  still runs from 0 to  $\infty$ .

The key to integrating this function is to determine how far out in time one actually needs to integrate in order for the integral to converge. Since the integrand oscillates about zero and always decreases in amplitude as  $t \rightarrow \infty$ , the integral also oscillates as the upper limit in time is taken to infinity, and the range of these oscillations decreases as  $t \rightarrow \infty$ . This code decides when to stop integrating by comparing the range of oscillation of the integral to the mean of the last local minimum and maximum values of the integral. When the range of oscillation is a (pre-set) small fraction of the mean value, the value of the mean is taken to be the estimate of the integral in the limit  $t \rightarrow \infty$ . The algorithm requires the integrand to have its maximum value at  $t = 0$  and an envelope that decreases monotonically with time..

```
#define float double

#include <math.h>
#include <stdlib.h>
#include <stdio.h>
```

```
#include "1ph_hr_2.c"

void hop_rate_(double *, double *, double *, double *, double *);

void main()
{
    float temperature, lp, lb,delta, hop_rate;
    FILE *fp;

    fp=fopen("1ph_hr_2d.out","w");

    lp=38.801;
    lb=2.5;
    delta=0.079194;

    fprintf(fp, " lp=%f \n", lp);
    fprintf(fp, " lb=%f \n", lb);
    fprintf(fp, " delta=%f \n", delta);

    for(temperature=38; temperature<=116; temperature += 3.0){
        hop_rate_(&temperature, &delta, &lb, &lp, &hop_rate);
        fprintf(fp, " %E %E \n", temperature, hop_rate);
    }

    fclose(fp);
}
```

```
/* 1PH_HR_2.c calculates hop rate in 1phonon model, with polaron
and flucuational barrier preparation by direct numerical integration.
Phonon spectrum of solid Xe is included in function g(w).
*/

#define float double

#include <stdlib.h>
#include <stdio.h>
#include <math.h>

float my_int(float (*func)(float), float a, float b, long int n);
float t_int(float (*func)(float));
float f1(float);
float f2(float);
float f1_approx(float);
float f2_approx(float);
float fg(float);
float g(float);
float f_of_t(float);
float f_of_t_test(float);
float f_approx(float);
float sqr(float);
float coth(float);
```

```
float hop_rate(void);
float f_lb(float);
float f_lp(float);
float sign(float);

/* global variables and constants used by several functions */
float t, tp, omega, omega_d, th_d, lb, lp, delta, gf;
float hbar, kb, ff;
float bb_fctr, bb_om;
long int nn;

void hop_rate_(double *ptp, double *pdelta, double *plb, double *plp,
               double *hpr)
{
    float time_range, t1, t2, dt, dtime, tt, foft, z1,z2;
    float i1,i2;
    long int n_cur, curve, nn_max;

    hbar = 1.055E-34;           /* Plank's constant          */
    kb = 1.381E-23;            /* Boltzman's constant      */
    ff = hbar/kb;
    th_d=64.0;                 /* Debye temperatrue of Xe */
    omega_d = kb*th_d/hbar;

    tp=*ptp;
    lb=*plb;
```



```

lp=*plp;
delta=*pdelta;

nn=4000;
if(tp>=110) nn=8000;
gf= my_int(*fg, 0.0, omega_d, 8000);
z1=2.0*t_int(*f_of_t);
*hpr=sqr(delta*kb/hbar)*z1;
return;
}

```

/\* t\_int integrates an oscillatory function of time, whose amplitude decreases with time, from zero up to such time that the amplitude of oscillation of its integral is small compared to the mean, which is taken to be the limiting value of the integral. I.e., it goes as far out as it needs to so that it is clear to what value it is converging \*/

```

#define FUNC(x) ((*func)(x))
float t_int(float (*func)(float))
{
    float a,sum, del, m, maxval, minval,cc;
    int goodmax, goodmin,conv=0;

    del=4.0E-17; /* fixed step size in seconds */
    cc=1.0E-2; /* Convergence criteria: (max-min) < 0.01*mean */

```

```
maxval=0.0;
minval=0.0;

sum=0.0E0;
a=del/2.0;    /* start offset at centre of first interval */
m=0.0E0;
while(!conv){
    goodmax=0;
    goodmin=0;
    while(!goodmax){
        sum += FUNC(a + m*del);
        m++;
        if(sum<=maxval) goodmax=1;    /* found new maxval */
        else maxval=sum;
    }

    minval=maxval;
    while(!goodmin){
        sum += FUNC(a + m*del);
        m++;
        if(sum>=minval) goodmin=1;    /* found new minval */
        else minval=sum;
    }

    if( (maxval-minval)< cc*(maxval+minval)*0.5) conv=1;
    else{
```

```
        goodmax=0;
        goodmin=0;
        maxval=minval;
    }
}
return((maxval+minval)*0.5*del);
}
#undef FUNC(x)

/* My dumb, brute-force integrator */
#define FUNC(x) ((*func)(x))
float my_int(float (*func)(float), float a, float b, long int n)
{
    float x, sum, del, m;

    del=(b-a)/n;
    sum=0.0;
    a=a+del/2.0;
    for (m=0; m<=n-1; m++){
        sum += FUNC(a + m*del);
    }
    return(sum*del);
}
```

```
#undef FUNC(x)

float f_of_t(float x)    /* the function of time that gets integrated */
{
    float f, psi_bar, psi;

    t=x;    /* passes time to global variable t */

    psi_bar = my_int(*f1, 0.0, omega_d, nn);
    psi      = my_int(*f2, 0.0, omega_d, nn);

    f=exp(psi_bar+gf)*cos(-psi); /* im part = sin(psi) dropped */

    return(f);
}

float f1(float w)    /* integrand for Psi bar - fcn of omega */
{
    float l_fctr, v;

    if(w==0.0) return(0.0);

    l_fctr=(lb*hbar*w)/(kb*th_d) + lp*kb*th_d/(hbar*w);
    v=g(w)*l_fctr*cos(w*t)/sinh(hbar*w/(2.0*kb*tp));
    return(v);
}
```

```
float f2(float w)      /* integrand for Psi - fcn of omega */
{
    float l_f,v;

    if(w==0.0) return(0.0);
    l_f = 2.0*sqrt(lb*lp);
    v=l_f * g(w) * sin(w*t)/sinh((hbar*w)/(2.0*kb*tp));

    return(v);
}

float fg(float w)
{
    float tmp,v;

    if(w==0.0) return(0.0);
    tmp=(lb*hbar*w)/(kb*th_d) - lp*(kb*th_d)/(hbar*w);
    v=g(w)*tmp*coth((hbar*w)/(2.0*kb*tp));
    return(v);
}

/* Real g(w) for s-Xe by simple linear interpolation between points*/
/* Data read from a graph in Klein's Rare Gas Solids , p964 ? */
float g(float omega)
{

```

```

float  x, y, t_dist;
long int i;

float yy[70] =
    {0.0,0.07,0.15,0.30,0.45, .6,.9,1.1,1.32,1.7,
    2.0,2.2,2.7,3.1,3.8, 4.25,5.0,5.7,6.3,7.1,
    8.0,9.3,10.6,11.7,13.0, 14.8,16.5,18.6,21.0,24.5,
    34.0,34.93,35.86,36.77,37.71, 38.64,39.57,40.50,41.43,42.36,
    43.29,44.21,45.14,46.07,47.00, 28.0,27.9,27.8,27.6,27.2,
    27.0,26.0,25.0,23.0,21.0, 18.5,36.0,43.0,51.0,
    64.0,33.0,22.0,10.0,0.0,0.0,0.0,0.0,0.0};

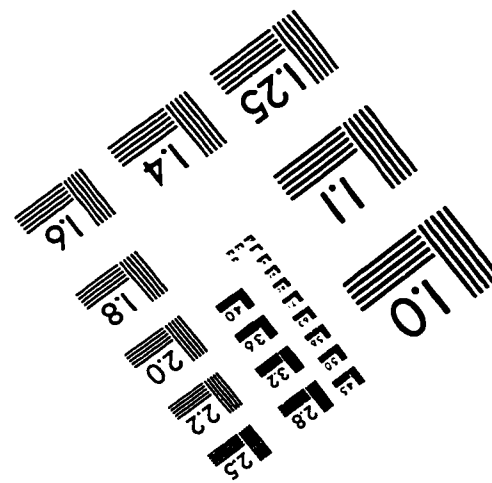
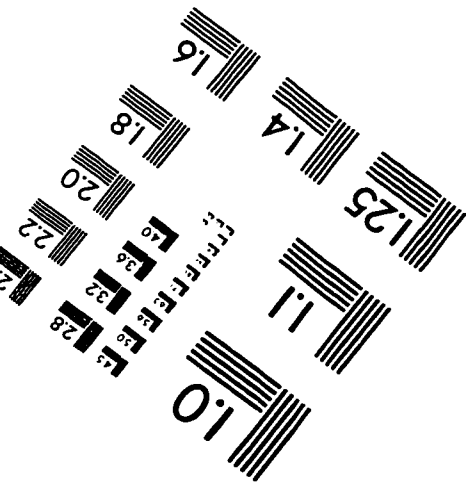
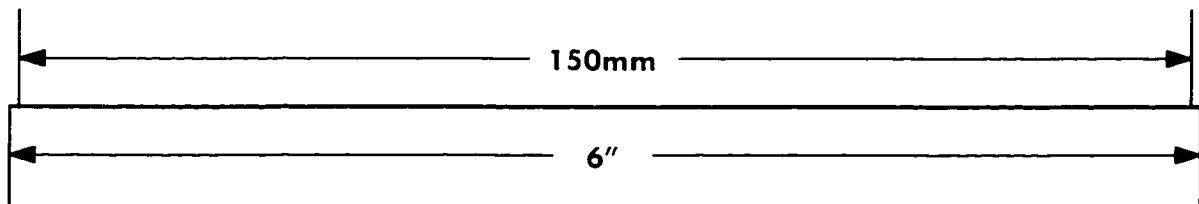
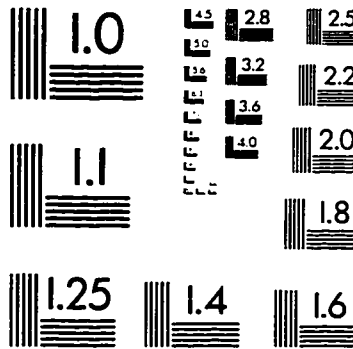
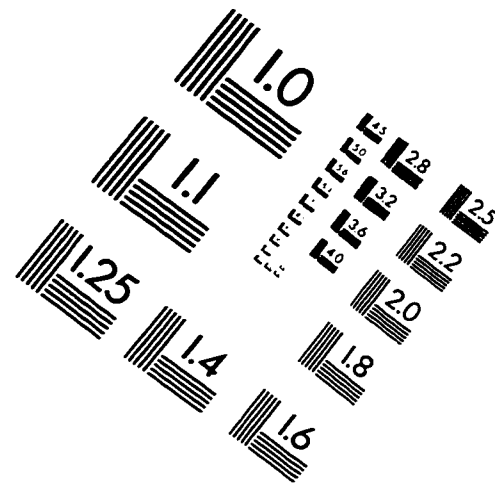
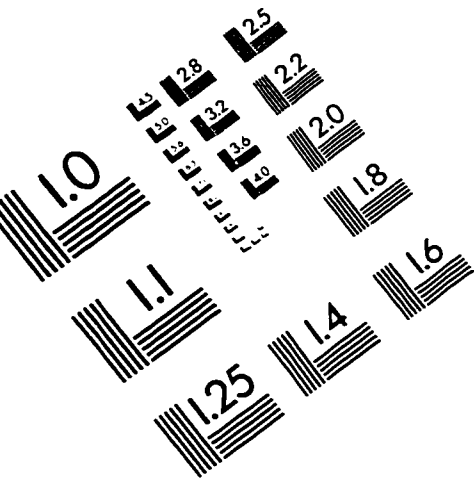
x=omega*(97.9/12.57E12);      /* scale interpolation variable */
i=x;
if(x<=10){
    y= 0.019*x*x;           /* at low omega like omega^2 */
    return(y/1.7217424E14);
}
if(i>=64){                  /* above cutoff -> zero */
    y=0.0;
}
else{
    y=yy[i] + (x - (float) i)*(yy[i+1] - yy[i]);
}
return(y/1.7217424E14);     /* normalized so its integral is 1.0000 */
}

```

```
/* def some math */
float sqr(float x)
{
    return(x*x);
}

float coth(float x)
{
    return(cosh(x)/sinh(x));
}
```

# IMAGE EVALUATION TEST TARGET (QA-3)



APPLIED IMAGE, Inc  
1653 East Main Street  
Rochester, NY 14609 USA  
Phone: 716/482-0300  
Fax: 716/288-5989

© 1993, Applied Image, Inc., All Rights Reserved